The Chandra Deep Survey of the Hubble Deep Field North Area. II. Results from the Caltech Faint Field Galaxy Redshift Survey Area[1]

A.E. Hornschemeier,[2] W.N. Brandt,[2] G.P. Garmire,[2] D.P. Schneider,[2] A.J. Barger,[3,4,5,6] P.S. Broos,[2] L.L. Cowie,[3,6] L.K. Townsley,[2] M.W. Bautz,[7] D.N. Burrows,[2] G. Chartas,[2] E.D. Feigelson,[2] R.E. Griffiths,[8] D. Lumb,[9] J.A. Nousek,[2] L.W. Ramsey,[2] and W.L.W. Sargent[10]

ABSTRACT

A deep X-ray survey of the Hubble Deep Field North (HDF-N) and its environs is performed using data collected by the Advanced CCD Imaging Spectrometer (ACIS) on board the *Chandra X-ray Observatory*. Currently a 221.9 ks exposure is available, the deepest ever presented, and here we give results on X-ray sources located in the $8.6' \times 8.7'$ area covered by the Caltech Faint Field Galaxy Redshift Survey (the "Caltech area"). This area has (1) deep photometric coverage in several optical and near-infrared bands, (2) extensive coverage at radio, submillimeter and mid-infrared wavelengths, and (3) some of the deepest and most complete spectroscopic coverage ever obtained. It is also where the X-ray data have the greatest sensitivity; the minimum detectable fluxes in the 0.5–2 keV (soft) and 2–8 keV (hard) bands are $\approx 1.3 \times 10^{-16}$ erg cm^{-2} s^{-1} and $\approx 6.5 \times 10^{-16}$ erg cm^{-2} s^{-1}, respectively. More than $\approx 80\%$ of the extragalactic X-ray background in the hard band is resolved.

---

[1]Based on observations obtained at the W. M. Keck Observatory which is operated jointly by the California Institute of Technology and the University of California. Based on observations obtained by the Hobby-Eberly Telescope, which is a joint project of The University of Texas at Austin, The Pennsylvania State University, Stanford University, Ludwig-Maximillians-Universität München, and Georg-August-Universität Göttingen.

[2]Department of Astronomy & Astrophysics, 525 Davey Laboratory, The Pennsylvania State University, University Park, PA 16802

[3]Institute for Astronomy, University of Hawaii, 2680 Woodlawn Drive, Honolulu, HI 96822

[4]Department of Astronomy, University of Wisconsin-Madison, 475 N. Charter Street, Madison, WI 53706

[5]Hubble Fellow and Chandra Fellow at Large

[6]Visiting Astronomer, W.M. Keck Observatory, jointly operated by the California Institute of Technology and the University of California

[7]Massachusetts Institute of Technology, Center for Space Research, 70 Vassar Street, Building 37, Cambridge, MA 02139

[8]Department of Physics, Carnegie Mellon University, Pittsburgh, PA 15213

[9]Astrophysics Division, ESTEC, Keplerlaan 1, 2200 AG Noordwijk, The Netherlands

[10]Palomar Observatory, California Institute of Technology, Pasadena, CA 91125

The 82 *Chandra* sources detected in the Caltech area are correlated with more than 25 multiwavelength source catalogs, and the results of these correlations as well as spectroscopic follow-up results obtained with the Keck and Hobby-Eberly Telescopes are presented. All but nine of the *Chandra* sources are detected optically with $R \lesssim 26.5$. Redshifts are available for 39% of the *Chandra* sources, including 96% of the sources with $R < 23$; the redshift range is 0.1–3.5, with most sources having $z < 1.5$. Eight of the X-ray sources are located in the HDF-N itself, including two not previously reported. A population of X-ray faint, optically bright, nearby galaxies emerges at soft-band fluxes of $\lesssim 3 \times 10^{-16}$ erg cm^{-2} s^{-1}.

Our multiwavelength correlations have set the tightest constraints to date on the X-ray emission properties of μJy radio sources, mid-infrared sources detected by *ISO*, and very red ($\mathcal{R} - K_{\rm s} > 5.0$) objects. Sixteen of the 67 1.4 GHz μJy sources in the Caltech area are detected in the X-ray band, and the detection rates for starburst-type and AGN-candidate μJy sources are comparable. Only two of the 17 red, optically faint ($I > 25$) μJy sources are detected in X-rays. While many of the starburst-type μJy sources appear to contain obscured AGN, the *Chandra* data are consistent with the majority of the μJy radio sources being powered by star formation. Eleven of the ≈ 100 *ISO* mid-infrared sources found in and near the HDF-N are detected in X-rays. In the HDF-N itself, where both the infrared and the X-ray coverage are deepest, it is notable that six of the eight *Chandra* sources are detected by *ISO*; most of these are known to be AGN where the X-ray and infrared detections reveal both the direct and indirect accretion power being generated. The high X-ray to infrared matching rate bodes well for future sensitive infrared observations of faint X-ray sources.

Four of the 33 very red objects that have been identified in the Caltech area by Hogg et al. (2000a) are detected in X-rays; these four are among our hardest *Chandra* sources, and we argue that they contain moderately luminous obscured AGN. Overall, however, the small *Chandra* detection fraction suggests a relatively small AGN content in the optically selected very red object population. A stacking analysis of the very red objects not detected individually by *Chandra* yields a soft-band detection with an average soft-band X-ray flux of $\approx 1.9 \times 10^{-17}$ erg cm^{-2} s^{-1}; the observed emission may be associated with the hot interstellar media of moderate redshift elliptical galaxies.

Constraints on AGN candidates, extended X-ray sources, and Galactic objects in the Caltech area are also presented.

Subject headings: diffuse radiation – surveys – cosmology: observations – galaxies: active – X-rays: galaxies – X-rays: general.

1. Introduction

Observations with the *Chandra X-ray Observatory* are in the process of revolutionizing studies of the X-ray background and the sources that comprise it. Not only has most of the 2–8 keV background now been resolved into point sources (e.g., Brandt et al. 2000; Mushotzky et al. 2000; Giacconi et al. 2001, hereafter G01), but the high-quality *Chandra* positions also allow these sources to be matched unambiguously to (often faint) multiwavelength counterparts. Surveys over a broad X-ray band have finally reached the depths needed to complement the most sensitive surveys in the radio, submillimeter and infrared bands. In these bands, star formation and lower luminosity active nuclei in moderate-to-high redshift galaxies are thought to dominate the energy production (e.g., Richards et al. 1998, hereafter R98; Aussel et al. 1999, hereafter A99; Barger, Cowie, & Richards 2000, hereafter BCR00).

We have undertaken a deep X-ray survey with the *Chandra X-ray Observatory* (hereafter *Chandra*; Weisskopf, O'Dell, & van Speybroeck 1996) centered on the most intensively studied extragalactic patch of sky, the Hubble Deep Field North (HDF-N; Williams et al. 1996, hereafter W96; Ferguson, Dickinson, & Williams 2000). The Advanced CCD Imaging Spectrometer (ACIS; G.P. Garmire et al., in preparation) has achieved 221.9 ks of exposure in four spatially staggered segments over an $\approx 17' \times 19'$ region (see Figure 1). In the area of deepest coverage, the minimum detectable fluxes in the 0.5–2 keV (soft) and 2–8 keV (hard) bands are $\approx 1.3 \times 10^{-16}$ erg cm^{-2} s^{-1} and $\approx 6.5 \times 10^{-16}$ erg cm^{-2} s^{-1}, respectively.

In Hornschemeier et al. (2000, hereafter H00), we presented first results from the survey based on 164.4 ks of data; our focus was almost entirely on the HDF-N itself, although we also presented tight constraints on the X-ray emission properties of submillimeter sources found outside the HDF-N. In this paper, we present results derived from more data over a significantly larger area: that studied by the Caltech Faint Field Galaxy Redshift Survey (hereafter the "Caltech area"; e.g., Hogg et al. 2000a, hereafter Hogg00; Cohen et al. 2000, hereafter C00). This area covers $8.6' \times 8.7'$ and has (1) deep photometric coverage in several optical and near-infrared bands, (2) extensive coverage at radio, submillimeter and mid-infrared wavelengths, and (3) some of the deepest and most complete spectroscopic coverage ever obtained. This is also the region where our X-ray data have the greatest sensitivity (see Figure 1). The optical and near-infrared photometric coverage includes the HDF-N itself (W96), the eight *HST* flanking fields adjacent to the HDF-N (W96; these reach $I \approx 25$), and the deep ground-based imaging presented by Hogg00 which reaches $U_{\rm n} = 25$, $G = 26$, $\mathcal{R} = 25.5$ and $K_{\rm s} = 20.5$. We also have deep I and V band images covering the field (Barger et al. 1999) as well as deep Keck R (BCR00) images covering portions of the field. The multiwavelength coverage includes radio surveys and maps (e.g., R98; Muxlow et al. 1999; Garrett et al. 2000; Richards 2000, hereafter R00; and references therein), submillimeter surveys (e.g., Hughes et al. 1998; BCR00; Borys et al. 2001; Chapman et al. 2001), and infrared surveys (e.g., A99; Thompson et al. 1999; Dickinson et al. 2000; Hogg et al. 2000b). Finally, more than 670 redshifts have been obtained in this area, primarily with the Keck Telescope (C00 and references therein).

We have detected 82 *Chandra* sources in the Caltech area, and in this paper we present the X-ray source catalog and correlate it with the multiwavelength source catalogs described above. Our goals are (1) to understand the broad-band emission and nature of the sources producing most of the X-ray background in the 0.5–8 keV band and (2) to investigate the X-ray emission properties of physically interesting sources identified at other wavelengths. We present optical spectra for 15 of these sources, using data obtained by the Keck and Hobby-Eberly Telescopes. A companion paper, G.P. Garmire et al., in preparation (Paper III), presents the number counts derived from this field and further details on the X-ray spectral properties of these sources.

The Galactic column density along this line of sight is $(1.6 \pm 0.4) \times 10^{20}$ cm^{-2} (Stark et al. 1992), and $H_0 = 70$ km s^{-1} Mpc^{-1} and $q_0 = 0.1$ are adopted throughout this paper. Coordinates throughout this paper are J2000.

2. Chandra ACIS Observations

The field containing the HDF-N was observed with the *Chandra* ACIS for a total exposure time of 221.9 ks in four separate observations between 1999 Nov and 2000 Feb; a journal of observations is presented in Table 1. ACIS consists of ten CCDs designed for efficient X-ray detection and spectroscopy. Four of the CCDs (ACIS-I; CCDs I0–I3) are arranged in a 2×2 array with each CCD tipped slightly to approximate the curved focal surface of the *Chandra* High Resolution Mirror Assembly (HRMA). The remaining six CCDs (ACIS-S; CCDs S0–S5) are set in a linear array and are tipped to approximate the Rowland circle of the objective gratings that can be inserted behind the HRMA. The CCD which lies on-axis in ACIS-I is I3. Each CCD subtends an $8.3' \times 8.3'$ square on the sky. The HDF-N was placed near the "aim point" of the ACIS-I array during all four observations. While observing with ACIS-I, two CCDs from ACIS-S, typically S2 and S3, can be operated. CCD S3 was turned off during the HDF-N observations due to the higher background level of this device; this property may cause telemetry saturation during background flares. CCD S2 was operated during our observations, but since it is far off-axis, it is outside the Caltech area under study in this paper.

The full ACIS-I field of view is $16.9' \times 16.9'$,[1] although the region of full exposure (221.9 ks) is somewhat reduced due to the different pointings of the four separate observations. These offsets were necessary to satisfy the roll constraints of *Chandra* while keeping the HDF-N itself near the area of best focus and away from the gaps between the four ACIS-I CCDs (see Figure 1). The on-axis image quality is $\approx 0.5''$ FWHM increasing to $\approx 3.0''$ FWHM at $\approx 4.0'$ off-axis.[2] The focal-plane temperature, which governs several characteristics of the CCD behavior, in particular the Charge Transfer Inefficiency (CTI), was -110°C during the first three observations and -120°C

---

[1] There are small gaps between the CCDs; see Figure 1.

[2] Each ACIS pixel is $0.49''$ on a side.

during the fourth. The version numbers of the *AXAF*[3] Science Center Data System software used for the processing of these data were R4CU4UPD2 for the first three observations and R4CU5UPD2 for the fourth. The data processing dates were 1999 Nov 26, 1999 Nov 27, 1999 Nov 28, and 2000 Apr 19.

The data were corrected for the radiation damage the CCDs suffered during the first few weeks of the mission (Hill et al. 2000; Prigozhin et al. 2000) following the procedure of Townsley et al. (2000), which corrects simultaneously for both position-dependent gain shifts and event grade changes. There is still some ($\approx$ 11%) residual quantum efficiency (QE) degradation in the -110°C data at the center of the ACIS-I array at 5.9 keV;[4] but this is improved over the $\approx$ 19% loss incurred without CTI correction (Townsley et al. 2000). At -120°C, the 5.9 keV QE loss from CTI is $\approx$ 10% at the center of the ACIS-I array before CTI correction, and it is $\approx$ 5% with correction. For a $\Gamma = 1.4$ power law ($N = AE^{-\Gamma}$, where N is the number of photons per second per cm^{-2} per keV, A is a normalization constant, and Γ is the photon index), 5% of the hard-band energy flux is lost due to this residual QE deficiency, so the incurred error is generally small compared to measurement error. We do not correct for this residual QE loss, as it is dependent on the spectral shape of the source, and the X-ray photon statistics are generally too limited to constrain the detailed spectral properties of the sources. For extremely hard sources, where most of the photon flux occurs at observed energies greater than 5 keV, it is possible that the hard-band fluxes will have been underestimated by a slightly larger factor. However, the HRMA effective area is quite small above 5 keV, so few such extremely hard sources would be detected in the current sample regardless of the effects of CTI.

The background was stable during the entire 221.9 ks of observation. The 0.5–8 keV light curves have been inspected for all of the observations, and they are free from strong flaring due to "space weather." Over the four observations, only seven 3.3-s frames were "dropped" from the telemetry, which amounts to a data loss of less than 0.01% (frames are dropped when background flaring occurs, causing the telemetry to be saturated). During any observation the background is stable to within $\approx$ 20%, and the mean background levels from the four observations agree to within 10%. The average background over the fully exposed portion of the Caltech area is 0.053 count pixel^{-1} in the 0.5–8 keV band. Thus, even with a total observation length of 221.9 ks, the observation is still photon limited. *Chandra* ACIS should remain photon limited near the optical axis and for point source detection in the 0.5–8 keV band out to exposure lengths of $\approx$ 4 Ms.

[3] *Advanced X-ray Astrophysics Facility*, the name of the *Chandra* mission before launch.

[4] The effect of CTI is most severe at higher energies and farthest from the read-out nodes. The center of the ACIS-I array is far from the read-out nodes, so these values are the worst-case scenario.

3. Chandra Source Searching and Analysis

The X-ray data analysis performed in this paper was carried out using the *Chandra* X-ray Center's (CXC's) *Chandra* Interactive Analysis of Observations (CIAO) software as well as the Interactive Data Language (IDL) based Tools for ACIS Real-Time Analysis (TARA) software developed at Penn State (publicly available; see Broos et al. 2000).

3.1. X-ray Image Creation

The four observations were co-added after cross-registration using 12 bright X-ray sources detected in each of the individual observations near the optical axis (see Figure 2). All observations were reassigned to the coordinate system of observation 966 (see Table 1), requiring shifts of $\approx 1''$ and very small rotational corrections (0.01–0.20°). After cross-registration, the offsets of the other three observations from the coordinate system of 966 were zero within plausible errors with $0.22''$ root mean square (RMS) dispersion in right ascension and $0.19''$ RMS dispersion in declination. Thus internal cross-registration of the four observation datasets is accurate to within $0.3''$.

Absolute X-ray source positions were obtained by matching bright (> 25 counts) 0.5–8 keV X-ray sources to either $R < 23$ sources in the Hogg00 catalog or any radio source in the R00 1.4 GHz catalog. Using the astrometry as determined on board *Chandra* before any astrometric corrections were made, the 22 matched sources had a mean offset from the X-ray sources of $1.88 \pm 0.70''$. After shifting and slightly rotating the positions of the X-ray sources so that the mean offset was zero, the RMS scatter in the offsets was $0.46''$. The dispersion in positional offsets for these 22 sources is shown in Figure 2, along with an ellipse showing the RMS dispersion of offsets for this group. We adopt $0.5''$ as our systematic positional uncertainty but note that for X-ray sources with $\lesssim 10$ counts and/or larger off-axis angles ($\gtrsim 3.0'$), the positional uncertainty will be dominated by photon statistics and will be $\gtrsim 1.0''$.

Images were created from 0.5–8 keV (full band), 0.5–2 keV (soft band) and 2–8 keV (hard band) using the CIAO DATAMODEL software. *ASCA* event grades 0, 2, 3, 4 and 6 were used in all analyses, as this is the grade distribution currently being supported by the CXC. In the future, as support is developed for different grade distributions, the effective background may be reduced by choosing a subset of these grades (compare with Brandt et al. 2000). Neglecting the 8–10 keV data improves the signal-to-noise ratio in the hard-band, as the effective area of the mirror is steeply decreasing while the overall background is increasing with energy over this range. The raw images are shown in Figure 3 for both the soft and hard bands. Figure 4 displays the same data adaptively smoothed at the 3σ level using the code of Ebeling, White, & Rangarajan (2001). We did not use the adaptively smoothed images for source searching, but they do show most of the detected X-ray sources more clearly than the raw data. Note that some of the sources we detect do not appear in Figure 4 because they fall below the 3σ level of the adaptive smoothing.

3.2. X-ray Exposure Map

The amount of ACIS exposure for a given patch of sky in the Caltech area is influenced by two main factors: (1) telescope vignetting reducing the effective area at larger off-axis angles, and (2) observatory dither changing the celestial location of bad pixels and gaps between the CCDs and thus reducing the amount of time a given area is visible (see Figure 1). An "effective exposure time," defined as the equivalent amount of exposure time for a source located at the aim point, can be calculated taking these two effects into account.

For this data set, effective area maps were generated using a script developed by T. S. Koch, P. S. Broos, and D. P. Huenemoerder.[5] This script uses a combination of FTOOLS (FTOOLS Group 2000) and CIAO DATAMODEL tools to generate QE and effective area maps for each of the individual observations. The CIAO tool MKEXPMAP, one of the tools used in the aforementioned script, makes a map of average effective area over an individual observation (with units cm^2). We generated an effective area map assuming a $\Gamma = 1.4$ power-law spectrum for the full 0.5–8 keV energy range.

To translate effective area into effective time, these effective area maps are binned into $1''$ square pixels, and a median map is generated by replacing each effective area value with the median of the effective area values in a circular region of diameter $5''$, a dimension chosen to be representative of a source detection cell size. The motivation for making the median map was to produce a two-dimensional "look-up" table whose individual entries would be appropriate for the range of *Chandra* PSF values over the entire survey area (≈ 1.0–$5.0''$). The median statistic was chosen over the average since it is more robust. The median map is divided by the maximum effective area and multiplied by the total exposure time. The four (see Table 1) individual exposure maps were added to produce the full exposure map (see Figure 1) for the entire 221.9 ks observation. Figure 1 also shows the survey area as a function of effective exposure time and the distribution of exposure times for the 82 X-ray sources described in § 3.3 (effective exposure times for the individual sources are given in Table 4). The few sources with exposure times much shorter than 221.9 ks are located on or near the gaps between the CCDs. These gaps have effective widths of $\approx 32''$; the observatory dither reduces their sharpness and produces scatter in the exposure times. The mean effective exposure time in the entire region is 203 ± 14 ks. The median effective exposure time is 207 ks, and the minimum effective exposure possible is 89 ks in the center of the gaps between the CCDs.

3.3. X-ray Emission from Point Sources

We searched the images described in §3.1 with the WAVDETECT software (Dobrzycki et al. 1999; Freeman et al. 2001) using the same methods and safety checks as Brandt et al. (2000) and H00. We have used a probability threshold of 1×10^{-7} for source detection and searched using a

[5] The script is available at http://www.astro.psu.edu/xray/acis/recipes/exposure.html

"$\sqrt{2}$ sequence" of wavelet scales (scales of 1, $\sqrt{2}$, 2, $2\sqrt{2}$, 4, $4\sqrt{2}$, 8, $8\sqrt{2}$, and 16 pixels). The X-ray images shown in Figure 3 have dimensions of $\approx 1032 \times 1044$ pixels; this means that we expect ≈ 0.1 false detections per image for the case of a uniform, static background. In reality, the background is neither perfectly uniform or static. The background level decreases in the gaps between CCDs and increases slightly near bright point sources due to the point spread function (PSF) wings. This latter effect should be small in the current data, since there are few bright sources. The 90% encircled energy radius of the PSF, even at $4'$ off-axis and for the hardest energies under analysis here, is only $5''$.

We mentioned in §2 that there were no significant background flares during any of the observations. However, there are other transient and more isolated phenomena, the most important of which is the occasional flaring pixel (CXC, private communication). Flaring pixels occur in front-side illuminated ACIS CCDs when charge from an incident charged particle is released slowly in a fashion that resembles real X-rays. The result is a series of spurious events occurring in the same CCD pixel over 2–7 sequential frames. We have performed a flaring pixel analysis using code developed by T. Miyaji, which searches temporally for events showing the characteristic energy decay of a flaring pixel event.[6] Using this code, we were able to reject nine sources where flaring pixel events combined with background events to exceed the source detection threshold (see Table 2). All of the rejected sources had fewer than nine counts, and only one had more than seven counts. All but one were also detected only in the soft band, and all sources were only present in one of the four observations. Any sources with fewer than seven counts, especially if only detected in the soft band, are still considered marginal but are included in the X-ray source catalog.

Even in a 221.9 ks observation the ACIS data are far from being background limited (see §2). Over the entire Caltech area the detection limit for point sources with our selection criteria is $\approx$ 5–7 counts in the full, soft and hard bands. For a power-law model with photon index $\Gamma = 1.4$ and the Galactic column density, seven counts in 221.9 ks corresponds to a soft (hard) observed flux detection limit of 1.3×10^{-16} erg cm^{-2} s^{-1} (6.5×10^{-16} erg cm^{-2} s^{-1}). For the cosmology of §1, at $z = 1$ the corresponding rest-frame luminosity limits are $L_{0.5-2} = 3.4 \times 10^{41}$ erg s^{-1} ($L_{2-8} = 1.8 \times 10^{42}$ erg s^{-1}); even fairly low-luminosity Seyfert galaxies should be detected at this redshift.

A summary of the numbers of detected X-ray sources and the background levels in each of the three bands is given in Table 3. We have also searched in the 5–8 keV band, described as the "ultra-hard" band in Table 3, finding 10 sources. All but one of these 5–8 keV sources have strong 2–8 keV counterparts; the one remaining source was detected with only 3.8 counts in the ultra-hard band. We have not included this faint ultra-hard-band source in the list as its detection is marginal at this point.

There are a total of 82 *Chandra* sources in the Caltech area, 73 of which are detected in the

[6]This code is available at ftp://maibock.phys.cmu.edu/pub/miyaji/Flagflare.tar.gz

full band. Of the 45 hard-band sources, 13 are not detected in the soft band. Of the 62 soft-band sources, 31 are not detected in the hard band. The fraction of soft-band sources detected only in the soft band is somewhat lower than the fraction of G01, but the two are roughly consistent. The fraction of hard-band sources detected only in the hard band is somewhat higher than that of G01 (15/45 as compared to G01's 15/91). This difference could be due to the hardening of sources at faint fluxes; the data presented in this paper are for a 221.9 ks observation, as compared to the 130 ks observation presented in G01.

The catalog of source detections and individual source properties is given in Table 4. The source positions listed are the WAVDETECT full-band X-ray source positions except when the source was only detected in the soft band (there were no sources detected in the hard band but not in the full band). Source photometry was performed by WAVDETECT whose accuracy was verified with our own aperture photometry. Good agreement was found for sources with greater than 20 counts when using a circular aperture of radius $3.0''$ and background annulus of inner and outer radius $4.0''$ and $6.0''$, respectively. For sources with fewer than 20 counts, the agreement is not quite as tight, but it is still consistent within the errors quoted by WAVDETECT. Three sources detected by WAVDETECT with fewer than five counts were found to have 5–8 counts when aperture photometry was performed. This discrepancy is due to a failure in the WAVDETECT source characterization code which occasionally "collapses" one or both of the axes of the "source ellipse" to zero, resulting in a gross underestimate of the number of counts present even though a source was detected with a probability threshold of 1×10^{-7}. We have manually inspected these three discrepant sources and indeed find sources at the positions that WAVDETECT reports. For these sources, we have used the counts determined by the aperture photometry; all three are marked in Table 4. For sources that were not detected in a given band, we determine upper limits at the 99% confidence level by interpolating between the values in Table 3 of Kraft, Burrows, & Nousek (1991). All X-ray upper limits in this paper used this same methodology. The aperture sizes used to determine the upper limits depended on how far off axis the source was. Aperture diameters of $2''$, $3''$, and $4''$ were used for sources with off-axis angle, θ, satisfying $\theta < 3'$, $3' \leq \theta < 5'$ and $5' \leq \theta < 6'$, respectively.

The X-ray band ratio in Table 4 is defined as the ratio of hard-band to soft-band counts, and it is plotted versus soft-band count rate for all the *Chandra* sources in Figure 5. We find, with two exceptions (see the caption of Figure 5), that the sources become harder at low soft-band count rates, consistent with the results of G01. The power-law photon indices in Table 4 have been determined from these X-ray band ratios using the AO2 version of the Portable, Interactive, Multi-Mission Simulator (PIMMS; Mukai 2000). In the case of "low" numbers of counts we assume $\Gamma = 1.4$; this value is the counts-weighted mean photon index for sources with fewer than 300 full-band counts (see Paper III). A source with a "low" number of counts is defined as being (1) detected in only the hard band with less than 15 counts, (2) detected in only the soft band with less than 30 counts, or (3) detected in both the hard and soft bands, but with less than 15 counts in each. In the current sample, 45 of the 82 sources are considered to have "low" numbers of counts by these criteria. A more complete spectral analysis will be presented in Paper III.

In Table 4 we also present observed fluxes for the full, hard and soft bands. These have been determined from the given count rates and photon indices using the AO2 version of PIMMS, except in the case of the two spectroscopically identified M stars (see §7.7) where we have assumed a $kT = 0.5$ keV thermal bremsstrahlung model. The listed fluxes have not been corrected for Galactic absorption; this effect is small due to the low Galactic column density along the line of sight to the HDF-N (see §1). We estimate the fluxes to be accurate to roughly 30%, as residual uncertainties of CTI-induced QE loss and other calibration issues still exist. The errors introduced in the fluxes by using a $\Gamma = 1.4$ power law for a source with a $\Gamma = 1.7$ power-law continuum are 14%, 5%, and 2% for the full, hard, and soft bands, respectively.

Using the normalization of Ishisaki (1997), the 45 hard-band X-ray sources in the Caltech area are found to account for $\gtrsim 80\%$ of the diffuse extragalactic X-ray background in the hard band (Paper III; after adding the fraction of the background already resolved in wide-field surveys).

3.4. Extended X-ray Emission

To investigate possible extended X-ray emission from the *Chandra* sources, we have identified the sources whose extents as determined by WAVDETECT (see §9.2 of Dobrzycki et al. 1999) significantly exceed the 50% encircled-energy radius of the *Chandra* PSF at 1.5 keV (see Figure 4.8 of the Version 3 *Chandra* Proposers' Observatory Guide for the behavior of the *Chandra* PSF with source off-axis distance). Recall that this is restricted to features found within "Mexican hat" regions having radii $\leq 8''$ (the maximum WAVDETECT scale was 16 pixels; see §3.3). We have manually inspected the resulting nine sources, and we do not find any with highly significant evidence for extent. All of the nine sources are located close to the center of the field of view, where small errors in image cross registration and satellite aspect reconstruction can most easily lead to false apparent extent. In addition, because the aim point position varied between observations (see Table 1), there is not a unique PSF applicable to all observations of any given source; apparent source extent on the scale of about an arcsecond can be introduced by variations in the applicable PSF from observation to observation. Therefore, we conclude that there are no sources found here by WAVDETECT with highly significant spatial extent. We note, however, that our constraints on the spatial extents of nearly point-like sources are limited in many cases due to small numbers of counts ($\lesssim 20$).

To investigate further any extended X-ray sources, we have searched the soft-band and hard-band images described above using the CXC's Voronoi Tessellation and Percolation detection algorithm (VTPDETECT; Ebeling & Wiedenmann 1993; Dobrzycki et al. 1999). We have used a probability threshold (i.e., a `limit` parameter) of 1×10^{-6}, and we require a minimum number of events per source (i.e., a `coarse` parameter) of 10. In our searching, we have included a "buffer" region around the Caltech area to minimize any edge effects that could affect extended sources in the Caltech area. We do not find any highly extended sources in either the soft or the hard bands. We comment that much of the apparent diffuse emission seen in some of the adaptively smoothed images (e.g., Figure 4) can be explained via a combination of instrumental background and emission in the wings of the PSFs of bright point sources.

While the methods we have used above to search for extended emission are effective and appropriate for the scope of this paper, we note that optimal extended source searching requires precise modeling of the underlying background. As improved understanding of the *Chandra* background develops, we will improve our extended source searching appropriately.

4. Multiwavelength Counterparts of the Chandra Sources

4.1. Source Matching Procedure

The multiwavelength studies of the HDF-N and its vicinity that were correlated with the X-ray detections are presented in Table 5. Listed are the number of objects in each catalog located within the Caltech area, the positional accuracy assumed, the number of objects with *Chandra* source matches, and the estimated false match rate. The positional accuracy we assumed for a given catalog was generally slightly larger than that quoted by the particular author. We assumed $\approx 0.5''$ positional accuracy for the X-ray sources (see § 3.1) and used the positional error of each catalog object to determine counterparts of X-ray detections; if a catalog object's positional offset from the X-ray source was less than the error on the object's position listed in Table 5, then a match was assumed. In practice, the X-ray positional error was only considered when an individual catalog's positional uncertainty was less than $1.0''$ (e.g., in the HDF-N itself and for the very precise radio catalogs). Additional criteria besides spatial coincidence within a catalog's errors were used when possible (e.g., the much deeper optical data in the HDF-N supersedes more shallow surveys in the optical). The estimated false match rates in Table 5 were calculated using a "random-step" technique. All X-ray sources were shifted by $7''$ to the northeast, northwest, southeast and southwest, and for each of these shifts the source matching algorithm was run. The resulting numbers of falsely matched sources were then averaged to estimate the false match rate.

The expected numbers of falsely matched sources are generally quite low, so false matches should not materially affect our results. For a few catalogs, however, the false match rate appears to be fairly high when compared to the number of *Chandra* source matches. For instance, the number of false matches expected for the W96 HDF-N catalog is 2.5, but the median R magnitude for the false matches is 28.5 whereas the *Chandra*-W96 matches had a median R magnitude of 23.4. There are zero *Chandra*-W96 false matches expected at this bright optical flux level, where the optical source density is much lower. The same effect is seen for the Hogg00 and Barger et al. (1999) catalogs. For the Hogg00 catalog, the falsely matched sources had a median R of 24.8 whereas the *Chandra*-Hogg00 matches had a median R of 23.3. For the Barger et al. (1999) catalog, the falsely matched sources had a median R of 23.6 and the *Chandra*-Barger matches had a median R of 22.6. We thus are confident that the vast majority of the *Chandra* source identifications are correct.

4.2. Optical Photometric Data

Deep I (Kron-Cousins; see Bessel 1990) and V (Kron-Cousins) band images covering the field were obtained in 1997 Apr with the UH8K CCD mosaic camera on the Canada-France-Hawaii Telescope. The 8.3 hour I-band and 11 hour V-band images were cross calibrated to shallower I and V images obtained with the University of Hawaii 2.2m telescope. A more detailed description of these imaging data may be found in Barger et al. (1999). Deep R (Kron-Cousins) band imaging was obtained using Keck LRIS during 1998 Feb and 1999 Feb. The combined 7080 s exposure, which was calibrated using Landholt standards, covers approximately half of the field. More discussion of the R-band imaging data may be found in BCR00.

For each object in the X-ray sample I, R and V magnitudes were measured using $3''$ apertures centered on the nominal X-ray position. These aperture magnitudes were then corrected to approximate total magnitudes using an offset of -0.19 mags for I, -0.22 mags for R, and -0.24 mags for V. For objects brighter than $R = 21$, isophotal magnitudes computed to 1% of the peak surface brightness were also calculated and used in place of the aperture magnitudes. For the fainter objects the isophotal magnitudes generally agree well with the aperture magnitudes. The apertures are shown superimposed on $19'' \times 19''$ I-band thumbnail images of the surrounding field in Figure 6. For a small number of objects there is an apparent optical counterpart lying within the aperture but sufficiently close to the edge that if this is the counterpart we would overestimate the magnitude of the object. In these cases we have remeasured the magnitudes with apertures centered on the optical positions; these objects have been marked in Table 6. For each image we measured a 1σ noise level by placing random apertures in the field and measuring the distribution of corrected aperture magnitudes at these positions. The 1σ levels measured in this way are 26.0 for I, 27.3 for R, and 27.1 for V.

In Table 6 we list the R and I magnitudes for the 82 *Chandra* sources. Where no direct R measurement is available we have used the relation:

$$R = I - 0.2 + 0.5(V - I) \tag{1}$$

This relation was computed as a fit to the R magnitudes in the observed region to determine the R magnitudes from the V and I observations. The 1σ dispersion of the fitted objects is 0.18 mags, and 97% lie within 0.4 mags of this relation. The computed R magnitudes should be accurate to this level which is sufficient for the present work.

When needed, we quote 2σ lower limits on R and I magnitudes in Table 6. There are a few additional sources for which deeper data were available (e.g., in the HDF-N itself).

Six of the 62 soft-band sources have no optical counterparts to $R \approx 26.5$. Four of these soft-band sources have neither hard-band nor full-band counterparts and were detected with fewer than 6 counts; some of these may be false X-ray detections (see § 3.3). Only one of the 45 hard-band sources has no optical counterpart to $R \approx 26.5$ (CXOHDFN J123648.3+621456); it has a full-band counterpart. There were an additional two sources lacking optical counterparts which were detected in the full band (0.5–8 keV) but in neither the soft band nor the hard band.

There are a total of nine *Chandra* sources with no optical counterparts to $R \approx 26.5$ and $I \approx 25.3$. These nine sources also had no counterparts in the Hogg00 $K_{\rm s}$ image as determined from our manual inspection. Our results on optical counterparts are consistent with those of G01, who find optical counterparts for 90% of their X-ray sources. Due to the potentially false detections of some of the faintest X-ray sources in our sample, we also consider only X-ray sources detected with full-band fluxes $> 7 \times 10^{-16}$ erg cm^{-2} s^{-1}; we find that only 1 of 57 (1.8%) lacks an optical counterpart to $R \approx 26.5$.

We have compared our sources with those of Barger et al. (2001, hereafter B01) using their criteria for "optically faint" ($I > 23.5$). Of the 45 hard-band sources, 18 (40%) have $I > 23.5$ compared with seven of the 20 (35%) B01 hard-band sources. The two surveys are consistent within the statistics; note that the current survey is more than twice as deep as that of B01. More optically faint counterparts are expected as extremely faint hard-band X-ray flux limits are reached (see § 5.1 for discussion of R versus X-ray flux).

The other main source of optical photometric data used in this paper is the catalog of Hogg00. We also used the deep $\mathcal{R}$ image of Hogg00 (kindly provided to us by C. Steidel and D. Hogg) for cross-calibration purposes. Colors discussed in this paper are in the $U_{\rm n}$, G, and $\mathcal{R}$ filters as used by Hogg00 and described in Steidel & Hamilton (1993), except where otherwise indicated. The $U_{\rm n}$, G, and $\mathcal{R}$ filters have effective wavelengths of 3570, 4830, and 6930 Å, FWHM bandpasses of 700, 1200, and 1500 Å, and zero-magnitude flux densities of roughly 1550, 3890, and 2750 Jy. These magnitudes are normalized to Vega. Also included in our data analysis are $\mathcal{R} - K_{\rm s}$ colors as calculated by Hogg00; the $K_{\rm s}$ filter has an effective wavelength of 2.15 μm, a FWHM bandpass of 0.3 μm, and a zero-magnitude flux density of roughly 708 Jy. The $\mathcal{R}$ band is related to the Kron-Cousins R and I bands by the following relation from Steidel & Hamilton (1993):

$$\mathcal{R} = R + 0.24 - 0.28(R - I) \tag{2}$$

5. Optical Properties of the Chandra Sources

In this section we describe the bulk optical properties of the *Chandra* sources in the Caltech area. Detailed descriptions of individual sources are given in §A, and an update on X-ray source detections in the HDF-N itself is given in §6.

5.1. Optical Fluxes and Colors

The median R magnitude of the 73 *Chandra* sources in the Caltech area with optical detections is ≈ 23.7. The color distributions of our X-ray-optical matches are shown in Figure 7; these colors were calculated by Hogg00. The two X-ray detected M stars stand out in several plots; they have colors that are redder than most of the catalog objects. X-ray detections with $20 < \mathcal{R} < 23$ tend to be redder than the average galaxy (most easily seen in the $\mathcal{R} - K_{\rm s}$ versus $\mathcal{R}$ plot). There also seems to be an excess of objects with $4 < \mathcal{R} - K_{\rm s} \lesssim 5$ as compared to the field galaxy population. Three X-ray sources have colors that are bluer than the general galaxy population; these bluer objects are most evident in the $U_{\rm n} - G$ versus $\mathcal{R}$ and $G - \mathcal{R}$ versus $\mathcal{R}$ plots. Optical spectra of all of these blue objects show broad lines; they are all AGN and are fairly luminous ($L_{0.5-8} \approx 10^{43-44}$ erg s^{-1}).

Figure 8 shows the relationship between R magnitude and soft-band and hard-band X-ray flux. We have plotted several values of the X-ray to optical flux ratio, $\log(\frac{f_{\rm X}}{f_{\rm R}})$, on this figure. This ratio was derived using the Kron-Cousins R filter transmission function:

$$\log\left(\frac{f_{\rm X}}{f_{\rm R}}\right) = \log f_{\rm X} + 5.50 + \frac{R}{2.5} \quad (3)$$

(compare with Figure 1 of Maccacaro et al. 1988). The majority of the X-ray sources in the current survey fall within $\log(\frac{f_{\rm X}}{f_{\rm R}}) = 0.0 \pm 1$. This range of values is typical of sources found in the wider field X-ray surveys of Schmidt et al. (1998) using *ROSAT* and Akiyama et al. (2000) using *ASCA*; it is that typical of AGN in the local Universe. There are a few sources, however, that deviate from $\log(\frac{f_{\rm X}}{f_{\rm R}}) = 0.0 \pm 1$. Two of these sources are spectroscopically identified M stars (see §A.1 and Table 6), which have the expected $\log(\frac{f_{\rm X}}{f_{\rm R}}) \approx -2$.

At the faintest soft-band fluxes ($< 3 \times 10^{-16}$ erg cm^{-2} s^{-1}), there is an interesting group of 7 sources which are X-ray weak for their optical fluxes (see Figure 8). These are seen only below the flux limits of the deepest pre-*Chandra* soft-band surveys (e.g., Schmidt et al. 1998). These sources are all relatively nearby ($z < 0.5$) low X-ray luminosity objects that are described in §5.4.

There are also three objects which are notably faint in the optical with respect to their X-ray flux values; these sources are of interest because they may represent a new class of astronomical object (e.g., extremely high redshift quasars). The three sources are found to be optically faint with respect to their hard-band fluxes, one of these is also found to be optically faint with respect to its soft-band flux. This soft-band source, CXOHDFN J123704.8+621601, is relatively bright and has X-ray band ratio of $0.45^{+0.14}_{-0.11}$. Its optical counterpart has $R = 25.4$ and is discussed in §A.3. One of the other two sources is the Type 2 QSO candidate in the HDF-N itself (CXOHDFN J123651.7+621221; see H00). The third source is CXOHDFN J123616.0+621107, which in addition to being optically faint is anomalously hard for its soft-band count rate (see Figure 5). The X-ray and optical properties point to a possible extreme AGN; this object is discussed in detail in §A.3.

5.2. Optical Spectroscopic Observations with Keck and the Hobby-Eberly Telescope

Extensive spectroscopic and photometric redshift studies have been carried out in the HDF-N region (e.g., Fernández-Soto et al. 1999; C00). We have supplemented these efforts by obtaining spectra of X-ray sources in the Caltech area using the Keck and Hobby-Eberly Telescopes. This section describes our spectroscopic work.

Of the 82 X-ray sources, 25 have optical counterparts brighter than $R = 23$ (including two stars, which are excluded from most of the analysis in this paper). A total of 32 redshifts were found from both the literature and our optical spectroscopy, including 24 of the 25 sources with $R < 23$ and eight sources with $R > 23$. The majority of the redshifts are from C00; we provide an additional six previously unpublished redshifts from four Keck spectra and two HET spectra. We also present a few additional spectra which were taken in order to provide more information about the nature of the individual objects.

Keck Low Resolution Imaging Spectrograph (LRIS; Oke et al. 1995) spectra were obtained on 2000 March 7 and earlier (L.L. Cowie 2000, private communication). These were taken using two slit-masks oriented at PA= 90°. Each mask was observed at three positions (steps were $\approx 1.5''$ along the slits) with 1200 s per exposure. The 300 line mm^{-1} grating was used with central wavelength 6700 Å. The night was photometric with seeing of $\approx 0.8''$. Keck Echellette Spectrograph and Imager (ESI; Epps et al. 1998) observations were taken on 2000 April 1–2 in low-resolution mode using a $1''$ slit. Exposure times were 300, 420, or 600 s at each position; most targets were observed at three positions 2–$3''$ apart along the slit (brighter targets were observed at two positions only), and the spectral resolution was ≈ 17 Å. Both nights were photometric with seeing of $0.6''$ the first night and $0.9''$ the second night. The band pass for both the Keck LRIS and ESI is $\approx$ 5000–10000 Å.

Spectra were also obtained using the Marcario Low Resolution Spectrograph (LRS; Hill et al. 1998a,b; Schneider et al. 2000) of the Hobby-Eberly Telescope (HET; Ramsey et al. 1998). The HET operates in queue mode, so the observations occurred on multiple evenings between 2000 February 7 and 2000 June 2. A $2.0''$ slit and a 300 line mm^{-1} grism/GG385 blocking filter produced spectra from 4400–9000 Å at 17 Å resolution; points redward of 7700 Å are suspect because of possible second-order contamination. The exposure time per source ranged from 5–60 m. The image quality was typically $2.5''$ (FWHM). Wavelength calibration was performed using HgCdZn and Ne lamps, and relative flux calibration was performed using spectrophotometric standards.

The spectra are shown in Figure 9, and individual descriptions are given in §A.1.

5.3. Redshifts, Luminosities, and Classifications of the Chandra Sources

5.3.1. Redshifts and Luminosities

The 32 sources in the X-ray sample for which we have redshifts have their redshift information listed in Table 6. Only two redshifts were derived using photometric data; all others are spectroscopic. The sources with redshifts are fairly evenly distributed with respect to X-ray count rate and band ratio (see Table 4); at least in terms of these properties, they appear to be representative of the X-ray source population as a whole.

The median redshift of the sample is 0.76, but the spread is quite large (see Figure 10). About 90% of the redshifts are uniformly distributed in redshift space for $0 < z < 1.5$. There exist two groups of two objects each at $z \approx 2.6$ and $z \approx 3.4$. This possible redshift "clustering" is interesting, but until more redshifts are obtained above $z \approx 1.1$ we cannot determine whether this clustering is real or merely an artifact of the small number of sources.

Full-band, soft-band and hard-band luminosities are given for the sources with redshifts in Table 6; these are calculated for the rest frame. The soft-band and hard-band luminosities are plotted versus redshift in Figure 11. We have found no strong correlations between either soft-band or hard-band luminosity and band ratio.

5.3.2. Classification Scheme

It is physically unreasonable to try to cast all of the X-ray sources into a few sharply defined classes. The classifications chosen below are designed to provide some insight into the general nature of the population, but many of the sources could possibly belong to several of the categories (e.g., a heavily obscured AGN that also shows circumnuclear starburst activity). Objects that are not confirmed AGN by our optical spectroscopic criteria are placed in two "galaxy" categories based on their X-ray luminosities. These "galaxies" lack known AGN-defining spectral features in the optical band. Finally, we have a category for Galactic stars.

These various categories are briefly described as follows:

• **BL AGN and NL AGN:** We follow the classification schemes of Schmidt et al. (1998) and B01 in that AGN must have (1) broadened emission lines (FWHM > 500 km s^{-1}) or (2) emission from either [Ne V] or [Ne III]. AGN are classified as either broad-line (BL AGN, FWHM of emission lines > 1000 km s^{-1}) or narrow-line (NL AGN). We identify 15 of the 30 extragalactic sources as AGN, including eight spectroscopically identified BL AGN and QSOs.

• **Low X-ray Luminosity Galaxies (LL):** Low-luminosity galaxies ($L_{0.5-8} < 10^{41.5}$ erg s^{-1}; see §5.4) are objects in which the X-ray source can plausibly be explained by moderate-strength starbursts, hot gas in elliptical galaxies, or other sources besides accretion onto a nuclear supermassive black hole (although accretion onto a supermassive black hole is still a viable possibility for some of these objects). There are eight sources in this category; only one is detected in the hard band.

• **High X-ray Luminosity Galaxies (HL):** The seven objects classified as HL galaxies are all detected in the hard band and have hard-band X-ray luminosities $\gtrsim 10^{42}$ erg s^{-1} (three are detected in *only* the hard band), strongly suggesting that these objects are actually AGN. They stand in contrast to the low-luminosity X-ray galaxies, which are generally detected only in the soft band (see § 5.4). In some cases, we were unable to assess the AGN nature of the object due to lack of access to the optical spectrum.

• **Stars:** Two M4 stars are included in the sample. A curious difference between our sample and that of G01 is that none of the optically bright, X-ray faint objects in the G01 sample are identified as stars, whereas two of our optically bright, X-ray faint sources are spectroscopically identified as stars (one would expect more in the larger field of G01). Figure 8 shows the location of the stars in a plot of R magnitude versus X-ray flux.

A summary of the optical spectroscopic classifications of the *Chandra* sources in the Caltech area is given in Table 7. This table separates the objects by the X-ray band (soft or hard) in which they were detected, in addition to giving the total number of objects in each class (regardless of X-ray nature).

We plot $\mathcal{R}$ magnitude versus redshift in Figure 12, breaking the source redshifts shown in Figure 10 into separate spectroscopic classes. The four higher redshift ($z > 2$) objects are all luminous QSO-type AGN. At $z \approx 1$, there is a mixture of BL AGN, NL AGN, and HL galaxies. At $z \approx 0.5$, there is a mixture of NL AGN, HL galaxies, and LL galaxies (see §5.4). Finally, at the brightest $\mathcal{R}$ magnitudes and lowest redshifts, the sources are LL galaxies and stars. We estimate the fraction of optically selected sources that are X-ray sources in a manner similar to that of B01 (see their § 5). We find that the fraction of galaxies with $-22.5 < M_{\mathcal{R}} < -24$ having counterparts in the X-ray band is 0.06 ± 0.03, fully consistent with the $0.07^{+0.05}_{-0.03}$ fraction found by B01.

5.3.3. Comparison of Classifications with Other Samples

We can compare our 20 hard-band classifications with the 13 sources in the complete 2–10 keV sample of B01. The survey of B01 reached 3.8×10^{-15} erg cm^{-2} s^{-1} in the 2–10 keV band (our limit in the 2–10 keV band is $\approx 8.1 \times 10^{-16}$ erg cm^{-2} s^{-1}). We find a comparable fraction of AGN in the hard band; 11 of 20 (55%) hard-band objects with identifications in our sample are spectroscopically confirmed AGN, while 7 of 13 (54%) hard-band objects in B01 are spectroscopically confirmed AGN.

Our soft-band classifications are most suitably compared with the *ROSAT* Ultra Deep Survey (UDS) work of Lehmann et al. (2001), who have obtained optical spectra for 85 of the 91 soft-band X-ray sources in the Lockman Hole. The limiting 0.5–2 keV flux for the *ROSAT* UDS is 1.2×10^{-15} erg cm^{-2} s^{-1} (compared to 1.3×10^{-16} erg cm^{-2} s^{-1} for this paper). To account for the increased number of low-luminosity galaxies seen at very faint soft-band fluxes (see § 5.4), we compare only our 13 sources with soft-band fluxes $> 1.2 \times 10^{-15}$ erg cm^{-2} s^{-1} to the Lehmann et al. (2001) sample. We have spectroscopic identifications for 10 of those 13 sources; 6 are broad-line AGN, one is a narrow-line AGN, and three objects fall into the "galaxies" categories. Of 85 objects with spectroscopic identification in the *ROSAT* UDS, 56 are broad-line AGN, and 13 are Type 2 AGN; our survey is thus consistent with the *ROSAT* UDS after accounting for the small number of sources in our survey at the relevant flux level. In our entire identified soft-band sample (see Table 7), however, the percentage of AGN is not quite as high as that of the Lehmann et al. (2001) sample, mainly due to the increased prevalence of low-luminosity X-ray emitting galaxies at very faint soft-band fluxes ($< 3 \times 10^{-16}$ erg cm^{-2} s^{-1}; see § 5.4).

5.4. Low-Luminosity X-ray Emitting Galaxies

As mentioned in §5.3, a group of low-luminosity ($L_{0.5-2} < 10^{41.5}$ erg s^{-1}) soft X-ray sources appears at faint soft-band flux levels. Seven of these sources are visible as a group in Figure 8a, appearing at faint X-ray fluxes ($\lesssim 3 \times 10^{-16}$ erg cm^{-2} s^{-1}) and bright optical fluxes ($R \lesssim 21$). There is one additional faint X-ray source that was not detected independently in either the soft or the hard X-ray bands; this full-band source, CXOHDFN J123702.0+621123, has properties similar to the other low-luminosity sources. We also place CXOHDFN J123656.9+621301, an elliptical galaxy in the HDF-N, in this category based on its lower X-ray luminosity, although it is more optically faint ($R = 23.4$).

All of these objects are galaxies at moderately low redshift, z = 0.089–0.56, and most have absorption-dominated or "intermediate" type optical spectra, where the spectrum is not dominated by emission (C00). The constraints on their X-ray spectral properties are not strong due to low numbers of counts; the typical X-ray band ratio upper limit is < 1.20. All but one source (CXOHDFN J123656.9+621301) is undetected in the hard band; the hard-band luminosity upper limits are $\leq 10^{41.7}$ erg s^{-1}. The one hard-band detected source has $L_{2-8} \approx 10^{41.6}$ erg s^{-1}. Furthermore, their optical luminosities are typical of galaxies rather than AGN; most have $L_{\rm R} \approx 0.3 L_{*}$. While the newly discovered X-ray source in the HDF-N itself (CXOHDFN J123644.0+621249; see §6) does show signs of containing a weak AGN, several of these sources do not show optical evidence of harboring AGN in fairly high quality optical spectra. In the rest of the cases, however, we lack the high-quality optical spectroscopy to determine if there is a weak AGN present. This group of objects is important regardless of the presence of AGN, as they are either examples of very low-luminosity AGN or the bright end of the "normal" galaxy X-ray luminosity function.

G01 also mention this population (see their Figure 7). Of the 7–8 optically bright, X-ray faint sources in the G01 sample, five have soft-band X-ray fluxes $\gtrsim 3 \times 10^{-16}$ erg cm^{-2} s^{-1}. These sources are identified by G01 as galaxies. The nature of this optically bright, X-ray faint population can only be studied with *Chandra* exposure times longer than 100 ks, necessary to reach the required soft-band X-ray flux level ($\approx 3 \times 10^{-16}$ erg cm^{-2} s^{-1}). Even deeper observations may reveal that

AGN cease to dominate the X-ray number counts at extremely faint soft-band fluxes in a manner analogous to the dominance of star-forming galaxies rather than AGN at very faint radio flux densities (see §7.1 for a discussion of μJy radio sources). This is perhaps not surprising, as one would expect less luminous, nearby X-ray sources (similar to M82, for example; e.g., Griffiths et al. 2000) to appear as X-ray surveys achieve greater sensitivities. It had previously been proposed that starburst galaxies may contribute to the X-ray background; some of these observed objects could very well be the early evidence of this population (e.g., Moran, Lehnert, & Helfand 1999 and references therein).

6. Chandra Sources in the HDF-N

6.1. Newly Discovered X-ray Sources

With the addition of 58.2 ks of *Chandra* exposure to the 164.4 ks discussed by H00, we have detected two new sources in the HDF-N: CXOHDFN J123639.6+621230 and CXOHDFN J123644.0+621249 (see Figure 13). A total of eight X-ray sources have now been discovered in the HDF-N; all six HDF-N sources of H00 are still detected in the 221.9 ks observation. At present, all eight of the X-ray sources found in the HDF-N have likely optical counterparts.

CXOHDFN J123639.6+621230 is identified with an $R = 24.3$ broad-line AGN classified by C00; the X-ray detection supports the AGN nature of this source. The W96 match, 4-852.12, is $0.41''$ from the X-ray source position (see Figure 13). C00 report $z = 0.943$ from the detection of a single broad emission line which they take to be Mg II at 2800 Å. Fernández-Soto et al. (2001) note that the expected colors of an AGN at $z = 0.943$ do not match the photometric properties of this source in the near-infrared and that a much better match is found at $z = 3.475$, in which case the broad emission line is Lyα. The C00 redshift has recently been revised to $z = 3.479$ (J.G. Cohen 2000, private communication). The corresponding rest-frame 0.5–8 keV luminosity is 1.4×10^{44} erg s^{-1}.

CXOHDFN J123644.0+621249 was detected with only five X-ray counts and only in the soft band. It is located $0.34''$ from an $R = 21.3$ object with characteristics of an AGN, however, so we have fairly high confidence that the detection is real. This source is a 1.4 GHz and 8.4 GHz emitter with $z = 0.557$ (R98; R00; C00). A Keck spectrum of the object is presented in Figure 8. The spectrum shows clear [O II] emission and has weak Hβ and perhaps [O III] lines. The Hβ line is resolved with a FWHM of ≈ 600 km s^{-1}, suggesting the presence of an AGN. This source is also discussed by R98, who report [O II], [O III] and Hβ lines with P Cygni profiles; we do not see such profiles in the current data (see Figure 8). The 8.5 GHz radio luminosity is $10^{22.5}$ W Hz^{-1}, and R98 estimate a star-formation rate of 30 $M_\odot$ yr^{-1}. The rest-frame soft-band luminosity of this source is 1.3×10^{42} erg s^{-1}, which would be high for a pure starburst galaxy. The broad Hβ line, combined with the large X-ray luminosity, suggest the presence of an AGN.

6.2. New Hard X-ray Detections of Elliptical Galaxies

All three of the HDF-N elliptical galaxies reported by H00 were undetected in the hard band with the 164.4 ks of exposure time used by H00. With the addition of 57.5 ks of exposure, two of these sources, CXOHDFN J123655.4+621311 and CXOHDFN J123656.9+621301, are now detected in the hard band with 5.5 ± 2.5 and 7.4 ± 2.8 hard-band counts, respectively. Their hard-band luminosities are 1.9×10^{42} erg s^{-1} and 4.0×10^{41} erg s^{-1}, respectively. The luminous hard components revealed from these sources strengthen the case that they harbor AGN; an AGN was already suspected in CXOHDFN J123655.4+621311 given its flat radio spectrum (R98; H00). The soft-band luminosities of CXOHDFN J123655.4+621311 and CXOHDFN J123656.9+621301 are somewhat higher than expected for normal ellipticals but are not outside the range seen for these objects.

Fernández-Soto et al. (2001) have argued that CXOHDFN J123656.9+621301 is at a higher redshift than the value of $z = 0.474$ stated by C00, giving $z = 1.270$. They suggest that the spectroscopic redshift is in error due to confusion with a nearby source, even though C00 list it as being secure and based on multiple spectral features. We cannot resolve this issue with the X-ray data, although we note that the X-ray detection may make an unusual intrinsic spectral energy distribution for this object more plausible. If CXOHDFN J123656.9+621301 is indeed at $z = 1.270$ rather than $z = 0.474$, it would have a full-band X-ray luminosity of 5.2×10^{42} erg s^{-1} rather than 6.5×10^{41} erg s^{-1} (3.2×10^{41} erg s^{-1} was quoted in H00 where $q_0 = 0.5$ and $\Gamma = 2$ were used). This would make the case for the presence of an AGN even stronger.

7. Chandra Constraints on Source Populations at Other Wavelengths

7.1. The μJy Radio Sources

While surveys of radio sources are dominated by powerful AGN at flux densities above a few mJy, a large population of lower luminosity galaxies becomes visible at fainter limits (e.g., Windhorst et al. 1985). About 60% of these μJy radio sources are thought to be starburst-type systems associated with disk galaxies at moderate redshift (e.g., Muxlow et al. 1999; R00; and references therein); and approximately 30% of μJy radio sources are thought to be low-luminosity AGN often identified with field ellipticals. The remaining 10% are associated with red, optically faint ($I > 25$; $I - K > 3$) systems which may be luminous dust-shrouded starbursts at $z \approx 1$–3, luminous obscured AGN, or extreme redshift ($z > 6$) AGN (e.g., Richards et al. 1999).

Extremely deep radio coverage of the HDF-N and its environs has been obtained using the VLA (R98; R00), MERLIN (Muxlow et al. 1999; Richards 1999), and the WSRT (Garrett et al. 2000). We have used the *Chandra* data to set constraints on the X-ray emission properties of the sources detected in these surveys. Most of the radio surveys above have been performed at 1.4 GHz, so we shall first focus on the X-ray properties of sources selected at this frequency. In §7.1.4 we shall return to discuss radio sources detected at 8.5 GHz that are not detected at 1.4 GHz (R98).

The μJy radio sources in the HDF-N and its environs may be classified based upon their radio spectral indices and radio morphologies. Starburst-type objects have steep radio spectra ($S_\nu \propto \nu^{-\alpha}$, $\alpha > 0.5$) and appear extended on sub-galactic scales. AGN candidates generally have flat or inverted radio spectra ($\alpha < 0.5$) together with a compact core and one or two-sided extended radio structure. In some cases optical morphology and infrared properties can also be used in the classification process (see Richards 1999). Muxlow et al. (1999) and Richards (1999) have reported 31 starburst-type 1.4 GHz sources and six AGN-candidate 1.4 GHz sources in the Caltech area (see Chapter 4 of Richards 1999). They also have found 30 1.4 GHz sources in the Caltech area that they cannot easily classify as either of these types (hereafter these are referred to as objects of unknown type). Their classifications were intended to identify the origin of the bulk of the radio emission from a particular galaxy; they did not preclude starburst-type objects from containing embedded AGN or AGN candidates from also having starburst activity. With *Chandra* we detect 11 of the starburst-type sources, two of the AGN candidates, and three of the unknown-type objects (see Table 8 and Figure 14). It is worth noting that the X-ray detection fraction for the μJy sources of unknown type is significantly lower than for the starburst-type and AGN-candidate μJy sources, but it is difficult to examine this issue in detail due to the limited information on the unknown-type objects. Below we will discuss the starburst-type and AGN-candidate μJy sources in further detail.

7.1.1. Radio Starburst-Type Systems

In Figure 14 we plot the 1.4–8.5 GHz spectral index versus the 1.4 GHz flux density for the 1.4 GHz sources in the Caltech area; we have marked the sources detected by *Chandra*. Notably, within our limited statistics, the $\approx$ 35% *Chandra* detection fraction for the starburst-type radio sources is comparable to that for the radio AGN candidates (see §7.1.2). The X-ray detection fractions are comparable in both the soft and the hard bands.

The 11 *Chandra*-detected, starburst-type radio sources have typical redshifts of 0.3–1.0 and a range of X-ray band ratios. They are uniformly distributed among the population in terms of 1.4 GHz flux density and 1.4–8.5 GHz spectral index (see Figure 14). The high X-ray luminosities ($\gtrsim 5 \times 10^{42}$ erg s^{-1}) and large band ratios of several of these systems strongly suggest that they contain previously unrecognized AGN. Others have X-ray luminosities that are comparable to, or only slightly higher than, those of the most powerful starbursts in the local Universe (e.g., Moran, Lehnert, & Helfand 1999).

Considering the starburst-type radio population as a whole, including the $\approx$ 65% of sources not detected in X-rays, the present *Chandra* data are still consistent with the idea that the majority of these objects are predominantly powered by star formation.

7.1.2. Radio AGN Candidates

Two of the six radio AGN candidates seen at 1.4 GHz in the Caltech area are detected by *Chandra*: J123646.3+621404 and J123652.8+621444 (see Figure 14). The first is a well-known AGN in a spiral galaxy at $z = 0.960$ that is located in the HDF-N; its X-ray detection was reported by H00. J123652.8+621444 is at $z = 0.322$ and has an $R = 19.5$ elliptical host. Its radio spectrum is inverted with $\alpha = -0.12$, and it shows radio variability on a timescale of months.

The non-detections of several radio AGN candidates by *Chandra* are notable given the fact that a few of these systems are at low redshift and are optically bright. For example, J123716.3+621512 ($z = 0.232$; $I = 19.8$; $\mathcal{R} = 20.3$; $\alpha = 0.41$) is undetected; assuming a $\Gamma = 1.4$ power law (see §3.3), the limit on its 0.5–8 keV emission is $< 3.9 \times 10^{40}$ erg s^{-1}. If this source is indeed an AGN, it must be either intrinsically X-ray weak, perhaps due to low radiative efficiency accretion, or it must have heavy obscuration up to ≈ 10 keV with little X-ray scattering.

Another remarkable AGN in the Caltech area that is not detected in the *Chandra* data is the Fanaroff-Riley I (FR I) Wide Angle Tail (WAT) radio source J123725.7+621128 (Muxlow et al. 1999; Richards 1999). With a 1.4 GHz flux density of 6.0 mJy, this object is one of the brightest radio sources in our field (it is not shown in Figure 14 because it lies beyond the right-hand edge of the plot). J123725.7+621128 is located in the *HST* flanking fields, and its host galaxy is a $K = 18.8$, $I = 22.9$, $\mathcal{R} = 24.5$ elliptical of unknown redshift. Application of the K-z relation (e.g., Eales et al. 1997) to this galaxy suggests a redshift of $z = 1$–2. FR I sources generally have low X-ray luminosities (10^{41}–10^{42} erg s^{-1} from 2–10 keV; e.g., Sambruna, Eracleous & Mushotzky 1999), and an X-ray luminosity somewhat below our detection limit would still be consistent with the X-ray properties of some local FR Is (e.g., the FR I in Hydra A; McNamara et al. 2000). WAT sources are often associated with rich groups or clusters; we discuss the nondetection of extended X-ray emission from a group or cluster in §7.6.

Similarly, the 0.42 mJy FR I in the HDF-N, J123644.3+621133 (R98), is not detected even with 221.9 ks of exposure time, although there is a hint of a soft-band photon excess (≈ 5 counts) at its position (see §3.2 of H00).

7.1.3. Optically Faint μJy Sources

The HDF-N itself contains three optically faint μJy sources, as defined above, at 1.4 GHz. As described by H00, one of these three (J123651.7+621221) is detected by *Chandra* and is a good candidate for a Type 2 QSO at $z \approx 2.7$. Encouraged by this result, we have searched for other optically faint μJy radio sources with X-ray matches, but we find only one further X-ray match among the 17 sources listed in Richards et al. (1999). The low matching fraction with X-ray sources is consistent with these objects being predominantly powered by starburst activity, although our constraints are difficult to quantify as most of these objects do not have measured redshifts.

The one further X-ray match is with J123711.9+621325 (see Figure 3 of Richards et al. 1999) which has a 1.4 GHz flux density of 54 μJy and a steep radio spectrum with $\alpha > 1.16$. J123711.9+621325 does not have a measured redshift at present. It presumably contains an AGN in addition to likely starburst activity, but the limited amount of information available for this source combined with its low X-ray flux (see Table 8) prohibit detailed interpretation.

7.1.4. Sources Detected at 8.5 GHz but not 1.4 GHz

In addition to the radio sources in the Caltech area that are detected at 1.4 GHz, there are 25 faint radio sources that R98 detect at 8.5 GHz that are not also detected at 1.4 GHz. Eight of these sources are in their main catalog (i.e., their Table 3) and 17 are in their supplemental catalog (i.e., their Table 5). These sources, of course, tend to have flatter radio spectra than those selected at 1.4 GHz and thus might contain a higher fraction of AGN (e.g., §6 of R00).

With *Chandra* we only detect two of these sources: J123655.4+621311 and J123658.8+621435.[7] J123655.4+621311 is in the HDF-N itself and is discussed above in §6.2 and in H00; it appears to contain a fairly low-luminosity AGN. J123658.8+621435 is identified with a face-on spiral at $z = 0.678$. Its radio spectrum is flat ($\alpha < 0.44$), but we are not aware of any claimed AGN in this object; C00 state that the spectrum is intermediate between an emission-line and an absorption-line spectrum. The HET spectrum of this object is given in Figure 8, and more discussion is included in §A.1.

If we alternatively look at the entire 8.5 GHz source population in the Caltech area, irrespective of 1.4 GHz detections, ten of the 48 sources at 8.5 GHz are detected by *Chandra*.

7.1.5. Far-Infrared Luminosities Estimated from 1.4 GHz Flux Densities

We have used 1.4 GHz flux densities to estimate the bolometric far-infrared luminosities of the *Chandra* sources with redshifts (Figure 15), following §6.3 of B01. Two of the radio-detected sources in the current sample appear to be ultraluminous far-infrared galaxies (ULIGs) while the rest have lower luminosities. These two ULIGs, CXOHDFN J123646.3+621404 and CXOHDFN J123651.7+621221, are both in the HDF-N itself and are detailed in H00; the ULIG status of CXOHDFN J123651.7+621221 should be treated with caution since its redshift is photometric. Figure 15b does not reveal any strong difference between the far-infrared luminosities of *Chandra* sources selected in the soft and hard bands.

---

[7] We note that the 8.5 GHz source J123644.0+621249 is not detected by Richards et al. (1999) at 1.4 GHz but is detected by Garrett et al. (2000) at this frequency. For this reason, we do not include it in the sample of X-ray sources detected at 8.5 GHz but not 1.4 GHz.

7.2. The Submillimeter Sources

In H00 we presented 164.4 ks *Chandra* constraints on the five submillimeter sources in the HDF-N itself (Hughes et al. 1998) as well as on the five most significant ($> 3\sigma$) submillimeter sources reported in the vicinity of the HDF-N (BCR00). None of these sources was detected at high significance with 164.4 ks of data, and this also holds with the 221.9 ks of data now available. With the new data the constraints on $\alpha_{\rm sx}$, the 850 μm to 2 keV spectral index, given in Table 1 of H00 are tightened by $+0.022$ on average. This tightening of constraints does not qualitatively change the basic conclusion reported by H00: these submillimeter sources appear to be dominated by star formation or have Compton-thick nuclear obscuration and little circumnuclear X-ray scattering.

We do note, however, that manual inspection of the full-band *Chandra* image suggests an X-ray photon excess coincident with the BCR00 submillimeter source J123646.1+621448. We have run WAVDETECT over this area of the full-band image using a less conservative probability threshold of 5×10^{-6}, and we detect a 6.9-count source coincident with J123646.1+621448. J123646.1+621448 is optically faint with $R = 25.5$, and its 850 μm flux density is 10.7 mJy. A spectroscopic redshift is not available for this source, but BCR00 estimate $z = 1.6$–3.1 with a millimetric redshift technique. If this redshift is correct, the implied X-ray luminosity of $\sim 10^{43}$ erg s^{-1} suggests that a moderate-strength AGN is present in this source.

We have stacked *Chandra* images of nine of the submillimeter sources mentioned above to derive the tightest possible constraints upon $\alpha_{\rm sx}$ for the average X-ray weak submillimeter source; we excluded J123646.1+621448 (see the previous paragraph). Our effective exposure time is 1.86 Ms, derived from the stacked exposure map. No photon excesses are apparent in the stacked soft-band or hard-band submillimeter source images. Unfortunately, the limited accuracy of the submillimeter source positions limits the efficacy of the stacking technique since one must allow for source-to-source offsets that are considerably larger than the *Chandra* PSF. We have used a $3''$-radius source cell for count extraction from the stacked images, and we are background limited in this source cell. Our 3σ upper limits on the numbers of soft-band and hard-band counts in the stacked images are 13.4 counts (3.2×10^{-17} erg cm^{-2} s^{-1}) and 17.2 counts (1.9×10^{-16} erg cm^{-2} s^{-1}), respectively. The corresponding soft-band $\alpha_{\rm sx}$ limit is $\alpha_{\rm sx} > 1.45$, and the hard-band limit is $\alpha_{\rm sx} > 1.33$ (compare with Figure 2 of H00). These $\alpha_{\rm sx}$ limits have been computed with the same X-ray spectral shape assumptions used by H00, and we have used the weighted mean 850 μm flux density of 3.92 mJy.

H00 also noted *Chandra* detections of two of the 2.8σ submillimeter sources reported by BCR00: J123616.1+621513 and J123629.1+621045. The X-ray properties of these sources, derived from 221.9 ks of *Chandra* data, are reported in Table 4.

More detailed analysis and interpretation of the submillimeter sources in the HDF-N and its vicinity will be presented by Barger et al., in preparation.

7.3. The *ISO*-CAM Sources

Infrared surveys, like X-ray surveys, are a powerful probe of the obscured Universe. The *Infrared Space Observatory* (*ISO*) has performed a deep survey of the HDF-N and its environs with the infrared imaging instrument *ISO*-CAM; at present this is the deepest survey ever made at 15μm and is also very deep at 6.75μm (see A99 and references therein). The *ISO*-CAM survey covers all of the HDF-N as well as some of its flanking fields, although the total area covered is still only about a quarter of the Caltech area. The sensitivity of the *ISO*-CAM survey was generally highest for the HDF-N itself and dropped off outside it (see §6 of A99 for details). A99 have presented the most recent analysis of the *ISO*-CAM survey data, finding 49 "main" sources and 51 "supplementary" ones; Aussel (1999) provides an update on the supplementary sources and states that the vast majority with flux densities above 100 μJy are real. We have matched the *Chandra* sources with the *ISO*-CAM sources of A99, adopting $3.5''$-radius error circles for the *ISO*-CAM sources following Aussel (1999). In total, we find seven matches with the main *ISO*-CAM sources and four with the supplementary *ISO*-CAM sources.

The HDF-N itself contains eight *Chandra* sources, 18 main *ISO*-CAM sources, and 15 supplementary *ISO*-CAM sources. A remarkable finding is that six of the eight *Chandra* sources in the HDF-N itself have matches with *ISO*-CAM sources (see Table 9 and Figure 16). Three of these matches are with main *ISO*-CAM sources, and three are with supplementary *ISO*-CAM sources. This high matching fraction bodes well for future sensitive infrared observations (e.g., with the *Space Infrared Telescope Facility*) of sources found in deep X-ray surveys, as well as for large-area infrared/X-ray surveys such as the European Large-Area *ISO* Survey (ELAIS). Furthermore, we note that five of the six *Chandra*/*ISO*-CAM matches in the HDF-N are also detected at 8.5 GHz by R98. Most *ISO*-CAM sources, however, do not have *Chandra* source matches; this is as expected given that the surface density of *ISO*-CAM sources on the sky is much higher than that of *Chandra* sources. The nature of the HDF-N *Chandra* sources with *ISO*-CAM matches is discussed in detail in §6 and in H00; at least four of them show fairly secure signs of hosting AGN. These AGN presumably heat dust in their environments to produce the emission seen by *ISO*-CAM (see Wilman, Fabian, & Gandhi 2000 and Alexander et al. 2001).

Outside the HDF-N, where the sensitivity of the *ISO*-CAM survey is lower, the fraction of *Chandra* sources with *ISO*-CAM matches is lower but is still $\approx 25\%$ (see Table 9 and Figure 16). Here we have four *Chandra* source matches with main *ISO*-CAM sources and one *Chandra* source match with a supplementary *ISO*-CAM source. Again we note that a high fraction (3/5) of the *Chandra*/*ISO*-CAM matches are also detected at 8.5 GHz. A few of the *Chandra*/*ISO*-CAM matches outside the HDF-N are remarkable. For example, HDF_PM3_2 (J123634.4+621212; see A99) is associated with a $z = 0.458$ (C00), $R = 19.5$ disk galaxy showing evidence for a double nucleus which may indicate a recent merger. R98 suggest that this galaxy has a star formation rate of $\approx 95\ M_{\odot}\ \mathrm{yr}^{-1}$, about an order of magnitude larger than that of M82. *Chandra* has only detected J123634.4+621212 in the soft-band, consistent with a starburst nature, and its X-ray luminosity in this band of $\approx 8 \times 10^{40}$ erg s^{-1} is also about an order of magnitude larger than that of M82. HDF_PM3_6 (J123636.5+621348) is associated with a $z = 0.960$, $R = 21.5$ AGN discussed by Phillips et al. (1997); intervening absorption lines are seen towards this AGN at $z = 0.846$.

Overall, the *Chandra*/*ISO*-CAM matches span a wide range of full-band X-ray luminosity from $\approx 10^{40}$–10^{43} erg s^{-1}. AGN comprise the more luminous X-ray sources and starbursts the less luminous ones, as expected. Our *Chandra*/*ISO*-CAM matches also have a range of X-ray band ratios, but as a population they do not obviously stand out from the other X-ray sources.

7.4. Very Red Objects

C00 and Hogg00 have identified and discussed 33 very red objects (VROs), defined as having $\mathcal{R} - K_s > 5.0$ (down to $\mathcal{R} = 25.5$ and $K_s = 20$). These were found in a region slightly smaller than the Caltech area (see Figure 2 of Hogg00), due to the fact that their K_s coverage did not encompass the entire Caltech area. The nature of most of these VROs is uncertain due to the difficulty of spectroscopic follow up as most have $\mathcal{R} > 23.5$. The majority of VROs have been proposed to be old galaxies at $z \sim 1$, in which case they can sometimes point to high-redshift clusters (e.g., Stanford et al. 1997; Hasinger et al. 1998; Cimatti et al. 1999; and references therein). Some, however, may be distant AGN and starbursts that are shrouded in dust (e.g., Newsam et al. 1997; Richards et al. 1999; H00; Lehmann et al. 2000; and references therein). Sensitive X-ray observations of VROs, particularly in the hard-band, are a powerful way to assess their AGN content.

7.4.1. Individual Chandra Detections of VROs

We detect four of the 33 VROs in X-rays (see Table 10). The small *Chandra* detection fraction suggests a relatively small AGN content in the optically selected VRO population, although AGN suffering from heavy obscuration ($N_{\rm H} \gtrsim 5 \times 10^{23}$ cm^{-2}) might escape detection in even these data. The four VRO detections are among the hardest *Chandra* sources (see Table 10 and Figure 5); none is formally detected in the soft-band, although J123629.1+621045 has a hint of a soft-band photon excess at its position. The band ratios of the X-ray detected VROs are larger than expected for typical elliptical galaxies at moderate redshift; for $z \approx 1$, the hard-band counts arise from above ≈ 4 keV in the rest frame, whereas typical ellipticals produce the bulk of their X-ray emission below 4 keV.

Only two of the X-ray detected VROs, the Hogg00 sources J123629.1+621045 and J123715.9+621213, are bright enough for optical spectroscopy (see Table 6). Both are classified as having "emission-line" spectra by C00, but these authors did not note any evidence for AGN. Analyses of the Keck/LRIS spectra in Figure 8 show the presence of one significant narrow emission line in each spectrum that we interpret as [O II] 3727 Å; our redshifts are identical to those of C00. There is no evidence for the presence of a [Ne V] line in either spectrum (see §4.2 of Schmidt et al. 1998), but this is not a stringent constraint given the relatively low signal-to-noise of the data. The spectrum of J123715.9+621213 contains a weak feature that may correspond to [Ne III] 3869 Å. J123629.1+621045 is also notable as an 81.4 ± 8.7 μJy source at 1.4 GHz and a probable submillimeter source (R00; see §7.2). The large band ratios of these two VROs, combined with their observed X-ray luminosities, suggest that they are moderately luminous obscured AGN. The same conclusion is also likely to hold for the two X-ray detected VROs without redshift information, although clearly follow-up work is required for these.

While the four X-ray detected VROs are hard, we note that objects are detected in the X-ray with $\mathcal{R} - K_{\rm s} = 4$–5 and a range of X-ray hardness; there are ten such objects in the soft band and eight in the hard band (compare with Newsam et al. 1997). Hogg00 report only one extremely red object in the Caltech area with $\mathcal{R} - K_{\rm s} > 6$ (J123711.1+620933); this object is not detected in our source searching, and manual inspection does not show any hint of a photon excess at its position.

7.4.2. Average X-ray Properties of the X-ray Weak VROs

We have stacked *Chandra* images of the 29 X-ray undetected VROs in the soft and hard bands to place further constraints on their X-ray emission (see Figure 17). Before stacking we have manually verified that none of these 29 sources shows apparent emission just below the detection threshold, and we have also manually verified that flaring pixels (see §3.3) are not corrupting the stacking procedure. The stacked images have effective exposure times of 6.02 Ms, and we have searched these with WAVDETECT using a probability threshold of 1×10^{-7}. A 31.3-count source is detected in the soft-band stacked image; the resulting average soft-band flux of an X-ray weak VRO is $\approx 1.9 \times 10^{-17}$ erg cm^{-2} s^{-1}. At $z \approx 1$ and $z \approx 2$, the corresponding rest-frame soft-band X-ray luminosities are $\approx 6 \times 10^{40}$ erg s^{-1} and $\approx 3 \times 10^{41}$ erg s^{-1}, respectively. No sources are detected in the hard-band stacked image; the 3σ upper limit for the hard band is 16.4 counts, corresponding to an average upper limit on the flux of 5.7×10^{-17} erg cm^{-2} s^{-1}. The band ratio for the average X-ray weak VRO is < 0.52; for a power-law model with the Galactic column density, this corresponds to $\Gamma > 1.4$.

Our detection of the average X-ray weak VRO in the soft band but not the hard band stands in contrast to the results for the 4 individual VRO detections described above; the latter were some of the hardest X-ray sources and were not detected in the soft band. The band-ratio upper limit for the average X-ray weak VRO is highly disjoint from the lower limits of the individually detected VROs (see Table 10). There thus appear to be at least two separate classes of VROs in terms of their observed X-ray emission properties. The softer X-ray spectral shapes and likely X-ray luminosities of the X-ray weak VROs are consistent with the emission properties of moderate redshift ($z \sim 1$) ellipticals where the X-rays arise from a hot interstellar medium. The X-ray data therefore provide supportive evidence for an elliptical galaxy interpretation of many of the VROs, as has been argued based on observations at other wavelengths (see §7.4). However, given that the constraints on the X-ray spectral shape of the average X-ray weak VRO are not tight ($\Gamma > 1.4$; see above), it is still possible that at least some of them are obscured moderate-luminosity AGN at fairly high redshift ($z \gtrsim$ 2–3); their apparently softer X-ray spectra would then simply arise as a result of the photoelectric absorption cutoff being moved to lower energies by the redshift. At $z \gtrsim 3$, for example, X-ray emission from AGN having $N_{\rm H} \lesssim 10^{23}$ cm^{-2} would be redshifted into the observed soft band. Such AGN would not appear to be particularly hard sources, especially if there were also a contribution from scattered, unabsorbed flux. If there is a significant population of high-redshift, obscured AGN among the VROs, it is somewhat surprising that the band ratios of the average X-ray weak VRO and the individually detected VROs are so disjoint; we would have perhaps expected to detect a few VROs with intermediate band ratios, but this could simply be due to limited source statistics.

The properties of the three *Chandra*-detected elliptical galaxies in the HDF-N itself can be compared with the X-ray constraints we place on the rest of the VRO population. The three elliptical galaxies in the HDF-N are CXOHDFN J123648.0+621309 ($\mathcal{R} - K_{\rm s} = 3.23$; $z = 0.475$), CXOHDFN J123655.4+621311 ($\mathcal{R} - K_{\rm s} = 4.66$; $z = 0.968$) and CXOHDFN J123656.9+621301 ($\mathcal{R} - K_{\rm s} = 4.41$; $z = 0.474$); they would be very red at $z > 1$. Their X-ray band ratios of < 1.03, $0.26^{+0.22}_{-0.14}$ and $0.59^{+0.22}_{-0.14}$ are much softer than those of the X-ray detected VROs (see Table 10) but consistent with that of the average X-ray weak VRO.

7.5. Optical Active Galaxy Candidates

The *Chandra* sources were cross-correlated with five lists of AGN candidates identified at optical wavelengths (see Table 5), and only three objects were found with matches. These sources are a $z = 2.580$ QSO (CXOHDFN J123622.9+621527; see §A.2 and Liu et al. 1999), the $z =$ 0.96 AGN in the HDF-N itself (CXOHDFN J123646.3+621404; see H00) and a $z = 1.020$ QSO (CXOHDFN J123706.8+621702; see §A.3 and Vanden Berk et al. 2000).

The AGN candidates identified at optical wavelengths are generally optically faint ($R \approx 27$). We have plotted them along with X-ray sources from this paper and others in Figure 8. Most of the candidates with $R \gtrsim 25$ are still found to be consistent with the range of $\log\left(\frac{f_{\rm X}}{f_{\rm R}}\right)$ typical of X-ray detected AGN (Schmidt et al. 1998; Akiyama et al. 2000), so we cannot rule out the presence of AGN in these optically faint candidates.

We can place somewhat stronger constraints statistically by stacking the images of the X-ray undetected AGN candidates in the same manner as for the submillimeter sources and the VROs (see §7.2 and §7.4). The results of stacking the X-ray images of the X-ray undetected AGN candidates are given in Table 11. There were no sources detected in any of the relevant X-ray bands when WAVDETECT was run on the stacked images, so we place upper limits on the average X-ray emission from these sources. The typical flux upper limit is $\approx 2 \times 10^{-17}$ erg cm^{-2} s^{-1} in the soft band and $\approx 1 \times 10^{-16}$ erg cm^{-2} s^{-1} in the hard band. We did not use the stacking technique for the X-ray undetected Vanden Berk et al. (2000) objects as there are only two such sources in the Caltech area, and the stacking technique provides large improvements over the raw limits only when the effective integration time can be increased significantly. For the Jarvis & MacAlpine (1998) sample, all objects are claimed to be at $z > 3.5$ so the resulting average rest-frame X-ray luminosity in the 0.5–8 keV band is $\lesssim 3 \times 10^{44}$ erg s^{-1}. For the Sarajedini et al. (2000) sample, the most distant object has a photometric redshift of $z \approx 1.9$, and the mean redshift is $z \approx 1.1$. The average X-ray luminosity limits in the full-band for these sources are $\lesssim 1 \times 10^{44}$ erg s^{-1} for $z \approx 1.9$ and $\lesssim 3 \times 10^{43}$ erg s^{-1} for $z \approx 1.1$. The Conti et al. (1999) objects are split into high-redshift ($z > 3$) and low-redshift ($z < 3$) classes, so the constraints on these objects can be compared to the Jarvis & MacAlpine (1998) limits in the high-redshift case and to the Sarajedini et al. (2000) limits in the low-redshift case. All of these authors have pointed out that the typical range of absolute magnitudes for these AGN candidates ($M_{\rm V} \approx -18$) are consistent with low-luminosity Seyfert 1 galaxies or Seyfert 2 galaxies rather than with luminous QSOs, so the X-ray limits are still consistent with their findings. Extremely deep ($\gtrsim 1$ Ms) X-ray observations will be necessary to test these AGN search techniques effectively.

The two X-ray undetected Vanden Berk et al. (2000) objects are notable since they are bright in the optical; ultraviolet excess QSO candidate J123628.1+621433 has $R = 21.3$ and high-redshift QSO candidate J123723.7+621544 has $R = 19.3$ (see Vanden Berk et al. 2000 for a discussion of these object classifications). We have placed upper limits on their X-ray emission; the limit is $\approx 2.4 \times 10^{-16}$ erg cm^{-2} s^{-1} in the full band. J123628.1+621433 has a measured redshift of $z = 0.243$ (C00); the corresponding X-ray luminosity upper limit is 3.4×10^{40} erg s^{-1}. According to Vanden Berk et al. (2000), J123723.7+621544 is at $z > 3$; the corresponding X-ray luminosity upper limit at $z = 3$ is 9×10^{42} erg s^{-1}. We find that J123628.1+621433 most likely does not contain a luminous AGN. While J123723.7+621544 may harbor a moderately luminous AGN, it most likely does not contain a luminous quasar even if it is at very high redshift.

Two other notable AGN that have not been detected in the X-ray, the WAT radio source J123725.7+621128 (Muxlow et al. 1999; R00) and the FR I in the HDF-N, J123644.3+621133, are discussed in §7.1.2.

7.6. Clusters and Groups

As described in §3.4, we have not found any highly significant extended X-ray sources in the Caltech area. We are not aware of any firmly established clusters or groups in this area found from observations at other wavelengths.

WAT radio sources, such as J123725.7+621128 (see §7.1.2), are often found in clusters. We have manually inspected the area around J123725.7+621128, and we find no hint of any extended X-ray emission centered near this source. Given the depth of the current observation, we can rule out moderately luminous cluster X-ray emission near J123725.7+621128 to $z \approx 1.5$.

We have also manually searched for any diffuse X-ray emission near the possible $z \approx 0.85$ cluster discussed by Dawson et al. (2001). Again, we see no hint of diffuse X-ray emission from this object in the current data.

Extrapolating the known number counts for clusters (e.g., Rosati et al. 1998), it is not surprising that none has been detected by *Chandra* in the Caltech area; only 0–2 are expected. Similarly, comparing the solid angle and depth of the current survey to those of deep *ROSAT* surveys, it is plausible (although mildly surprising) that no extended X-ray sources have been detected. Scaling from the results of Schmidt et al. (1998), for example, we would have expected ~ 3 extended X-ray sources in the Caltech area.

7.7. Galactic Objects

There are two X-ray detections of M stars in the Caltech area (see Figure 8 for their optical spectra): CXOHDFN J123625.4+621404 and CXOHDFN J123725.7+621648. The TiO absorption features characteristic of an M4 star are apparent in both spectra, and the M star classification is clearly consistent with their X-ray to optical flux ratios, $\log\left(\frac{f_{\rm X}}{f_{\rm R}}\right) \approx -2$ in both cases. Curiously, Hα emission is not detected from either; this emission is generally associated with plages and/or flares on magnetically active stars. We estimate their distances, based on their optical magnitudes, to be ≈ 240 and ≈ 520 pc. The corresponding soft-band X-ray luminosities are $\approx 10^{28}$ erg s^{-1} in both cases. The second star is one of the most distant X-ray detected M stars ever reported. More information on the properties of the *Chandra*-detected stars in our X-ray survey area will be presented in Feigelson et al., in preparation.

Ibata et al. (1999) have put forward five objects that appear to show proper motion in *HST* images of the HDF-N. These objects are very faint ($V \sim 28$) and blue, but their nature is uncertain; they may be old white dwarfs that represent a population comprising much of the missing Galactic dynamical mass. None of these five objects is detected in the source searching described in § 3.3, but, given their potential importance, we have manually inspected their positions to search for any hints of photon excesses. We find none.

8. Conclusions

8.1. Overview

This work represents the most sensitive study to date of the extragalactic X-ray background source population. We reach limiting soft (hard) flux levels of $\approx 1.3 \times 10^{-16}$ erg cm^{-2} s^{-1} ($\approx 6.5 \times 10^{-16}$ erg cm^{-2} s^{-1}) for individual point sources, and $\approx 1.1 \times 10^{-17}$ erg cm^{-2} s^{-1} ($\approx 5.7 \times 10^{-17}$ erg cm^{-2} s^{-1}) for summed classes of objects (e.g., VROs). The sources in this study comprise $> 90\%$ of the 0.5–2 keV X-ray background and $> 80\%$ of the 2–8 keV background (Paper III; after adding the fraction of the background already resolved in wide-field surveys). Further observations of the HDF-N area, which will bring the total exposure time to ≈ 1 Ms, have been approved for the coming year.

For the 39% of sources with redshift measurements, we find redshifts ranging from 0.1–3.5 and 0.5–8 keV luminosities ranging from 10^{40}–10^{45} erg s^{-1}. These spectroscopically identified sources generally have luminosities well below those of quasars; they resemble weak Seyferts (with both Type 1 and Type 2 spectra), starburst galaxies, and elliptical galaxies. As with the μJy radio sources and ultraluminous far-infrared galaxies studied over the past two decades, it is often unclear whether the faintest X-ray sources are powered by accretion onto a massive black hole or by powerful bursts of star formation. We detect some definite members of both classes, but many sources could be either AGN, starbursts or a combination of both. At 0.5–2 keV fluxes below $\approx 3 \times 10^{-16}$ erg cm^{-2} s^{-1}, we find that a significant fraction of the new sources are associated with low-redshift, optically bright ($R \lesssim 21$) galaxies. Optically faint ($R > 26.5$) X-ray sources that might represent a new class of astronomical object (e.g., extremely high redshift quasars) comprise $< 11\%$ of the current sample and $< 2\%$ of the sources with 0.5–8 keV fluxes $> 7 \times 10^{-16}$ erg cm^{-2} s^{-1}.

8.2. Specific Findings

- Eighty-two X-ray sources have been discovered in the Caltech area down to limiting soft (hard) flux levels of $\approx 1.3 \times 10^{-16}$ erg cm^{-2} s^{-1} ($\approx 6.5 \times 10^{-16}$ erg cm^{-2} s^{-1}). The sources become X-ray harder at low soft-band count rates, consistent with the hardening seen in the *Chandra* Deep Field South survey of G01. The 62 soft-band sources account for $> 90\%$ of the soft X-ray background, and the 45 hard-band sources account for $> 80\%$ of the hard X-ray background (after adding the fraction of the background already resolved in wide-field surveys). See §3.3.

- Redshifts and identification information for 32 of the 82 X-ray sources in the Caltech area are provided, including six redshifts previously unpublished for this region. Included in the sample with redshifts are 96% of the sources with $R < 23$. The median optical magnitude of our sample is $R \approx 23.5$, and 73 of the 82 sources have optical counterparts brighter than $R \approx 26.5$. See §4 and §5.

- At faint soft-band fluxes ($\lesssim 3 \times 10^{-16}$ erg cm^{-2} s^{-1}), we observe the emergence of a population of apparently "normal" galaxies, including moderately star-forming galaxies and elliptical galaxies. This population will only be apparent in *Chandra* surveys with > 100 ks observation lengths. All of these objects are optically bright ($R \lesssim 21$) compared to AGN with the same soft-band X-ray fluxes, and they are found to have low soft-band X-ray luminosities of $\lesssim 3 \times 10^{41}$ erg s^{-1}. See §5.4.

- We have not found any highly convincing Type 2 QSOs thus far. Our best candidate, CXOHDFN J123651.7+621221, has only a moderate observed X-ray luminosity and an uncertain redshift. See §7.1.3.

- Two new X-ray sources in the HDF-N are presented in this paper: CXOHDFN J123639.6+621230 is identified with an $R = 24.3$ broad-line AGN (C00), and CXOHDFN J123644.0+621249 is identified with a star-forming galaxy (R98) which may also contain an AGN. The total number of X-ray sources found in the HDF-N is now eight. See §6.1.

- This study provides the tightest X-ray constraints to date on the μJy radio source population. With *Chandra* we detect 11 of the starburst-type sources, two of the AGN candidates, and three of the unknown-type objects. The high X-ray luminosities ($\gtrsim 5 \times 10^{42}$ erg s^{-1}) and large band ratios of several of the starburst-type systems strongly suggest that they contain previously unrecognized AGN. In general, however, the *Chandra* data are consistent with the idea that the majority of these objects are predominantly powered by star formation. We detect only two of the 17 optically faint μJy sources, consistent with these objects being predominantly powered by starburst activity, although our constraints are difficult to quantify as most of these objects do not have redshifts. See §7.1.

- None of the ten reported submillimeter sources in the Caltech area (Hughes et al. 1998; BCR00) is detected with high significance in our 221.9 ks observation. The tightening of the X-ray constraints relative to H00 does not qualitatively change the basic conclusion reported by H00: these submillimeter sources appear to be dominated by star formation or have Compton-thick nuclear obscuration and little circumnuclear X-ray scattering. See §7.2.

- A remarkable finding is that six of the eight *Chandra* sources in the HDF-N itself have matches with *ISO*-CAM sources. This high matching fraction bodes well for future sensitive infrared observations (e.g., with the *Space Infrared Telescope Facility*) of sources found in deep X-ray surveys. See §7.3.

- In our data, four of the 33 VROs with $\mathcal{R} - K_{\rm s} > 5.0$ are detected in X-rays; they are X-ray hard and moderately luminous ($L_{0.5-8} \gtrsim 10^{42}$ erg s^{-1}). Stacking the *Chandra* images of the 29 X-ray undetected VROs in the soft and hard bands allowed us to place further constraints on their X-ray emission. The stacked images have effective exposure times of 6.02 Ms, and an "average" soft-band source was detected with a soft-band flux of $\approx 1.9 \times 10^{-17}$ erg cm^{-2} s^{-1}. Our detection of the average X-ray weak VRO in the soft band but not in the hard band stands in contrast to our results for the 4 individual VRO detections. There thus appear to be at least two separate classes of VROs in terms of their observed X-ray emission properties. See §7.4.

- Only three of the $\gtrsim 30$ AGN candidates identified at optical wavelengths are detected. In most cases, the X-ray constraints are not tight due to the extreme optical faintness ($R \approx 27$) of these candidates. See §7.5.

- Thus far we have not found any X-ray sources with highly signficant evidence for X-ray spatial extent. We do not detect two objects which might be expected to be associated with clusters of galaxies. See §3.4 and §7.6.

- Two M stars are found in the ACIS image, but none of the possible old white dwarfs discussed by Ibata et al. (1999) are detected. See §7.7.

We gratefully acknowledge the financial support of NASA grant NAS 8-38252 (GPG, PI), NASA GSRP grant NGT5-50247 (AEH), NSF CAREER award AST-9983783 and the Alfred P. Sloan Foundation (WNB), NSF grant AST99-00703 (DPS), and NSF grants AST-0084816 and AST-0084847 (AJB, LLC). AJB acknowledges support through Hubble Fellowship grant HF-01117.01-A awarded by the Space Telescope Science Institute, which is operated by the Association of Universities for Research in Astronomy, Inc., for NASA under contract NAS 5-26555.

We thank D. Alexander, M. Eracleous, G. Hasinger, D. Hogg, C. Liu, T. Miyaji, E. Richards and C. Steidel for helpful discussions and kindly providing data. This work would not have been possible without the enormous efforts of the entire *Chandra* team. We gratefully acknowledge all the creators and operators of the W. M. Keck Observatory. The Hobby-Eberly Telescope (HET) is a joint project of the University of Texas at Austin, the Pennsylvania State University, Stanford University, Ludwig-Maximillians-Universität München, and Georg-August-Universität Göttingen. The HET is named in honor of its principal benefactors, William P. Hobby and Robert E. Eberly. The LRS is named for Mike Marcario of High Lonesome Optics who fabricated several optics for the instrument but died before its completion.

A. Notes on Individual Sources

All X-ray luminosities in this Appendix are quoted for the 0.5–8 keV rest frame of the object unless otherwise indicated. Band ratios and inferred photon indices for all sources can be found in Table 4.

Sources located in the HDF-N itself are discussed in H00 and in §6 of this paper.

The classification system used is described in §5.3.

A.1. Identifications from Optical Spectra in Figure 8

CXOHDFN J123617.0+621010 (z = 0.845, HL Galaxy): Only one clear emission line is present in this optical spectrum; this narrow line is found at 6879.3 Å and is assumed to be [O II]. The Ca II H and K absorption bands are also present, and these match the $z = 0.845$ required for the emission line to be [O II]. We do not detect a [Ne V] emission line, but this object's appreciable X-ray luminosity of 1.2×10^{43} erg s^{-1} strongly suggests that it is an AGN. The X-ray spectrum is not particularly hard. R00 identifies this object in the radio as a radio starburst. Due to the lack of a [Ne V] or [Ne III] feature, we must identify this object as a galaxy, but we do note that the signal-to-noise in the spectrum is not of sufficient quality to rule out Ne emission.

CXOHDFN J123618.0+621635 (z = 0.679, NL AGN): The two [O III] emission lines are seen clearly, placing this object at $z = 0.679$. There is a weak feature at 5755.7 Å which we identify as [Ne V] in emission. The presence of this higher ionization optical emission line and the X-ray luminosity of 2.5×10^{43} erg s^{-1} indicate that this object is a narrow-line AGN. This source is also detected at 1.4 GHz by R00.

CXOHDFN J123618.5+621115 (z = 1.022, BL AGN): The spectrum of this object has a broad line located at $\approx$ 5668 Å. The line is assumed to be Mg II; the corresponding FWHM velocity is $\approx$ 4200 km s^{-1}. A faint feature at 7539.2 Å is identified as [O II], placing this object at $z = 1.022$. It is identified as a broad-line AGN.

CXOHDFN 123625.4+621404 (Star): This object is an M star of type M4–M5. Strong TiO absorption bands dominate the optical spectrum. This source is also one of only two X-ray/2MASS detections in the Caltech area.

CXOHDFN J123629.0+621046 (z = 1.103, NL AGN): This object was identified by Hogg00 as a VRO (see §7.4). This spectrum shows an [O II] emission line and the Ca II H and K absorption features. A weak feature at 7782.2 Å is interpreted as [Ne III] emission. The redshift of this source is $z = 1.103$ (in agreement with the value published by C00); the X-ray luminosity in the 2–8 keV band is 5.0×10^{42} erg s^{-1}. This X-ray source is quite hard, with a band ratio of 1.26 ± 0.31. The corresponding absorption column at $z = 0$ for a $\Gamma = 2$ power law would be $> 10^{22}$ cm^{-2}. The absence of broad lines, the [Ne III] emission feature, the hard X-ray spectrum, and the moderate

X-ray luminosity lead to the classification of this object as an absorbed, narrow-line AGN.

CXOHDFN J123629.2+621613 (z = 0.848, NL AGN): This spectrum shows an [O II] emission line but few other features. The Ca H absorption band appears near 7340 Å, but Ca K overlaps with the atmospheric B band at this object's redshift of 0.848. There may be a [Ne V] feature at 6181.5 Å, but since the stronger [Ne V] line at 3425 Å is absent, this feature may not be real. This X-ray source is quite hard, with a band ratio $> 2.08 \pm 0.47$; it has a hard-band luminosity of 4.4×10^{42} erg s^{-1} and is undetected in the soft-band. The upper limit on the soft-band luminosity is 4.1×10^{41} erg s^{-1}, and the lack of strong AGN features in the optical spectrum prevents us from ruling out star formation as a strong contributor to this object's emission. We conclude, however, that the bulk of the emission in the X-ray band is from an absorbed AGN due to the large amount of hard X-ray emission from this source.

CXOHDFN J123633.4+621418 (z = 3.408, BL AGN): This spectrum shows broad C IV and Lyα emission lines and the characteristic continuum dip on the blue side of the Lyα line produced by the Lyα forest. The measured redshift matches that of C00 ($z = 3.408$). The identification is a broad-line AGN.

CXOHDFN J123636.7+621156 ($z = 0.556$, NL AGN): This spectrum has an [O II] emission line at 5798.9 Å and an Hβ line at 7564.6 Å. The redshift of 0.556 agrees with the value found by Barger et al. (1999) and C00. The Hβ line is moderately broadened (FWHM $\approx$ 1100 km s^{-1}). Absorption features of Ca II H and K and CH (rest frame 4280–4300 Å) are present. This object's X-ray spectrum is fairly soft, and it has an X-ray luminosity of 2.1×10^{42} erg s^{-1}. This object is not detected at either 8.5 GHz or 1.4 GHz. The lack of evidence for X-ray absorption, despite the moderate X-ray luminosity, indicates that star formation may be a significant contributor to this object's emission, but the width of the Hβ line indicates a contribution from an AGN. We classify this object as a narrow-line AGN.

CXOHDFN J123644.0+621249 ($z = 0.555$, NL AGN): This object is in the HDF-N and is discussed in §6.1. It has a somewhat broadened Hβ line and weak [Ne III] emission, so we classify it as a narrow-line AGN.

CXOHDFN J123655.4+621311 ($z = 0.968$, HL Galaxy): This source is an elliptical galaxy in the HDF-N (see H00 and §6.2 of this paper) the only clearly visible feature in its optical spectrum is an [O II] 3727 Å emission line. Its flat radio spectrum indicates the possible presence of an AGN. The redshift we find ($z = 0.955$) is similar to the $z = 0.968$ value of C00.

CXOHDFN J123658.8+621435 ($z = 0.678$, BL AGN): R98 detect this source at 8.5 GHz (but not at 1.4 GHz; see §7.1.4) and identify it with a face-on spiral galaxy at a redshift of 0.678 (C00). This source has an X-ray luminosity of 1.0×10^{43} erg s^{-1}. The HET spectrum has a fairly low signal-to-noise ratio, but we do detect the Ca II break, [O II] emission, and a broad Mg II emission line. We identify this object as a broad-line AGN.

CXOHDFN J123702.7+621543 (z = 0.514, HL Galaxy): This spectrum shows emission lines from [O III] 5007, 4959, and 4363 Å, [O II] 3727 Å and Hβ. It also shows the Balmer series (Hδ through H12) and Ca II H and K in absorption. The redshift we measure, $z = 0.514$, matches that of C00. The X-ray spectrum of this object is fairly hard ($\Gamma \approx 1.2$), and the X-ray luminosity in the 2–8 keV rest frame band is 1.2×10^{43} erg s^{-1}. The Balmer jump is indicative of a "post-starburst" galaxy (for a discussion of post-starburst galaxies see Fisher et al. 1998 and references therein), dominated by an A star population, while the X-ray properties and the strong emission lines both indicate an AGN is also present. This object thus appears to be a "post-starburst AGN" (e.g., Boroson & Oke 1984; Brotherton et al. 1999; Dewangan et al. 2000). Despite the appreciable X-ray luminosity, no broad lines are seen (the only likely strong broad line in our observational window is Hβ, which is unresolved).

CXOHDFN J123704.6+621652 ($z = 0.377$, NL AGN): The main features in this spectrum are [O II] 3727 Å, [Ne II] 3867.8 Å, and the Ca II K absorption band. There is a weak Hβ line, but the [O III] 5007 Å and [Ne V] lines are not detected. The X-ray luminosity of this object is 1.1×10^{42} erg s^{-1}, and it has a moderately soft X-ray spectrum. The presence of Hβ and lack of [O III] emission lines point toward a soft ionizing continuum but may be inconsistent with the detection of [Ne III]. We deduce that this object is undergoing moderate star formation and possibly harbors a low-luminosity AGN.

CXOHDFN J123706.8+621702 ($z = 1.020$, BL AGN): The spectrum contains a strong broad line at 5641 Å; we identify the feature as Mg II at $z = 1.02$. This broad-line AGN was also identified as a QSO candidate by Vanden Berk et al. (2000).

CXOHDFN J123715.9+621213 ($z = 1.020$, HL Galaxy): There is a single narrow line at 7529 Å that is probably [O II] at $z = 1.020$. This source is not detected in the soft X-ray band. Its hard-band X-ray luminosity is 4.0×10^{42} erg s^{-1}. We suspect this object harbors an AGN and note that the signal-to-noise of the spectrum is too low to preclude the existence of [Ne V] or [Ne III]. We classify it as a galaxy to follow the optical classification system.

CXOHDFN 123725.7+621648 (Star): This object is an M star of type M4–M5. Strong TiO absorption bands dominate the optical spectrum.

A.2. Identifications from the Literature

CXOHDFN J123621.3+621109 ($z = 1.014$, HL Galaxy): This object is identified as having a spectrum that is of "intermediate" type (intermediate between being emission and absorption dominated) by C00. It is fairly red, with $\mathcal{R} - K_s = 4.72$ (Hogg00). This source is only detected in the hard band, with a hard X-ray luminosity of 4.0×10^{42} erg s^{-1}. In the radio, it is matched to an extended ($3.2''$) source at 1.4 GHz but lacks a detection at 8.5 GHz (R98; R00), giving a lower limit on the radio spectral index of $\alpha > 0.86$. Since the hard X-ray luminosity is rather large for a starburst, we suspect this object is an obscured AGN. The upper limit on this object's X-ray luminosity in the soft band is 5.6×10^{41} erg s^{-1}, so it is quite plausible that star formation is making a significant contribution to the X-ray emission. We must classify it as a galaxy since we are do not have access to its optical spectrum and are thus unable to ascertain if it exhibits [Ne V] or [Ne III] emission.

CXOHDFN J123622.9+621527 (z = 2.580, BL AGN): This is a spectroscopically confirmed QSO found by Liu et al. (1999).

CXOHDFN J123634.5+621213 ($z = 0.458$, LL Galaxy): This object is detected by *ISO*-CAM and is identified as a starburst galaxy. We designate it as a low-luminosity X-ray galaxy. See §7.3 for further discussion of its properties.

CXOHDFN J123635.3+621110 ($z = 0.410$, LL Galaxy): This object's spectrum is dominated by absorption according to C00 and appears to be of elliptical/S0 morphology on the Hogg00 $\mathcal{R}$ image. It is detected in the soft band with an X-ray luminosity of 6.3×10^{40} erg s^{-1}. Since the spectrum apparently lacks any strong emission features, this object would not be classified as either a starburst galaxy or an AGN. Its large optical luminosity, $\log(L_{\rm B}) = 44.8$, predicts a much higher X-ray luminosity if this object were dominated by X-ray emission from the hot gas in an elliptical galaxy (Eskridge, Fabbiano, & Kim 1995).

CXOHDFN J123636.6+621347 ($z = 0.960$, BL AGN): This object's spectrum is described in detail by Phillips et al. (1997). The principal emission lines in their spectrum are broad Mg II, narrow [O II], [Ne V], [Ne III], H δ, and H γ. It also shows absorption from a nearby disk galaxy at $z = 0.846$ in Mg II and Fe II. This source is classified as a broad-line AGN by C00 and is discussed in §7.3.

CXOHDFN J123639.6+621230 (z = 3.479, BL AGN): This broad-line AGN (C00) is in the HDF-N (see § 6.1 for discussion).

CXOHDFN J123641.8+621131 (z = 0.089, LL Galaxy): This object is in the HDF-N. The X-ray emission is identified with a "knot" most easily visible in the U band (see H00).

CXOHDFN J123642.2+621545 (z = 0.857, HL Galaxy): This source is one of the radio starbursts (see §7.1). The optical spectrum is classified by C00 as being of "intermediate" type. This source is also detected by *ISO*-CAM (see §7.3).

CXOHDFN J123646.3+621404 (z = 0.962, BL AGN): This source is in the HDF-N (see H00).

CXOHDFN J123648.0+621309 ($z = 0.475$, LL Galaxy): This source is an elliptical galaxy in the HDF-N (see H00).

CXOHDFN J123651.7+621221 ($z \approx 2.7$, NL AGN): This source is a Type 2 QSO candidate in the HDF-N (see H00 and references therein).

CXOHDFN J123652.9+621445 (z = 0.322, LL Galaxy): This source is identified as an AGN by R98 due to the variability of its radio emission on timescales of months. C00 identify it as having an absorption-dominated spectrum. This object is underluminous in the X-ray for an AGN with $\log\left(\frac{f_X}{f_R}\right) = -2.4$, and it is undetected in the hard X-ray band. This object is identified as an LL galaxy.

CXOHDFN J123656.9+621301 ($z = 0.474$, LL Galaxy): This source is an elliptical galaxy in the HDF-N (see H00 and §6.2 of this paper). It most likely contains an AGN.

CXOHDFN J123658.3+620958 ($z = 0.137$, LL Galaxy): This object is detected only in the soft band and is associated with a bright S0 or elliptical galaxy ($R = 18.0$). C00 identify it as an emission-line dominated galaxy. The X-ray luminosity is only 6.3×10^{39} erg s^{-1} in the soft band, extremely faint for an AGN. This source is also one of only two X-ray/2MASS detections in the Caltech area.

CXOHDFN J123702.0+621123 ($z = 0.136$, LL Galaxy): This object is identified by C00 as having a spectrum of "intermediate" type. It has a low X-ray luminosity of 8.6×10^{39} erg s^{-1} in the full band. It is identified as an LL galaxy.

CXOHDFN J123713.7+621424 ($z = 0.475$, HL Galaxy): This object has an intermediate-type spectrum (C00). This source is only detected in the hard band, and it has a hard-band luminosity of 6.8×10^{41} erg s^{-1}.

A.3. Other Interesting Objects

CXOHDFN J123616.0+621107 (z unknown): This object is one of the brightest 2–8 keV sources in this sample with a full-band observed X-ray flux of 1.3×10^{-14} erg cm^{-2} s^{-1}, but its optical counterpart is fairly faint ($R = 25.5$). It is also very hard, anomalously so for its bright X-ray flux (see Figure 5) with a band ratio of $2.14^{+0.63}_{-0.47}$; the corresponding $N_{\rm H}$ at $z = 1$ is $\approx 10^{23}$ cm^{-2} for $\Gamma = 1.7$. Note that the X-ray spectral nature of this source is not well understood; a power law may not be the appropriate continuum shape. We have analyzed the light curve and find no strong evidence for variability. This object is not detected in the radio. We suspect that this object does harbor some type of extreme AGN, but further investigation is required.

CXOHDFN J123635.6+621424 (z unknown): This object is quite red ($\mathcal{R} - K_{\rm s} = 4.74$; Hogg00) and also rather hard (its band ratio is $0.75^{+0.71}_{-0.43}$ corresponding to $\Gamma = 0.75$). We observed this object with the Keck LRIS and detected no prominent emission features. It has a rather steep radio spectrum ($\alpha > 0.87$), and the radio emission extends across $2.8''$ (R98; R00). R98 identify it with a face-on spiral galaxy, and R00 identifies it as a star-forming galaxy. It is also detected by *ISO*-CAM (A99). Given the object's spatial extent, it should be at moderate-to-low redshift; at $z \approx 1$ it would have a hard-band X-ray luminosity of $\approx 4 \times 10^{42}$ erg s^{-1} and soft-band luminosity $\approx 7 \times 10^{41}$ erg s^{-1}. The radio and infrared data point to significant star formation in this object, and the hard X-ray emission indicates the possibility of an obscured AGN.

CXOHDFN J123704.8+620941 (z unknown): This object is the only X-ray source with two possible optical counterparts with $R \approx 24$ (see Figure 6 for an the I-band image). The northern counterpart is not clearly visible on the deep V image but is clearly visible on the I band image, indicating that this object is rather red. Since both of these objects are of comparable brightness and within $\approx 1.0''$ of the X-ray source position, we cannot ascertain with the current data which object is the actual counterpart.

CXOHDFN J123704.8+621601 (z unknown): This object is optically faint for its soft-band X-ray flux of 2.9×10^{-15} erg cm^{-2} s^{-1} and hard-band X-ray flux of 5.8×10^{-15} erg cm^{-2} s^{-1} (it is marked with a box in Figure 8). It is undetected at 1.4 GHz (R00). This object may be a highly absorbed AGN at fairly high redshift ($z > 3$); the unabsorbed emission is redshifted into the 0.5–8 keV band, resulting in the only moderately hard nature of the X-ray emission.

REFERENCES

Alexander, D.M., et al. 2001, ApJ, submitted

Aussel, H., Cesarsky, C.J., Elbaz, D., & Starck, J.L. 1999, A&A, 342, 313 (A99)

Aussel, H. 1999, PhD thesis, Université Denis Diderot (Paris VII)

Barger, A.J., Cowie, L.L., Trentham, N., Fulton, E., Hu, E., Songaila, A., & Hall, D., 1999, AJ, 117, 102

Barger, A.J., Cowie, L.L., & Richards, E.A. 2000, AJ, 119, 2092 (BCR00)

Barger, A.J., Cowie, L.L., Mushotzky, R.F., & Richards, E.A. 2001, AJ, in press (B01; astro-ph/0007175)

Bessel, M.S. 1990, PASP, 102, 1181

Boroson, T.A., & Oke, J.B. 1984, ApJ, 281, 535

Borys, C., Chapman, S., Halpern, M., & Scott, D. 2001, in Proceedings of the UMass/INAOE conference on Deep Millimeter Surveys, eds. Lowenthal, J. & Hughes, D., in press (astro-ph/0009143)

Brandt W.N., et al. 2000, AJ, 119, 2349

Broos, P., et al. 2000, User's Guide for the TARA Package: Document Revision 5.8. Penn State University, University Park (available at http://www.astro.psu.edu/xray/docs/)

Brotherton, M.S., et al. 1999, ApJ, 520, L87

Caraveo, P.A., Bignami, G.F., & Trümper, J. 1996, A&AR, 7, 209

Chapman, S.C., Richards, E., Lewis, G., Wilson, G., & Barger, A. 2001, ApJ, submitted (astro-ph/0011066)

Cimatti, A., et al. 1999, A&A, 352, L45

Cohen, J.G., Hogg, D.W., Blandford, R., Cowie, L.L., Hu, E., Songaila, A., Shopbell, P., & Richberg, K. 2000, ApJ, 538, 29 (C00)

Coleman, G.D., Wu, C.-C., & Weedman, D.W. 1980, ApJS, 43, 393

Conti, A., Kennefick, J.D., Martini, P., & Osmer, P.S. 1999, AJ, 117, 645

Cutri, R.M., et al. 2000, Explanatory Supplement to the 2MASS Second Incremental Data Release (Pasadena: IPAC Press); available at http://www.ipac.caltech.edu/2mass/

Dawson, S.A., Stern, D., Bunker, A.J., & Dey, A. 2001, AJ, submitted

Dewangan, G.C., Singh, K.P., Mayya, Y.D., & Anupama G.C. 2000, MNRAS, 318, 309

Dickinson, M., et al. 2000, ApJ, 531, 624

Dobrzycki, A., Ebeling, H., Glotfelty, K., Freeman, P., Damiani, F., Elvis, M., & Calderwood, T. 1999, *Chandra* Detect 1.0 User Guide. *Chandra* X-ray Center, Cambridge

Eales, S., Rawlings, S., Law-Green, D., Cotter, G., & Lacy, M. 1997, MNRAS, 291, 593

Ebeling, H. & Wiedenmann, G. 1993, Phys. Rev. E, 47, 704

Ebeling, H., White, D.A., & Rangarajan, F.V.N. 2001, MNRAS, submitted

Epps, H.W., & Miller, J.S. 1998, Proc. SPIE, 3355, 48

Eskridge, P.B., Fabbiano, G., & Kim, D.-W. 1995, ApJS, 97, 141

Ferguson, H.C, Dickinson, M., & Williams, R., 2000, ARA&A, 38, 667

Fernández-Soto, A., Lanzetta, K.M., & Yahil, A. 1999, ApJ, 513, 34 (FLY99)

Fernández-Soto, A., Lanzetta, K. M. Chen, H., Pascarelle, S.M., & Yahata, N. 2001, ApJ, submitted (astro-ph/0007447)

Fisher, D., Fabricant, D., Franx, M., & van Dokkum, P. 1998, ApJ, 498, 195

Freeman, P.E., Kashyap, V., Rosner, R., & Lamb, D.Q. 2001, ApJ, submitted

FTOOLS Group 2000, User's Guide to FTOOLS. NASA/GSFC, Greenbelt

Garrett, M.A., de Bruyn, A.G., Giroletti, M., Baan, W.A., & Schilizzi, R.T. 2000, A&A, 361, L41

Giacconi, R., et al. 2001, ApJ, submitted (astro-ph/0007240) (G01)

Griffiths, R.G., et al. 2000, Science, 290, 1325

Hasinger, G., et al. 1998, A&A, 340, L27

Hill, G.J., Nicklas, H.E., MacQueen, P.J., Tejada, C., Cobos Duenas, F.J., & Mitsch, W. 1998a, Proc. SPIE, 3355, 375

Hill, G.J., Nicklas, H.E., MacQueen, P.J., Mitsch, W., Wellem, W., Altmann, W., Wesley, G.L., & Ray, F.B. 1998b, Proc. SPIE, 3355, 433

Hill, J.E., Lewis, K.T., Foster, R.F., Bautz, M., Brown, S.K., Roming, P.W.A., Hornschemeier, A.E., Burrows, D.N., & Garmire, G.P. 2000, Proc. SPIE, 4012-42, 402

Hogg, D.W., et al. 2000a, ApJS, 127, 1 (Hogg00)

Hogg, D.W., Neugebauer, G., Cohen, J.G., Dickinson, M., Djorgovski, S.G., Matthews, K., & Soifer, B.T. 2000b, AJ, 119, 1519

Hornschemeier, A.E., Brandt, W.N., Garmire, G.P., Schneider, D.P., et al. 2000, ApJ, 541, 49 (H00)

Hughes, D.H., et al. 1998, Nature, 394, 241 (H98)

Ibata, R.A., Richer, H.B., Gilliland, R.L., & Scott, D. 1999, ApJ, 524, L95

Ishisaki, Y. 1997, PhD thesis, University of Tokyo

Jarvis, R.M., & MacAlpine, G.M. 1998, AJ, 116, 2624

Kraft, R.P., Burrows, D.N. & Nousek, J.A. 1991, ApJ, 374, 344

Lehmann, I., et al. 2000, A&A, 354, 35

Lehmann, I., et al. 2001, A&A, submitted

Liu, C.T., Petry, C.E., Impey, C.D., & Foltz, C.B. 1999, AJ, 118, 1912

Lyons, L. 1991, Data Analysis for Physical Science Students. Cambridge University Press, Cambridge

Maccacaro, T., Gioia, I.M., Wolter, A., Zamorani, G., & Stocke, J.T. 1988, ApJ, 326, 680

McMahon, R.G., & Irwin, M.J. 1992, in Digitised Optical Sky Surveys, ed. MacGillivray, H. T. & Thomson, E. B. (Kluwer, Dordrecht), p. 417

McNamara, B.R., et al. 2000, ApJ, 534, L135

Monet, D., et al. 2000, USNO-A Version 2.0: A Catalog of Astrometric Standards (Flagstaff: USNO Press)

Moran, E.C., Lehnert, M.D., & Helfand, D.J. 1999, ApJ, 526, 649

Mukai, K. 2000, PIMMS Version 3.0 Users' Guide. NASA/GSFC, Greenbelt

Mushotzky, R.F., Cowie, L.L., Barger, A.J., & Arnaud, K.A. 2000, Nature, 404, 459

Muxlow, T.W.B., Wilkinson, P.N., Richards, A.M.S., Kellermann, K.I., Richards, E.A., & Garrett, M.A. 1999, New Astronomy Reviews, 43, 623

Newsam, A.M., McHardy, I.M., Jones, L.R., & Mason, K.O. 1997, MNRAS, 292, 378

Oke, J.B., et al. 1995, PASP, 107, 307

Phillips, A.C., Guzmán, R., Gallego, J., Koo, D.C., Lowenthal, J.D., Vogt, N.P., Faber, S.M., & Illingworth, G.D. 1997, ApJ, 489, 543

Prigozhin, G., Kissel, S., Bautz, M. W., Grant, C., LaMarr, B., Foster, R., Ricker, G., & Garmire, G.P. 2000, Proc. SPIE, 4012, 720

Ramsey, L.W., et al. 1998, Proc. SPIE, 3352, 34

Richards, E.A., Kellermann, K.I., Fomalont, E.B., Windhorst, R.A., & Partridge, R.B. 1998, AJ, 116, 1039 (R98)

Richards, E.A. 1999, PhD thesis, University of Virginia (also see PASP, 112, 1001)

Richards, E.A., Fomalont, E.B., Kellerman, K.I., Windhorst, R.A., Partridge, R.B., Cowie, L.L., & Barger, A.J. 1999, ApJ, 526, L73

Richards, E.A. 2000, ApJ, 533, 611 (R00)

Rosati, P., Della Ceca, R., Norman, C., & Giacconi, R. 1998, ApJ, 492, L21

Sambruna, R.M., Eracleous, M., & Mushotzky, R.F. 1999, ApJ, 526, 60

Sarajedini, V.L., Gilliland, R.L., & Phillips, M.M. 2000, AJ, 120, 2825

Schmidt, M., Hasinger, G., Gunn, J., Schneider, D., Burg, R., Giacconi, R., Lehmann, I., MacKenty, J., Trümper, J., & Zamorani, G. 1998, A&A, 329, 495

Schneider, D.P., et al. 2000, PASP, 112, 6

Stark, A.A., Gammie, C.F., Wilson, R.W., Bally, J., Linke, R.A., Heiles, C., & Hurwitz, M. 1992, ApJS, 79, 77

Steidel, C.C., & Hamilton, D. 1993, AJ, 105, 2017

Thompson, R.I., Storrie-Lombardi, L.J., Weymann, R.J., Rieke, M.J., Schneider, G., Stobie, E., & Lytle, D. 1999, AJ, 117, 17

Townsley, L.K., Broos, P.S., Garmire, G.P., & Nousek, J.A. 2000, ApJ, 534, L139

Vanden Berk, D.E., Stoughton, C., Crotts, A.P.S., Tytler, D., & Kirkman, D. 2000, AJ, 119, 2571

Weisskopf, M.C., O'Dell, S.L., & van Speybroeck, L. 1996, Proc. SPIE, 2805, 2

Williams, R.E., et al. 1996, AJ, 112, 1335 (W96)

Wilman, R.J., Fabian, A.C., & Gandhi, P. 2000, MNRAS, 318, L11

Windhorst, R.A., Miley, G.K., Owen, F.N., Kron, R.G., & Koo, D.C. 1985, ApJ, 289, 494

Table 1. Journal of *Chandra* observations

Obs. ID	Obs. Date	Exposure Time (s)[a]	Aim Point α_{2000}	Aim Point δ_{2000}	ACIS-I Corners α_{2000}	ACIS-I Corners δ_{2000}	Roll Angle (°)[b]
580	1999 Nov 13	49543	12 37 13.1	+62 12 42.3	12 37 35.0	+62 24 16	36.4
					12 35 39.8	+62 14 10	
					12 37 05.9	+62 00 37	
					12 39 02.6	+62 10 32	
967	1999 Nov 14	57444	12 37 01.0	+62 12 56.8	12 37 20.6	+62 24 36	38.0
					12 35 27.9	+62 14 16	
					12 36 57.6	+62 00 53	
					12 38 51.4	+62 11 07	
966	1999 Nov 21	57441	12 37 01.1	+62 12 57.2	12 37 19.7	+62 24 33	38.9
					12 35 27.6	+62 13 55	
					12 36 58.8	+62 00 54	
					12 38 51.6	+62 11 19	
957	2000 Feb 23	57450	12 36 36.4	+62 14 43.8	12 36 51.9	+62 28 35	134.3
					12 35 06.2	+62 16 43	
					12 36 47.8	+62 04 36	
					12 38 33.4	+62 16 27	

[a] All observations were continuous. These times have been corrected for lost exposure due to the 0.041 s read-out time per CCD frame and the drifting of the back-end processor (BEP) clock. Note that times in H00 have not had these corrections made.

[b] Roll angle describes the orientation of the *Chandra* instruments on the sky. The angle is between 0–360°, and it increases to the West of North—opposite to the sense of traditional position angle.

Table 2. False detections due to flaring pixels

α_{2000} ($-12^{\rm h}$)		δ_{2000} ($-62°$)		WAVDETECT SB Counts[a]	Flaring Pixel Counts
36	54.5	9	51.3	6.8	6
36	41.6	9	54.8	6.6	5
36	39.5	9	58.0	5.8	5
36	34.6	13	32.6	8.7	8
36	58.2	9	4.0	5.7	5
37	20.6	11	41.6	3.8	4
36	45.1	13	12.2	5.3[b]	3[b]
36	45.1	13	50.6	4.8	5
36	49.8	13	41.1	5.8	4

[a]The number of events detected in the soft-band (SB) X-ray image by CXC's WAVDETECT. Note that this number is background subtracted and has been convolved with a function representing the *Chandra* PSF (see Freeman et al. 2001 for more information).

[b]This source was only detected in the full band. The quoted counts are for the full band.

Table 3. *Chandra* source detections in the Caltech area

Energy Band	Number of Sources[a]	Detected Counts Per Source Maximum	Minimum	Median	Mean	Background Counts pixel^{-1}
0.5–8 keV (Full)	73	866.4	4.4	27.9	78.1	0.053±0.004
0.5–2 keV (Soft)	62	673.6	4.5	17.2	58.4	0.019±0.002
2–8 keV (Hard)	45	187.5	5.5	18.2	39.0	0.033±0.002
5–8 keV (Ultra-Hard)	10	23.3	3.8	13.2	12.4	0.019±0.002

[a]There were 82 independent X-ray sources detected in total.

Table 4. Properties of *Chandra* sources in the Caltech area

#	CXOHDFN Name (J2000)	FB Counts[a]	FB Error	Δ HB[b] (″)	HB Counts[a]	HB Error	Δ SB[b] (″)	SB Counts[a]	SB Error	Exposure Time (ks)[a]	Band Ratio[c]	Γ[d]	Flux (10^{-15} erg cm^{-2} s^{-1}) FB	HB	SB
1	123614.4+621046	19.9	5.4	···	<13.82	···	···	<11.1	···	200.6	···	1.40	1.02	<1.44	<0.25
2	123615.9+621515	33.6	6.8	0.3	20.05	5.2	2.1[e]	8.9	3.3	202.3	$2.30^{+2.28}_{-1.04}$	0.06	3.45	2.81	0.19
3	123616.0+621107	162.5	13.6	0.2	101.94	10.6	0.7	48.6	7.4	201.8	$2.14^{+0.63}_{-0.47}$	0.09	16.48	14.23	1.05
4	123617.0+621011	123.9	11.9	0.2	38.79	7.0	0.2	83.8	9.4	200.7	$0.47^{+0.15}_{-0.12}$	1.58	5.69	3.89	1.87
5	123618.0+621635	400.1	20.9	0.3	123.00	11.8	0.4	282.0	17.2	200.5	$0.45^{+0.07}_{-0.06}$	1.63	17.94	12.24	6.32
6	123618.5+621115	436.2	21.4	0.1	92.15	9.9	0.1	340.9	18.8	203.0	$0.27^{+0.30}_{-0.04}$	1.93	16.27	8.53	7.66
7	123619.1+621441	76.0	9.1	0.2	18.00	4.6	0.2	60.1	7.9	204.5	$0.30^{+0.13}_{-0.10}$	1.88	2.90	1.67	1.34
8	123619.9+621051	<14.3	···	···	<5.15	···	···	5.5	2.5	203.0	<0.96	1.40	<0.72	<0.53	0.12
9	123620.3+621446	<16.4	···	···	<8.57	···	···	4.5	2.2	204.9	<1.95	1.40	<0.82	<0.88	0.10
10	123620.4+621237	<19.3	···	···	<9.39	···	···	7.2	2.8	204.9	<1.33	1.40	<0.96	<0.96	0.16
11	123621.0+621411	12.1	3.9	···	<15.02	···	1.2[e]	7.9	3.0	205.8	<1.92	1.40	0.60	<1.53	0.17
12	123621.3+621109	13.3	4.1	0.5	13.21	4.0	···	<10.2	···	204.0	>1.32	1.40	0.67	1.36	<0.22
13	123622.6+621028	74.2	9.1	0.2	25.56	5.5	0.1	49.5	7.2	203.4	$0.52^{+0.22}_{-0.16}$	1.50	3.52	2.57	1.09
14	123622.9+621527	456.3	21.8	0.1	110.96	10.9	0.1	347.0	13.3	204.9	$0.32^{+0.05}_{-0.04}$	1.84	17.75	10.36	7.69
15	123625.4+621404	61.9	8.3	···	<10.94	···	0.2	56.3	7.7	184.7[g]	$<0.20^{+0.03}_{-0.02}$	Star	1.71	···	1.52
16	123627.5+621026	47.1	7.3	0.1	33.45	6.1	0.4	11.9	3.7	205.1	$2.84^{+2.02}_{-1.06}$	0.05	4.80	4.64	0.25
17	123627.5+621218	<6.2	···	···	<6.24	···	···	5.7	2.5	207.6	<1.1	1.40	<0.31	<0.63	0.12
18	123627.7+621158	14.7	4.1	0.1	12.70	3.7	···	<7.9	···	207.4	>1.62	1.40	0.73	1.28	<0.17
19	123629.0+621046	27.9	5.7	0.1	18.22	4.6	···	<14.6	···	206.2	>1.26	1.40	1.38	1.85	<0.32
20	123629.2+621613	22.4	5.2	0.4	21.65	5.0	···	<10.6	···	205.4	>2.08	1.40	1.12	2.21	<0.23
21	123629.4+621513	55.1	7.9	···	<16.63	···	0.1	40.1	6.5	207.5	<0.42	1.67	2.32	<1.58	0.87
22	123631.2+620957	<19.1	···	···	<7.92	···	···	7.1	2.8	205.4	<1.14	1.40	<0.95	<0.81	0.15
23	123633.4+621418	23.4	5.1	···	<15.76	···	0.2	16.3	4.1	209.1	<0.97	1.40	1.15	<1.58	0.35
24	123633.6+621123	7.8	3.0	···	<8.76	···	0.1	5.7	2.5	208.8	<1.54	1.40	0.38	<0.88	0.12
25	123633.7+621313	11.6	3.6	0.1	11.03	3.5	···	<6.2	···	210.1	>1.78	1.40	0.56	1.10	<0.13
26	123634.5+621213	10.0	3.3	···	<9.07	···	0.2	7.7	2.8	210.1	<1.19	1.40	0.49	<0.9	0.16
27	123635.3+621109	12.5	3.9	···	<13.03	···	0.4	7.4	2.8	208.9	<1.76	1.40	0.61	<1.31	0.16
28	123635.6+621424	37.1	6.4	0.3	18.75	4.6	0.1	17.2	4.2	209.7	$1.09^{+0.71}_{-0.43}$	0.75	2.60	2.16	0.36
29	123636.6+621347	171.7	13.3	0.2	32.55	5.8	0.1	135.3	11.7	210.6	$0.24^{+0.07}_{-0.06}$	1.99	5.96	2.87	2.94
30	123636.7+621156	56.5	7.7	0.3	10.31	3.3	0.1	42.2	6.6	210.5	$0.25^{+0.14}_{-0.10}$	1.99	1.97	0.91	0.92
31	123639.0+621041	10.6	3.6	···	<10.61	···	···	<14.3	···	209.1	···	1.40	0.52	<1.06	<0.31
32	123639.1+620944	36.5	6.3	···	<16.48	···	0.2	28.9	5.5	207.0	<0.57	1.40	1.81	<1.67	0.62
33	123639.6+621230	14.7	4.0	···	<13.58	···	0.2	9.5	3.2	212.0	<1.43	1.40	0.71	<1.34	0.20
34	123640.2+621655	<11.2	···	···	<5.3	···	···	5.0[f]	2.0	154.1[g]	<1.51	1.40	<0.75	<0.72	0.14
35	123640.8+621042	11.6	3.6	···	<16.26	···	···	<13.6	···	209.6	···	1.40	0.57	<1.62	<0.29

Table 4—Continued

#	CXOHDFN Name (J2000)	FB Counts[a]	FB Error	Δ HB[b] (″)	HB Counts[a]	HB Error	Δ SB[b] (″)	SB Counts[a]	SB Error	Exposure Time (ks)[a]	Band Ratio[c]	Γ[d]	Flux (10^{-15} erg cm^{-2} s^{-1}) FB	HB	SB
36	123641.8+621132	12.6	3.7	···	<8.90	···	0.4	5.8	2.5	211.5	<1.54	1.40	0.61	<0.88	0.12
37	123642.2+621711	64.2	8.4	0.3	18.54	4.6	0.2	44.9	6.9	208.1	$0.42^{+0.20}_{-0.14}$	1.68	2.70	1.76	0.97
38	123642.2+621545	34.6	6.2	0.2	14.49	4.0	0.3	16.3	4.1	174.9[g]	$0.90^{+0.63}_{-0.38}$	0.98	2.57	1.90	0.41
39	123644.0+621249	<14.0	···	···	<6.54	···	···	5.7	2.5	213.5	<1.15	1.40	<0.67	<0.64	0.12
40	123646.3+621404	315.0	17.9	0.1	174.37	13.3	0.1	137.8	11.8	213.0	$1.27^{+0.22}_{-0.19}$	0.58	23.71	20.57	2.82
41	123646.6+620857	13.6	4.1	0.1	11.75	3.7	···	<7.0	···	206.4	$1.70^{+0.53}_{-0.53}$	1.40	0.67	1.19	<0.15
42	123648.0+620941	24.8	5.3	···	<11.59	···	0.1	18.2	4.4	181.1[g]	<0.64	1.40	1.4	<1.34	0.45
43	123648.0+621309	16.6	4.2	···	<11.87	···	0.2	11.6	3.5	214.1	>1.03	1.40	0.79	<1.16	0.24
44	123648.3+621456	15.5	4.1	0.3	8.13	3.0	···	<15.5	···	211.8	>0.53	1.40	0.75	0.8	<0.33
45	123651.2+621051	14.7	4.0	0.0	15.14	4.0	···	<5.1	···	212.3	<2.98	0.07	1.43	2.02	<0.10
46	123651.7+621221	34.5	6.0	0.1	23.00	4.9	0.4	8.8	3.0	214.4	$2.62^{+2.21}_{-1.08}$	0.04	3.38	3.06	0.18
47	123651.8+621504	43.9	6.8	0.4	11.22	3.5	0.1	32.3	5.7	185.4[g]	$0.35^{+0.21}_{-0.14}$	1.80	1.93	1.17	0.79
48	123652.9+621444	13.8	3.9	···	<9.89	···	0.2	9.7	3.2	213.0	<1.03	1.40	0.66	<0.97	0.20
49	123655.4+621311	28.4	5.5	0.3	5.50	2.5	0.1	21.4	4.7	214.9	$0.26^{+0.22}_{-0.14}$	1.97	0.98	0.48	0.46
50	123655.8+621200	12.8	3.7	···	<13.73	···	···	<13.4	···	214.6	···	1.40	0.61	<1.34	<0.28
51	123656.9+621301	22.1	4.9	0.4	7.42	2.8	0.3	12.5	3.6	215.1	$0.59^{+0.56}_{-0.31}$	1.39	1.06	0.72	0.26
52	123657.4+621026	4.4	2.2	···	<7.92	···	···	5.3[f]	1.4	186.4[g]	<1.5	1.40	0.24	<0.89	0.13
53	123658.3+620958	<16.5	···	···	<7.92	···	···	6.9	2.6	210.6	<1.15	1.40	<0.81	<0.79	0.15
54	123658.8+621435	149.7	12.3	0.0	53.68	7.4	0.0	96.2	9.9	173.1[g]	$0.56^{+0.15}_{-0.12}$	1.45	8.62	6.43	2.48
55	123659.4+621616	7.6	3.0	···	<7.51	···	0.1	6.6	2.7	196.6[g]	···	1.40	0.39	<0.8	0.15
56	123700.5+621509	30.3	5.7	0.5	10.46	3.3	0.1	18.5	4.4	193.8[g]	$0.57^{+0.41}_{-0.25}$	1.39	1.61	1.13	0.42
57	123702.0+621123	4.4	2.2	···	<9.89	···	···	<10.1	···	214.2	···	1.40	0.21	<0.97	<0.21
58	123702.6+621244	11.7	3.6	···	<6.74	···	0.1	9.7	3.2	215.1	<0.69	1.40	0.56	<0.66	0.20
59	123702.7+621543	412.8	20.5	0.1	169.39	13.2	0.1	239.2	15.6	195.4[g]	$0.71^{+0.11}_{-0.09}$	1.22	23.95	18.86	5.41
60	123702.8+621601	43.5	6.9	1.2[e]	6.12	2.7	0.17	31.9	5.7	212.4	$0.19^{+0.14}_{-0.10}$	2.09	1.42	0.53	0.69
61	123703.5+621447	8.0[f]	2.8	···	<9.55	···	···	<5.2	···	193.6	···	1.40	0.42	<1.03	<0.12
62	123704.6+621652	75.2	9.1	0.2	15.03	4.1	0.2	54.1	7.5	209.4	$0.28^{+0.13}_{-0.10}$	1.92	2.74	1.35	1.18
63	123704.8+621601	179.4	13.6	0.4	61.4[f]	5.4	0.1	137.6	11.8	212.2	$0.45^{+0.14}_{-0.11}$	1.60	7.61	5.78	2.91
64	123705.1+621635	22.2	5.1	···	<13.28	···	0.1	12.0	3.6	210.4	<1.11	1.40	1.08	<1.32	0.25
65	123706.8+621702	866.4	29.8	0.1	187.49	14.0	0.1	673.6	26.2	208.6	$0.28^{+0.06}_{-0.05}$	1.92	31.65	16.92	14.72
66	123708.4+621204	<14.6	···	···	<6.54	···	···	5.8	2.5	214.5	<1.13	1.40	<0.7	<0.64	0.12
67	123711.9+621325	12.6	3.7	···	<15.97	···	···	<8.3	···	203.1	···	1.40	0.64	<1.65	<0.18
68	123713.7+621424	22.0	4.9	0.5	12.11	3.6	···	<13.7	···	215.5	>0.89	1.40	1.05	1.18	<0.28
69	123714.1+620916	60.4	8.1	0.3	19.26	4.6	0.2	39.0	6.3	207.8	$0.50^{+0.24}_{-0.17}$	1.54	2.75	1.88	0.84
70	123714.3+621208	9.2	3.2	···	<7.58	···	0.4	10.6	3.3	128.7[g]	<0.71	1.40	0.73	<1.23	0.37

Table 4—Continued

#	CXOHDFN Name (J2000)	FB Counts[a]	FB Error	Δ HB[b] (″)	HB Counts[a]	HB Error	Δ SB[b] (″)	SB Counts[a]	SB Error	Exposure Time (ks)[a]	Band Ratio[c]	Γ[d]	Flux (10^{-15} erg cm^{-2} s^{-1}) FB	HB	SB
71	123714.8+621617	47.9	7.2	0.4	14.51	4.0	0.1	31.0	5.7	210.2	$0.47^{+0.26}_{-0.18}$	1.59	2.10	1.39	0.66
72	123715.9+621213	11.0	3.5	0.0	11.33	3.5	···	<5.0	···	176.0[g]	>2.27	1.40	0.64	1.35	<0.13
73	123716.7+621733	382.3	20.1	0.2	159.44	13.0	0.2	213.0	14.8	205.6	$0.76^{+0.12}_{-0.11}$	1.15	21.89	17.13	4.57
74	123719.0+621025	12.0	3.7	···	<12.40	···	0.1	7.5	2.8	204.7	<1.66	1.40	0.60	<1.27	0.16
75	123719.9+620955	38.0	6.5	0.6	7.64	3.0	0.3	25.1	5.1	208.6	$0.31^{+0.23}_{-0.15}$	1.87	1.43	0.70	0.55
76	123721.8+621035	8.1	3.0	0.1	5.58	2.5	···	<9.6	···	195.3[g]	>0.59	1.40	0.42	0.60	<0.22
77	123722.7+620934	18.1	4.6	0.4	9.66	3.3	···	<13.7	···	203.1	>0.71	1.40	0.91	1.00	<0.3
78	123723.2+621538	35.6	6.2	···	<18.33	···	0.1	27.4	5.3	210.2	<0.68	1.40	1.74	<1.83	0.58
79	123724.0+621304	33.1	5.9	0.1	19.75	4.6	0.1	12.6	3.6	202.2	$1.57^{+1.14}_{-0.63}$	0.35	2.96	2.59	0.27
80	123724.3+621359	24.8	5.2	0.2	17.19	4.2	···	<9.7	···	197.5[g]	>1.78	1.40	1.29	1.82	<0.22
81	123725.0+620856	34.0	6.2	0.1	18.55	4.6	0.6	17.5	4.4	186.8[h]	$1.07^{+0.70}_{-0.42}$	0.78	2.64	2.39	0.41
82	123725.7+621648	28.5	5.7	···	<12.24	···	0.1	23.7	5.0	206.2	$<0.52^{+0.14}_{-0.09}$	Star	0.70	···	0.57

[a]CTI-corrected source counts and errors (1σ) are usually as computed by WAVDETECT (see §3.3 and Freeman et al. 2000 for details). The bands are full (FB, 0.5–8 keV), hard (HB, 2–8 keV), and soft (SB, 0.5–2 keV). Source exposure times are effective exposure times taken from the appropriate location in the full-band exposure map (see §3.2 for discussion).

[b]Distance between the source detected in the full-band and either the hard-band or the soft-band images. Positions were determined by WAVDETECT.

[c]Defined as the ratio of counts between the hard and soft bands. Errors for this quantity have been calculated following the "numerical method" described in §1.7.3 of Lyons (1991). These band ratios have been corrected for the differential vignetting in the hard and soft bands.

[d]Γ is the photon index of a power-law model (see § 3.3). Entries with values of 1.40 are assumed, since there are too few counts to determine the band ratio and then to estimate Γ. Entries of "Star" are spectroscopically confirmed stars; a $kT = 0.5$ keV thermal bremsstrahlung X-ray spectral model was assumed.

[e]Both CXOHDFN J123615.9+621515 and CXOHDFN J123621.0+621411 have $> 1.0''$ positional offsets between the full-band and soft-band detections. These are not considered to be independent detections due to decreased positional certainty for the combination of low numbers of counts (< 10) and large off-axis angles ($> 5'$). For the first, the source is very hard even if the soft match is incorrect. For the second, $\Gamma = 1.4$ is assumed regardless of the soft match due to the low number of counts. Both sources have faint ($R > 24.5$) optical counterparts and no measured redshifts, so none of the conclusions about their identities is compromised by a false cross-band match. CXOHDFN J123702.8+621601 has a $> 1.0''$ offset between full-band and hard-band detections, but the hard-band source has only 6 counts and the source spectrum is soft regardless of the hard-band match. This source has a very faint optical counterpart ($R \approx 25.4$) and no redshift, so its identity would not be compromised by a false cross-band match.

[f]WAVDETECT photometry failed, this value is from our manual photometry (see § 3.3). According to WAVDETECT, the numbers of "detected" counts for CXOHDFN J123640.2+621655, CXOHDFN J123657.4+621026, CXOHDFN J123703.5+621447 were 3.6, 1.9 and 3.5, respectively. For CXOHDFN J123704.8+621601, WAVDETECT photometry gave 27.8 counts, but our manual photometry found 61.4 counts.

[g]Source located on or near a gap between the CCDs for at least one observation.

[h]Source located at the edge of the ACIS field during observation 957 (see Table 1).

Table 5. Catalogs correlated against the *Chandra* sources

Catalog Description	Catalog Reference	$N_{\rm S}^{\rm a}$	$R_{\rm M}^{\rm b}$	$N_{\rm M}^{\rm c}$	$N_{\rm F}^{\rm d}$
Radio sources					
VLA (8.5 GHz)	R98	48	$0.4^{\rm e}$	10	0.25
VLA (1.4 GHz)	Richards et al. (1999)	17	$1.0^{\rm e}$	2	<0.25
	R00	65	$0.7^{\rm e}$	16	0.25
VLA + MERLIN	Richards (1999)	67	1.3	16	0.25
	Muxlow et al. (1999)				
WSRT (1.4 GHz)	Garrett et al. (2000)	65	3.0	11	0.75
Submillimeter sources					
SCUBA HDF-N	Hughes et al. (1998)	5	4.0	0	0.50
SCUBA HDF-N and environs	BCR00	5	1.1	0	0.25
Infrared sources					
ISO-CAM 6.5 and 15 μm	A99	100	3.5	11	0.25
2MASS	Cutri et al. (2000)	15	2.1	2	<0.25
Hawaii K selected	Barger et al. (1999)	180	1.4	6	0.75
Caltech K selected	Hogg00	487	1.4	31	0.50
Keck NIRC 3.2 μm	Hogg et al. (2000b)	11	1.4	3	<0.25
NICMOS	Thompson et al. (1999)	342	1.0	0	<0.25
Hawaii I selected	Barger et al. (1999)	2367	1.4	55	5
Optical sources					
HST HDF-N	W96	9509	0.9	8	$2.5^{\rm f}$
Caltech R selected	Hogg00	3606	1.0	60	10
APM POSS	McMahon & Irwin (1992)	147	2.0	12	0.75
USNO A-2	Monet et al. (2000)	45	1.4	5	0.25
Redshift surveys					
Caltech redshift survey	C00	675	1.0	24	2
Stony Brook photometric redshifts	Fernández-Soto et al. (1999)	1067	1.1	7	2
AGN and stellar candidates					
High-z, low-luminosity AGN candidates	Jarvis & MacAlpine (1998)	$32^{\rm g}$	1.4	0	<0.25
Color-selected QSO	Conti et al. (1999)	8	1.0	0	<0.25
Variable galaxies	Sarajedini et al. (2000)	9	1.1	1	<0.25
Wide-field confirmed QSOs	Liu et al. (1999)	1	1.4	1	<0.25
Wide-field QSO and star candidates	Vanden Berk et al. (2000)	$5^{\rm g}$	1.4	2	0.25
Faint, moving objects in HDF-N	Ibata et al. (1999)	5	0.7	0	<0.25

[a]Number of catalog sources in the Caltech area.

[b]Positional error (in arcseconds) of catalog sources adopted for matching with the *Chandra* sources.

[c]Number of catalog sources with *Chandra* source matches.

[d]Statistically expected number of catalog sources with false *Chandra* source matches (see §4.1). Note that this technique is of limited precision in some cases due to small number statistics.

[e]Typical value. Errors differed from source to source as described in the respective reference.

[f]In the HDF-N there are actually zero false matches expected at the optical flux levels of the *Chandra*-W96 matches (see § 4.1).

[g]For Jarvis & MacAlpine (1998), 12 of the 32 objects are AGN candidates. For Vanden Berk et al. (2000), four of the five objects are QSO candidates.

Table 6. Multiwavelength properties of the Caltech area *Chandra* sources

#	CXOHDFN Name (J2000)	R[a]	I[a]	z	z Ref[b]	ID[c]	ID Ref[d]	$\log L_X$ (erg s^{-1})[e] Full	Hard	Soft
1	123614.4+621046[f]	24.8	24.2	···	···	···	···	···	···	···
2	123615.9+621515[f]	25.2	24.4	···	···	···	···	···	···	···
3	123616.0+621107	25.5	24.4	···	···	···	···	···	···	
4	123617.0+621011[g]	22.7	21.7	0.845	H01	HL	H01	43.1	42.9	42.6
5	123618.0+621635[g]	20.5	19.9	0.679	H01	NL AGN	H01	43.4	43.2	42.9
6	123618.5+621115[g]	21.4	21.0	1.022	H01	BL AGN	H01	43.8	43.6	43.5
7	123619.1+621441	24.6	24.3	···	···	···	···	···	···	···
8	123619.9+621051	>26.1	>25.3	···	···	···	···	···	···	···
9	123620.3+621446	>26.1	>25.3	···	···	···	···	···	···	···
10	123620.4+621237[f]	26.2	25.0	···	···	···	···	···	···	···
11	123621.0+621411	24.6	23.7	···	···	···	···	···	···	···
12	123621.3+621109	23.4	21.9	1.014	C00	HL	H01	42.3	42.6	<41.8
13	123622.6+621028	25.1	24.7	···	···	···	···	···	···	···
14	123622.9+621527	20.1	20.0	2.580	Liu	QSO	Liu	44.8	44.6	44.3[h]
15	123625.4+621404	18.1	16.7	···	C00	M4 star	H01	···	···	···
16	123627.5+621026	24.0	22.8	···	···	···	···	···	···	···
17	123627.5+621218	>26.1	>25.3	···	···	···	···	···	···	···
18	123627.7+621158[f]	24.3	23.7	···	···	···	···	···	···	···
19	123629.0+621046[g]	24.0	22.8	1.013	C00	NL AGN	H01	42.6	42.7	<41.9
20	123629.2+621613[g]	21.6	20.4	0.848	H01	NL AGN	H01	42.3	42.6	<41.6
21	123629.4+621513	23.6	23.1	···	···	···	···	···	···	···
22	123631.2+620957	25.3	25.0	···	···	···	···	···	···	···
23	123633.4+621418[g]	24.3	23.8	3.408	C00	BL AGN	C00	43.7	43.6[h]	42.9[h]
24	123633.6+621123	>26.1	>25.3	···	···	···	···	···	···	···
25	123633.7+621313	25.4	24.8	···	···	···	···	···	···	···
26	123634.5+621213	19.5	18.8	0.458	C00	SB/LL	R98	41.4	<41.7	40.9
27	123635.3+621109	21.4	20.7	0.410	B99	LL	···	41.4	<41.7	40.8
28	123635.6+621424	23.5	22.9	···	···	···	···	···	···	···
29	123636.6+621347	21.5	21.1	0.960	C00	BL AGN	C00	43.3	43.0	43.0
30	123636.7+621156[g]	22.3	21.6	0.555	B99	NL AGN	H01/R98	42.3	42.0	41.9
31	123639.0+621041	>26.1	> 25.3	···	···	···	···	···	···	···
32	123639.1+620944[f]	24.0	23.2	···	···	···	···	···	···	···
33	123639.6+621230	24.3	23.5	3.479	FS/C00	BL AGN	C00	43.5	43.4[h]	42.7[h]
34	123640.2+621655	23.1	21.6	···	···	···	···	···	···	···
35	123640.8+621042	25.5	25.0	···	···	···	···	···	···	···
36	123641.8+621132[f]	19.9	19.6	0.089	C00	LL	H00	40.0	<40.2	39.3

Table 6—Continued

#	CXOHDFN Name (J2000)	R[a]	I[a]	z	z Ref[b]	ID[c]	ID Ref[d]	log L_X(erg s^{-1})[e] Full	Hard	Soft
37	123642.2+621711	24.3	23.7	···	···	···	···	···	···	···
38	123642.2+621545	22.2	21.2	0.857	C00	HL	···	42.6	42.5	41.8
39	123644.0+621249[g]	21.3	20.8	0.56	C00	NL AGN/LL	H01	<41.7	<41.7	41.0
40	123646.3+621404	22.1	21.0	0.962	C00	BL AGN	C00	43.6	43.5	42.6
41	123646.6+620857	24.4	23.0	···	···	···	···	···	···	···
42	123648.0+620941[f]	24.6	23.3	Northern object		···	···	···	···	···
		23.5	23.5	Southern object		···	···	···	···	···
43	123648.0+621309	21.0	20.1	0.475	C00	Elliptical/LL	H00	41.6	<41.8	41.1
44	123648.3+621456	>26.1	> 25.3	···	···	···	···	···	···	···
45	123651.2+621051	24.7	23.3	···	···	···	···	···	···	···
46	123651.7+621221	26.7[i]	> 25.3	2.700	D	QSO 2 cand.	H00	43.2	43.2	41.8[h]
47	123651.8+621504[f]	24.9	24.7	···	···	···	···	···	···	···
48	123652.9+621444	19.5	18.7	0.322	C00	LL	R98	41.2	<41.4	40.7
49	123655.4+621311[g]	23.3	21.7	0.968	C00	Elliptical/HL	H00	42.5	42.3	42.2
50	123655.8+621200	24.6	23.8	···	···	···	···	···	···	···
51	123656.9+621301	23.4	22.5	0.474	C00	Elliptical/LL	C00	41.8	41.6	41.1
52	123657.4+621026	23.5	22.3	···	···	···	···	···	···	···
53	123658.3+620958	18.0	17.4	0.137	C00	LL	H01	<40.5	<40.5	39.8
54	123658.8+621435[g]	21.4	20.4	0.678	C00	BL AGN	R98	43.0	42.9	42.5
55	123659.4+621616	>26.1	> 25.3	···	···	···	···	···	···	···
56	123700.5+621509	24.8	24.4	···	···	···	···	···	···	···
57	123702.0+621123	19.3	18.7	0.136	C00	LL	C00	39.9	<40.6	<39.9
58	123702.6+621244	24.8	24.5	···	···	···	···	···	···	···
59	123702.7+621543[g]	19.9	19.2	0.514	C00	post-SB/HL	H01	43.2	43.1	42.5
60	123702.8+621601	25.1	24.5	···	···	···	···	···	···	···
61	123703.5+621447	>26.1	> 25.3	···	···	···	···	···	···	···
62	123704.6+621652[g]	20.5	20.1	0.377	C00	NL AGN	H01	42.0	41.7	41.7
63	123704.8+621601[f]	25.4	25.2	···	···	···	···	···	···	···
64	123705.1+621635	25.4	25.1	···	···	···	···	···	···	···
65	123706.8+621702[g]	19.7	19.6	1.020	H01	BL AGN	H01	44.1	43.9	43.7
66	123708.4+621204	>26.1	>25.3	···	···	···	···	···	···	···
67	123711.9+621325	25.1	24.6	···	···	···	···	···	···	···
68	123713.7+621424	22.0	21.2	0.475	C00	HL	H01	41.8	41.8	<41.2
69	123714.1+620916[f]	24.5	24.0	···	···	···	···	···	···	···
70	123714.3+621208	23.7	23.3	···	···	···	···	···	···	···
71	123714.8+621617	23.7	23.3	···	···	···	···	···	···	···

Table 6—Continued

#	CXOHDFN Name (J2000)	R^{a}	I^{a}	z	z Ref[b]	ID[c]	ID Ref[d]	$\log L_X(\mathrm{erg\ s^{-1}})$[e] Full	Hard	Soft
72	123715.9+621213[g]	23.7	22.3	1.020	C00	HL	C00	42.3	42.6	<41.5
73	123716.7+621733	23.1	22.2	···	···	···	···	···	···	···
74	123719.0+621025	25.6	>25.3	···	···	···	···	···	···	···
75	123719.9+620955	24.3	24.0	···	···	···	···	···	···	···
76	123721.8+621035	22.4	21.3	···	···	···	···	···	···	···
77	123722.7+620934	24.8	24.6	···	···	···	···	···	···	···
78	123723.2+621538	24.0	23.6	···	···	···	···	···	···	···
79	123724.0+621304	24.1	23.6	···	···	···	···	···	···	···
80	123724.3+621359	24.7	24.1	···	···	···	···	···	···	···
81	123725.0+620856	23.4	22.2	···	···	···	···	···	···	···
82	123725.7+621648	19.3	18.0	···	H01	M4 star	···	···	···	···

[a] R and I are measured or calculated as described in §4.2. Lower limits on magnitude are at the 2σ level.

[b] Sources for redshifts. H01: the current paper; Liu: Liu et al. (1999); B99: Barger et al. (1999); FS: Fernández-Soto et al. (1999); D: M. Dickinson 2000, private communication

[c] Abbreviations in the table include: "SB"— Starburst; "LL"—Low-luminosity galaxy (see § 5.4), "HL"—High-luminosity galaxy, "NL"— narrow-line AGN and "BL"— broad-line AGN. The classification system is described in §5.3.2. Individual objects are discussed in detail in §A.1 and A.2.

[d] Sources for identifications are the same as for redshifts (see note "c" above); H00 is Paper I.

[e] Luminosity is for the rest frame of the source.

[f] For these objects, there was an optical counterpart lying within the aperture close to the edge. We have measured the magnitudes with the aperture centered on the position of this optical source (see §4.2 and Figure 6). CXOHDFN J123641.8+621132 is 1.4″ from the galaxy center but is consistent with an apparent off-center ultraviolet bright spot (see H00). It is possible that this spot may be a background AGN. CXOHDFN J123648.0+620941 has two optical counterparts of comparable brightness within the 3.0″ aperture (see Figure 6). We have measured the magnitudes of these two sources manually. See §A.2 for more discussion of this source.

[g] See Figure 9 for this object's spectrum.

[h] High-redshift objects: For soft-band fluxes, the 0.5–2 keV rest frame has been redshifted out of our observed bandpass, so these luminosities are extrapolations of the power law calculated from higher energy data. For hard-band fluxes (2 cases), this object was not detected in the observed 2–8 keV band but since the observed 0.5–2 keV band overlaps well with the rest-frame 2–8 keV band, we use the 0.5–2 keV count rate to calculate the hard luminosity for this source.

[i] CXOHDFN J123651.7+621221 lacks an optical counterpart in our deep I-band imaging, but it does have a faint $V = 26.7$ counterpart in the HDF-N (see H00).

Table 7. Summary of spectroscopic classifications of *Chandra* sources

Object Class	Soft-band Detections	Hard-band Detections	Total Detections
AGN			
Broad-line (BL)	8	6	8
Narrow-line (NL)	5	6	7
Total	13	12	15
Galaxies			
Low-luminosity (LL)	7	1	8
High-luminosity (HL)	4	7	7
Total	11	8	15
Stars	2	0	2

Table 8. Chandra detections of μJy radio sources

VLA object	Δ R-XR[a] ($''$)	$S_{1.4}$ (μJy)	$\alpha_{\rm R}^{\rm b}$	$\theta^{\rm b}$ ($''$)	z	Band Ratio	Class[b]	log $L_{0.5-8}$ (erg s^{-1})
J123646.36+621404.9	0.2	179.0	−0.04	0.2	0.962	1.27	AGN	43.6
J123652.96+621444.3	0.4	168.0	−0.12	2.5	0.322	<1.03	AGN	41.2
J123616.14+621513.9[c]	1.8	53.9	···	1.0	···	2.30	S	···
J123617.10+621011.5	0.5	62.0	···	0.7	0.845	0.47	S	43.1
J123621.27+621109.5	0.2	52.6	>0.86	3.2	1.014	>1.32	S	42.3
J123631.27+620957.3[d]	0.7	152.0	>0.99	2.5	···	<1.14	S	···
J123634.46+621213.3	0.4	233.0	0.74	1.0	0.458	<1.19	S	41.4
J123635.62+621424.3	0.1	87.8	>0.88	2.8	···	1.09	S	···
J123642.23+621545.7	0.3	150.0	0.50	2.4	0.857	0.90	S	42.6
J123651.80+621221.4	0.4	49.3	0.71	0.8	2.7	2.62	S	43.2
J123656.88+621302.5	1.0	49.5	>1.22	1.2	0.474	0.59	S	41.8
J123711.95+621325.8[e]	0.5	53.9	>1.16	1.4	···	···	S	···
J123716.68+621733.5	0.2	346.0	>0.76	0.6	···	0.76	S	···
J123618.04+621635.6	0.6	47.1	···	···	0.679	0.45	U	43.4
J123629.02+621046.0	0.5	81.4	>0.86	···	1.013	>1.26	U	42.6
J123725.05+620856.6	0.1	90.0	···	0.4	···	1.07	U	···

[a]Offset between the radio and *Chandra* source positions.

[b]$\alpha_{\rm R}$ is the radio spectral index and θ is the radio spatial extent; both were determined by R00. R00 classifications are 'S' for 'Starburst-type' and 'U' for 'Unknown'.

[c]Please see footnote "e" in Table 4 and footnote "f" in Table 6 about this object (CXO-HDFN J123615.9+621515).

[d]This source was detected in neither the full nor the hard band.

[e]This source was not detected independently in either the soft or hard bands.

Table 9. *Chandra* detections of faint *ISO*-CAM sources

ISOCAM object	Δ ISO-XR ($''$)	$z^{\rm a}$	7 μm (μJy)	15 μm (μJy)	Band Ratio	$\log L_{0.5-8}$ (erg s^{-1})
J123634.4+621212	1.8	0.456	···	448^{+68}_{-59}	< 1.19	41.4
J123635.6+621424	0.5	···	···	441^{+43}_{-82}	1.09	···
J123636.5+621348	1.4	0.960	···	353^{+40}_{-66}	0.24	43.3
J123642.1+621545	1.4	0.857	···	459^{+46}_{-86}	0.9	42.6
J123644.2+621251[b]	1.7	0.557	< 50	282^{+60}_{-64}	< 1.15	41.0
J123646.4+621406	1.3	0.960	191^{+41}_{-86}	107^{+95}_{-20}	1.27	43.6
J123647.7+621312	3.4	0.475	36^{+65}_{-30}	< 74	< 1.03	41.6
J123651.9+621221	1.2	2.7[c]	< 36	48^{+32}_{-9}	2.62	43.2
J123655.4+621312	0.9	0.968	< 37	23^{+10}_{-11}	0.26	42.5
J123656.7+621303	2.2	0.474	94^{+50}_{-69}	< 54	0.59	41.8
J123702.2+621124	1.4	0.136	···	162^{+76}_{-49}	···	39.9

[a]See Table 6 for individual redshift references.

[b]This source was only detected in the soft band. This luminosity is in the soft band.

[c]This redshift is photometric (M. Dickinson 2000, private communication).

Table 10. *Chandra* detections of VROs

Hogg00 Source	$\mathcal{R} - K_{\rm s}$	$K_{\rm s}$	Band Ratio	$z^{\rm a}$	$\log L_{2-8}$ erg s^{-1}
J123629.1+621045	5.28	17.96	>1.26	1.013	42.7
J123651.2+621051	5.11	19.56	>2.98	···	···
J123715.9+621213	5.05	18.49	>2.27	1.020	42.6
J123724.3+621359	5.24	19.96	>1.78	···	···

[a]From C00; these were determined on the basis of a single emission line assumed to be [O II] 3727 Å.

Table 11. *Chandra* stacking constraints on AGN candidates

AGN Search	Number of Undetected Objects	Stacked Exposure Time (Ms)	3σ Flux Limits (erg cm^{-2} s^{-1}) Soft	Hard
Conti et al. (1999)	8	1.7	1.5×10^{-17}	8.7×10^{-17}
Jarvis & MacAlpine (1998)	12	2.6	1.0×10^{-17}	8.5×10^{-17}
Sarajedini et al. (2000)	8	1.7	1.7×10^{-17}	1.2×10^{-16}

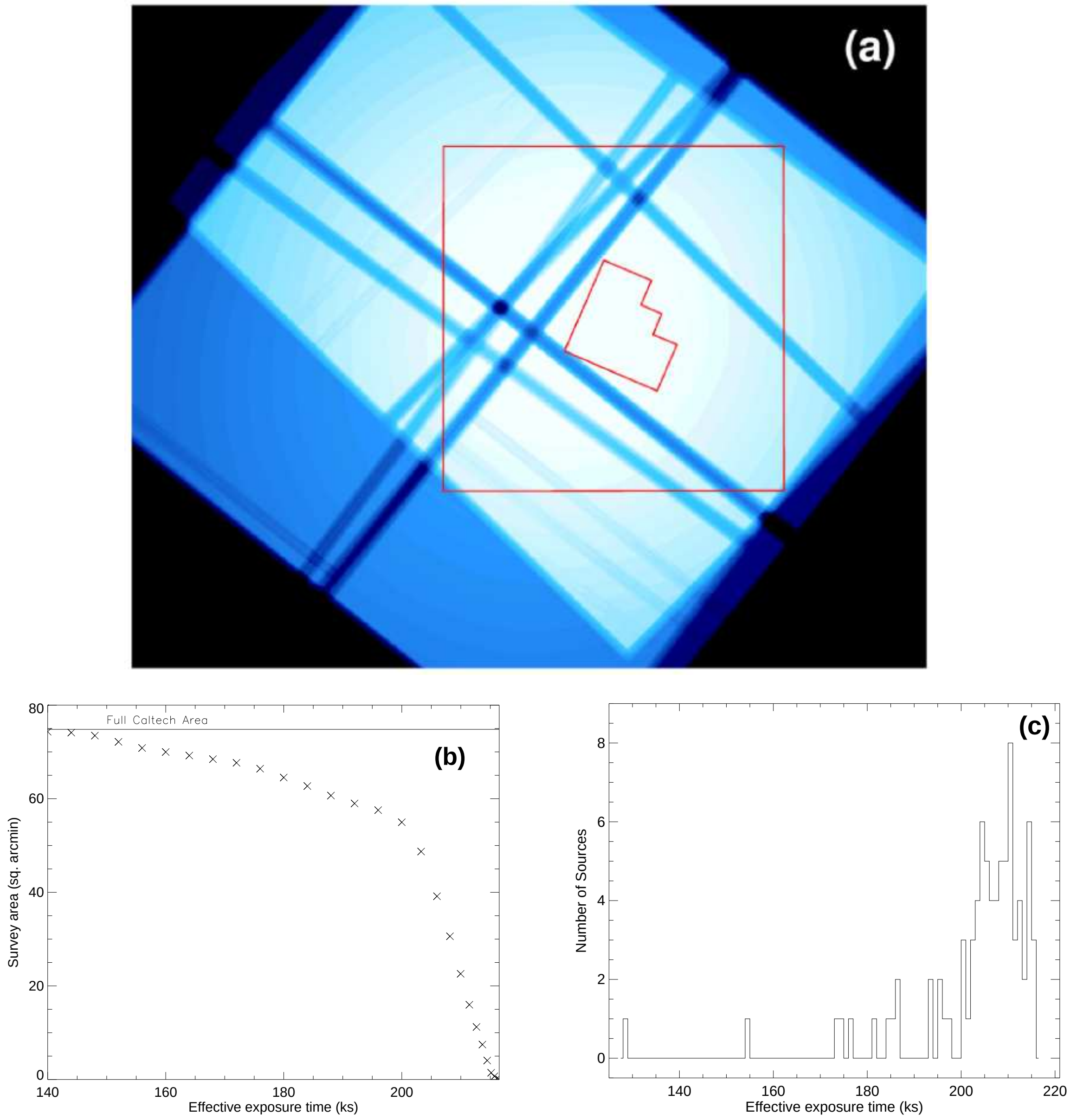

Fig. 1.— (a) The combined exposure map for the four ACIS-I observations. The whitest regions correspond to the highest exposure times. The dark grooves running through the exposure map correspond to the gaps between the ACIS-I CCDs. North is up, and East is to the left. The large square indicates the Caltech area, which is $8.6' \times 8.7'$. The small polygon indicates the HDF-N. (b) The observed survey area for the Caltech area as a function of effective exposure time in that area. Approximately 75% of the Caltech area has an effective exposure time of > 200 ks, which corresponds to the whitest regions in the exposure map. (c) The distribution of effective exposure times for the 82 X-ray sources detected in the Caltech area.

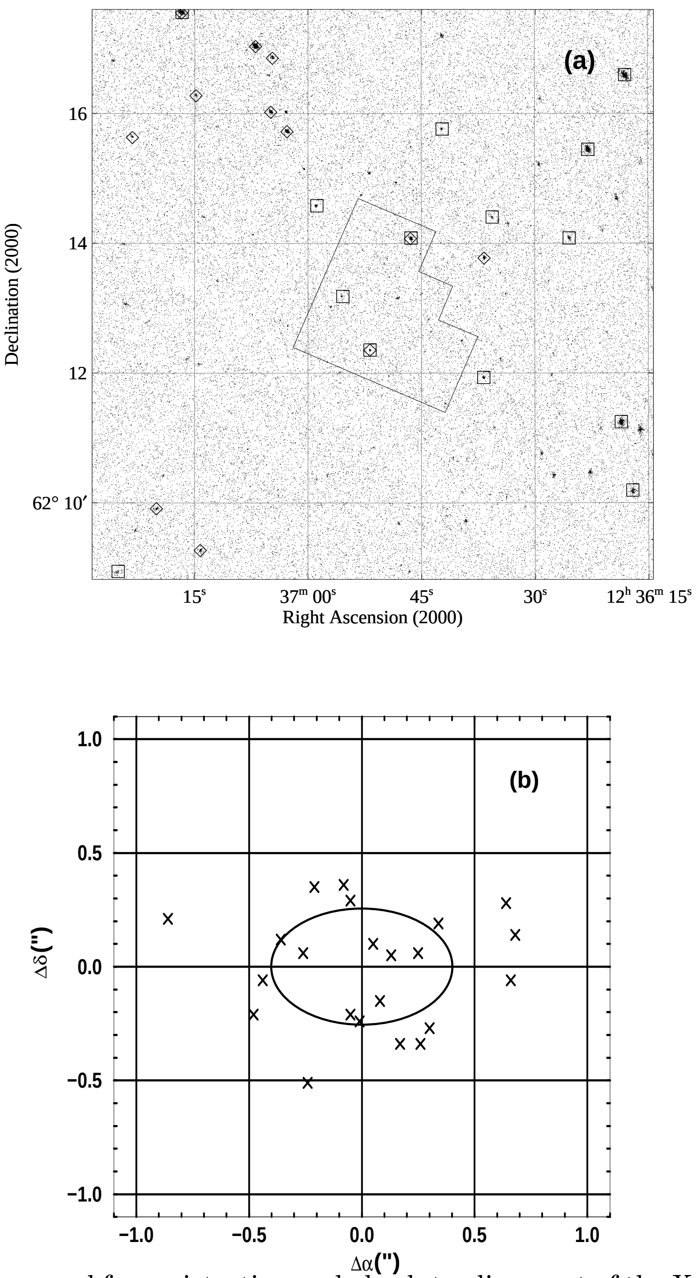

Fig. 2.— (a) The sources used for registration and absolute alignment of the X-ray images are shown in this 0.5–8 keV image. The gaps between CCDs appear less sharp in this image than in Figure 1 as the overall background level is very low and the image scaling is logarithmic. The diamonds indicate bright sources present in all four *Chandra* observations used to register the images. The squares indicate X-ray sources with reliable optical matches in Hogg00 or radio matches in R00 which were used for absolute alignment of the image. A total of 22 sources were used for absolute alignment of the HDF-N observation; 14 are in the Caltech area. (b) Positional dispersion of the 22 *Chandra* sources used for absolute alignment with respect to Hogg00 and R00 coordinates; the ellipse shows the RMS dispersion of the offsets.

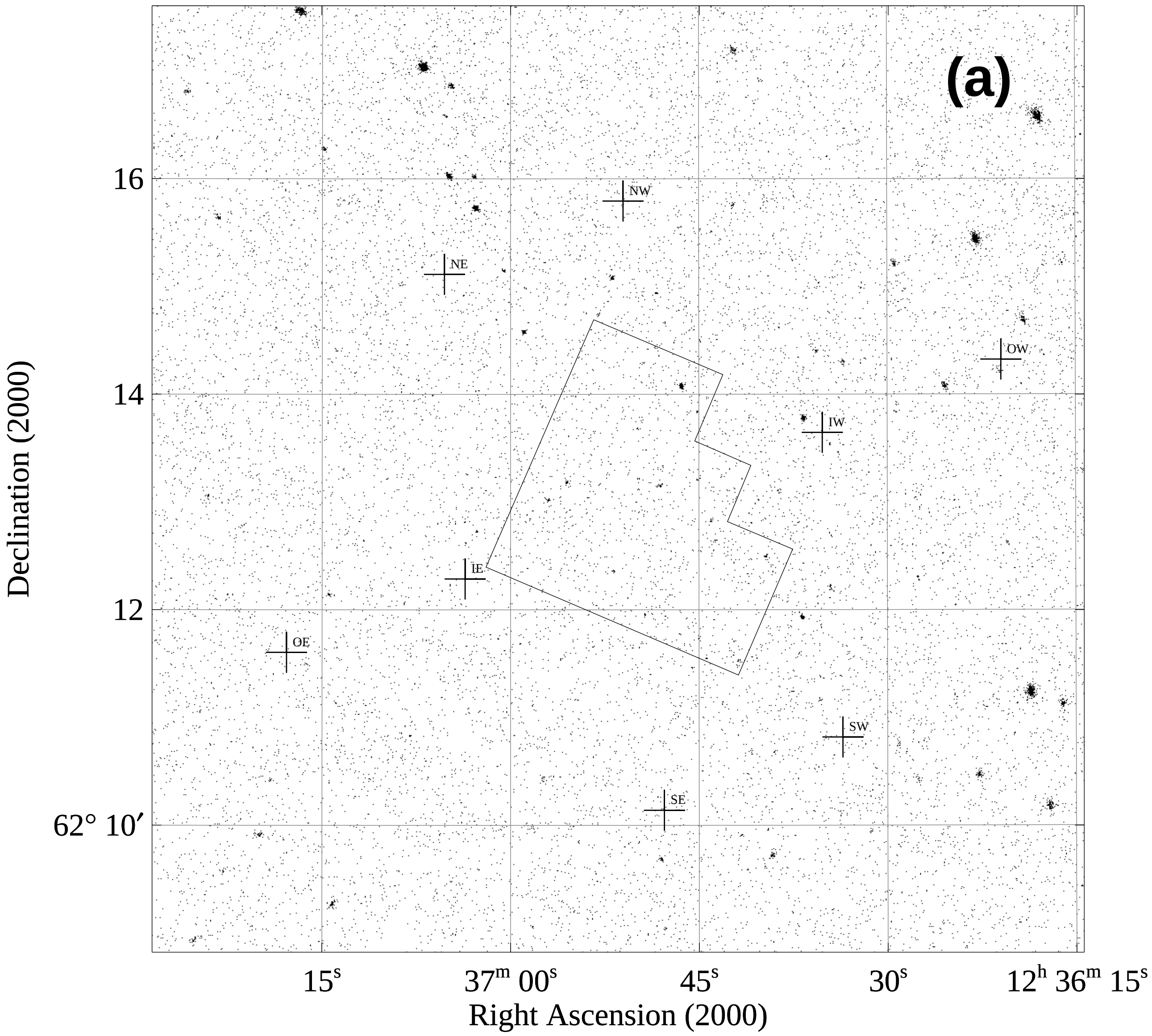

Fig. 3.— The raw X-ray images in the (a) 0.5–2 keV (soft) band and (b) 2–8 keV (hard) band. The area shown matches the Caltech area indicated on the exposure map in Figure 1. The outlined region is the HDF-N, and the crosses mark the centers of each of the Hubble Flanking Fields (see Table 2 of W96).

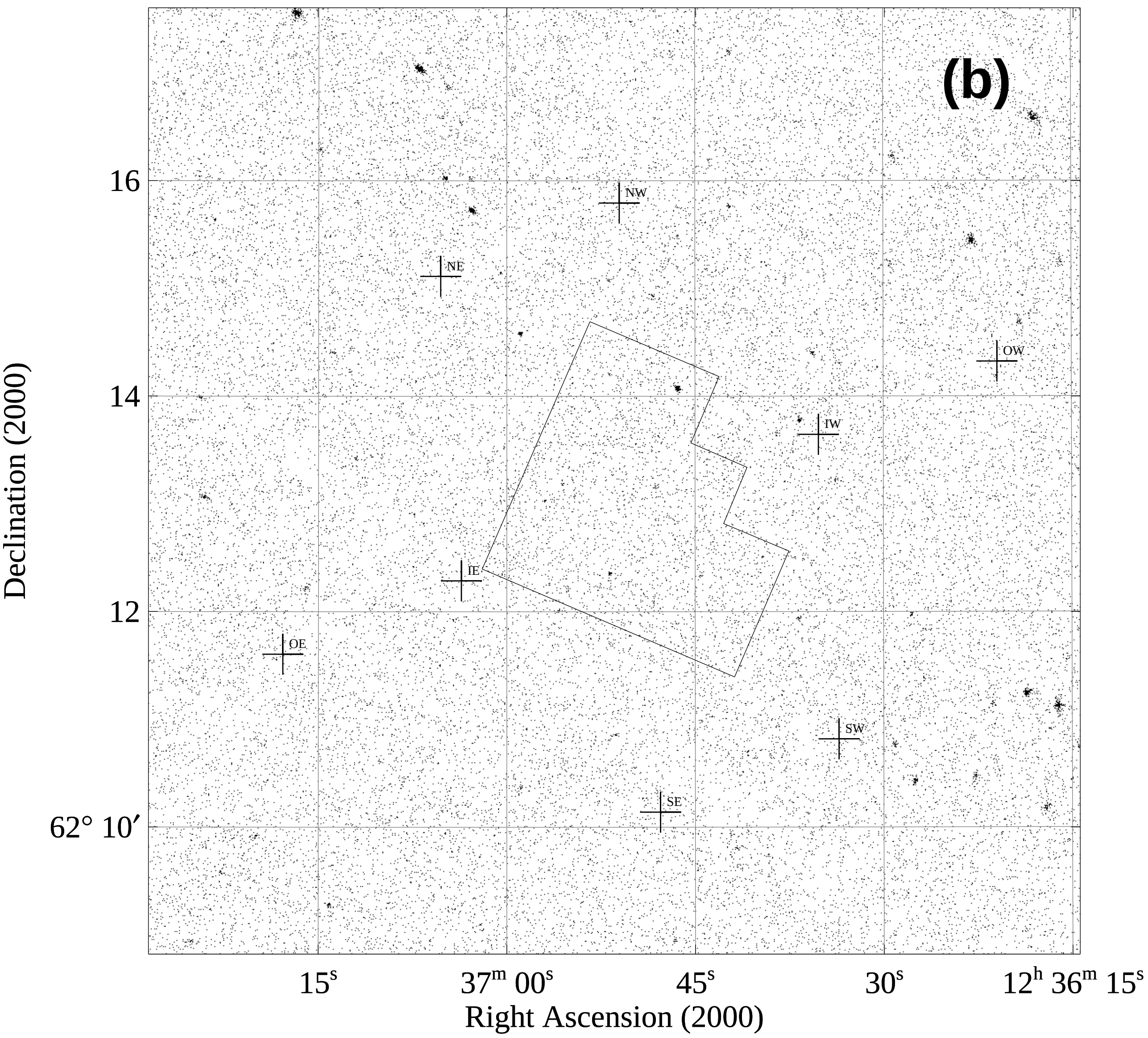
(b)
NW
NE
OW
IW
IE
OE
SW
SE
16
14
12
62° 10′
Declination (2000)
15s
37m 00s
45s
30s
12h 36m 15s
Right Ascension (2000)

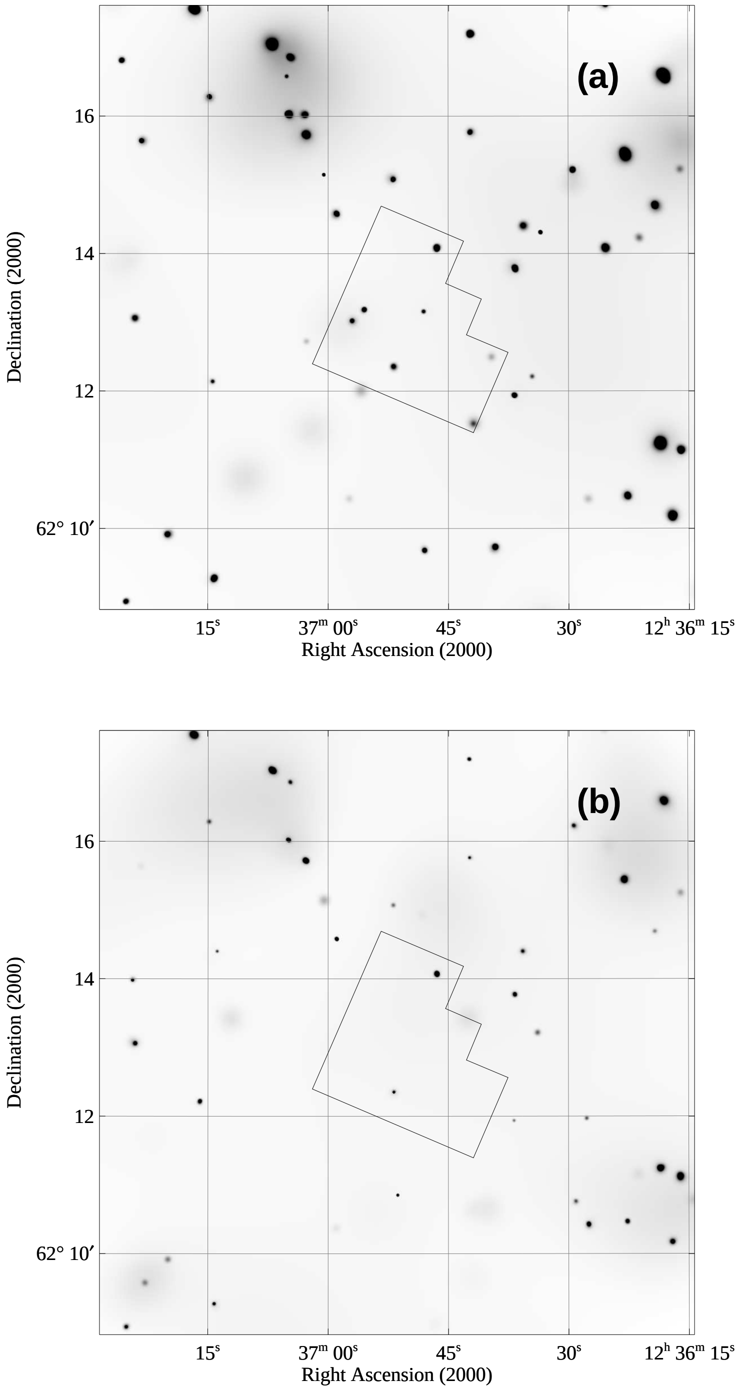

Fig. 4.— Adaptively smoothed versions of (a) the soft-band image shown in Figure 3a and (b) the hard-band image shown in Figure 3b. The adaptive smoothing is at the 3σ level using the code of Ebeling, White, & Rangarajan (2001).

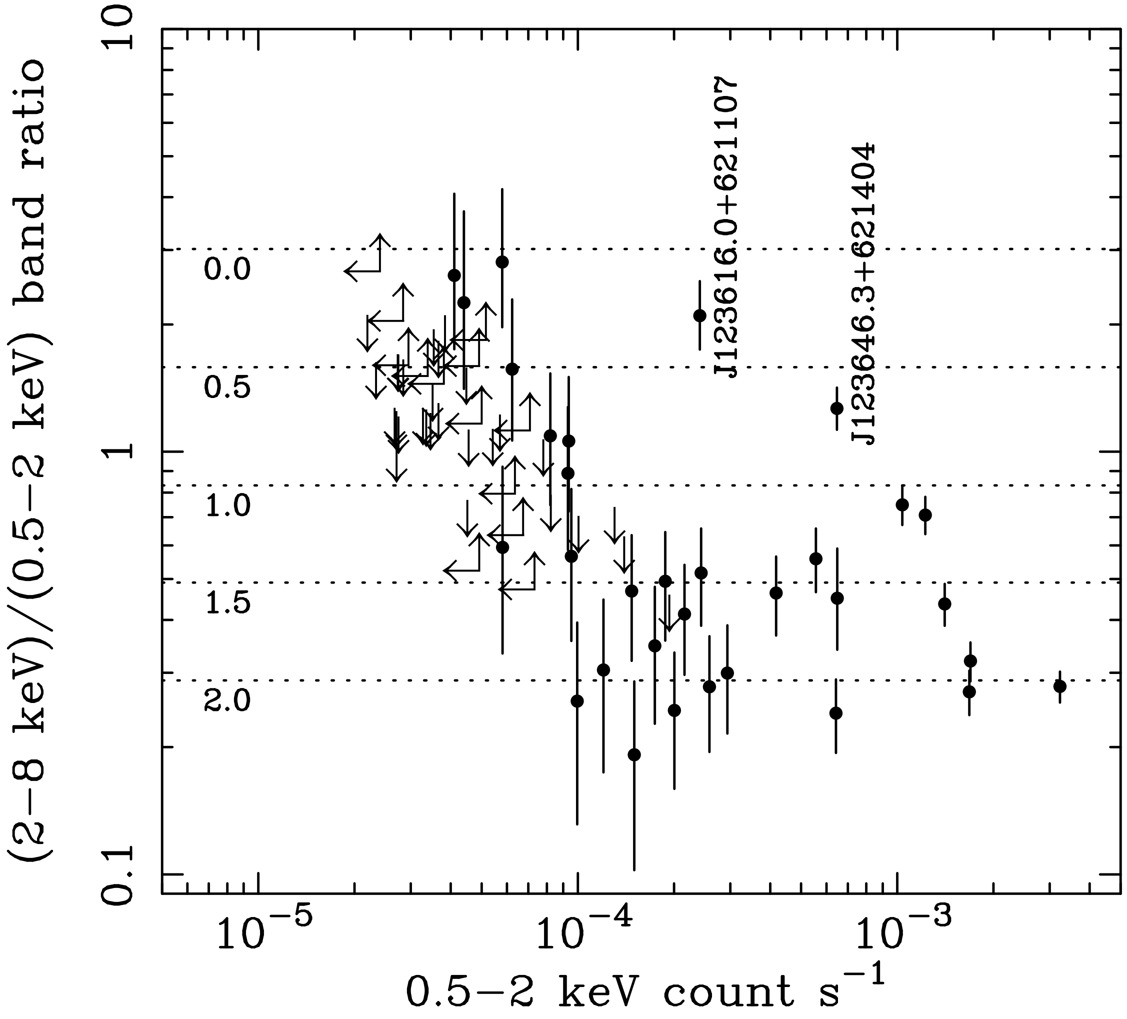

Fig. 5.— Band ratio as a function of soft-band (0.5–2 keV) count rate for the *Chandra* sources in the Caltech area. Dotted lines are labeled with the photon indices which correspond to a given band ratio. Sources only detected in one of the two bands are shown as limits (see Table 4). Note the general hardening of sources with low soft-band count rates (compare with Figure 2 of G00). We have marked two sources that are unusually hard for their soft-band count rates: CXOHDFN J123616.0+621107 and CXOHDFN J123646.3+621404. The first is also remarkable for its large f_X/f_R ratio; its optical counterpart has $R = 25.9$. The second is the $z = 0.960$ AGN in the HDF-N itself (see H00).

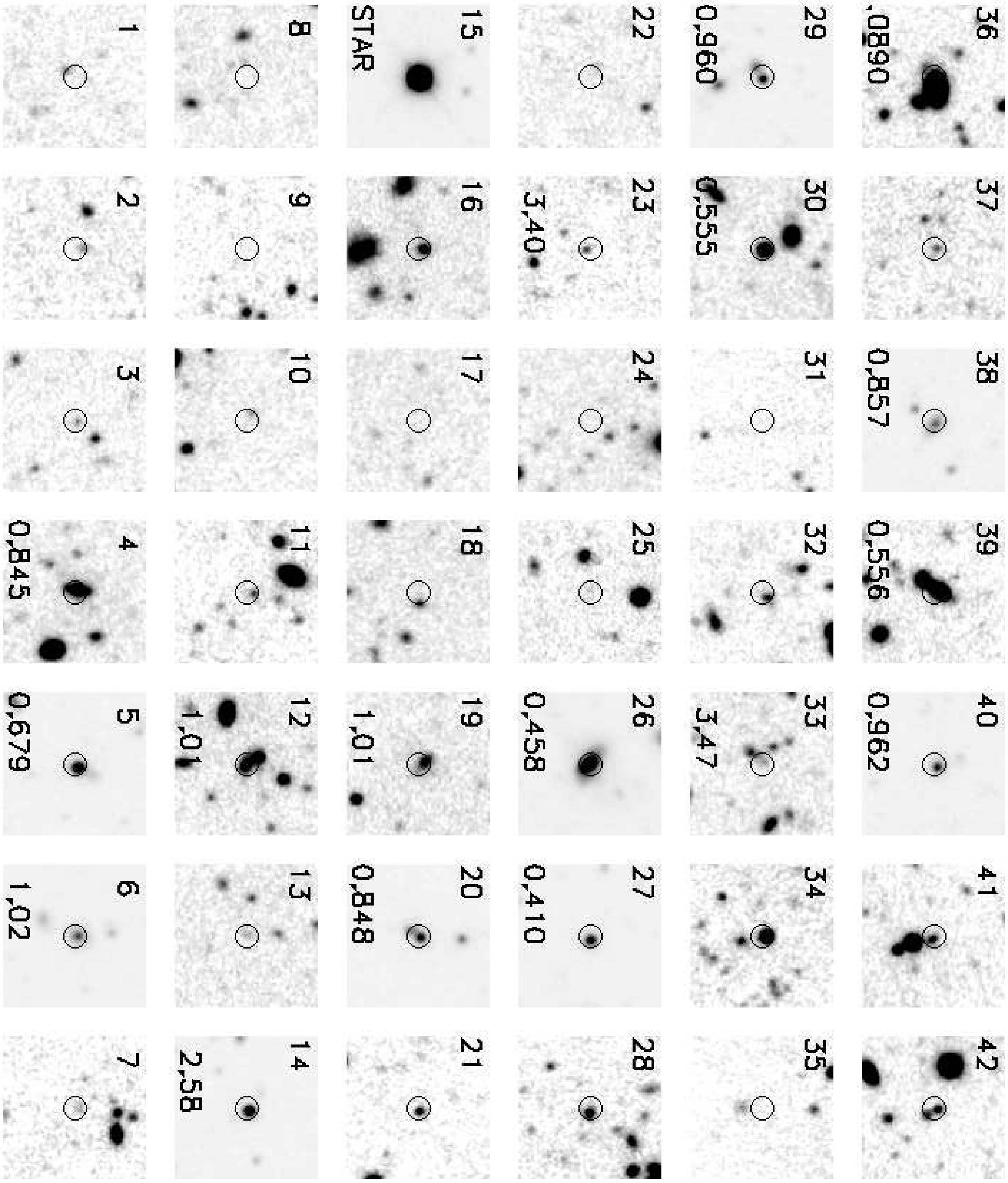

Fig. 6.— Deep I-band "thumbnail" images for the 82 *Chandra* sources. Each image is $19'' \times 19''$, and the circles have $3.0''$ diameters. The images are numbered as in Tables 4 and 6. Objects have been labeled with their spectroscopic redshifts where applicable.

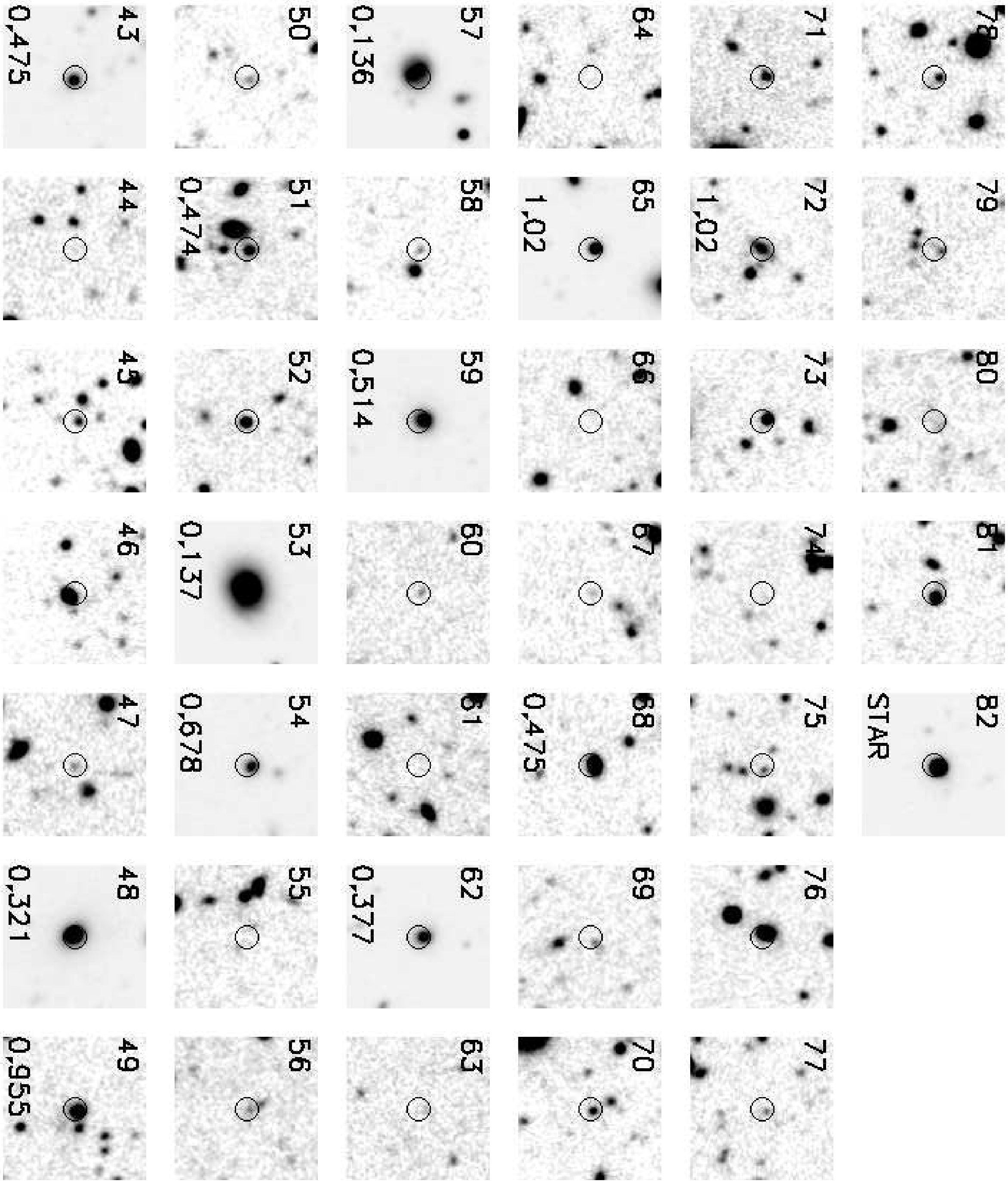
43
0,475
44
45
46
47
48
0,321
49
0,955
50
51
0,474
52
53
0,137
54
0,678
55
56
57
0,136
58
59
0,514
60
61
62
0,377
63
64
65
1,02
66
67
68
0,475
69
70
71
72
1,02
73
74
75
76
77
78
79
80
81
82
STAR

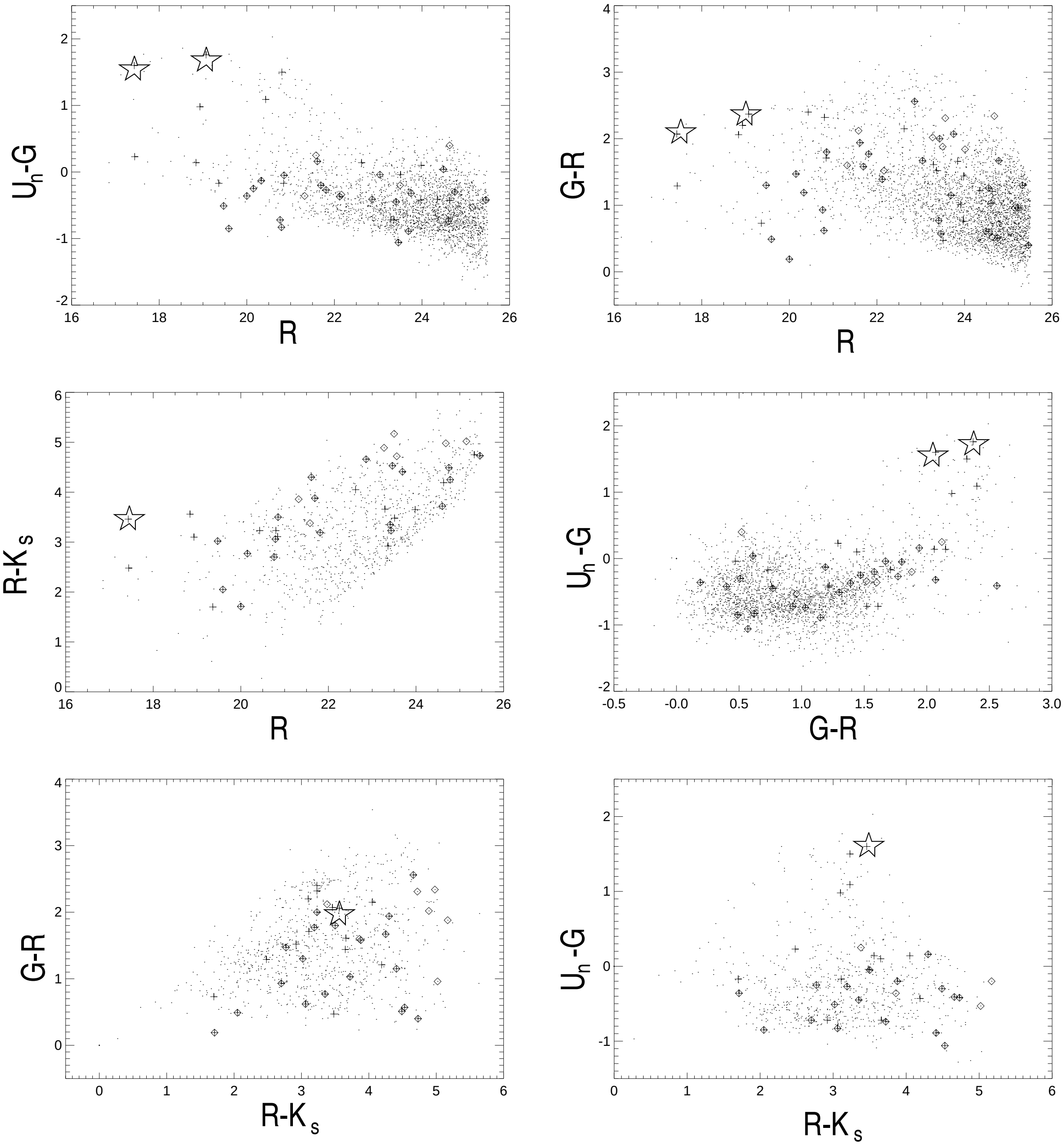

Fig. 7.— Optical colors of the *Chandra* sources as reported by Hogg00. All magnitudes in these plots are in the $U_{\rm n}$, G, $\mathcal{R}$ and $K_{\rm s}$ filters as described in Hogg00 and §4.2. Dots show the entire Hogg00 catalog, diamonds are hard-band detections, and plus symbols are soft-band detections. The star symbols mark the two X-ray detected M stars. All colors available in the Hogg00 catalog are plotted in this figure to show all the possible permutations. Note that not all X-ray sources in the current sample have measured colors and/or magnitudes in the Hogg00 catalog.

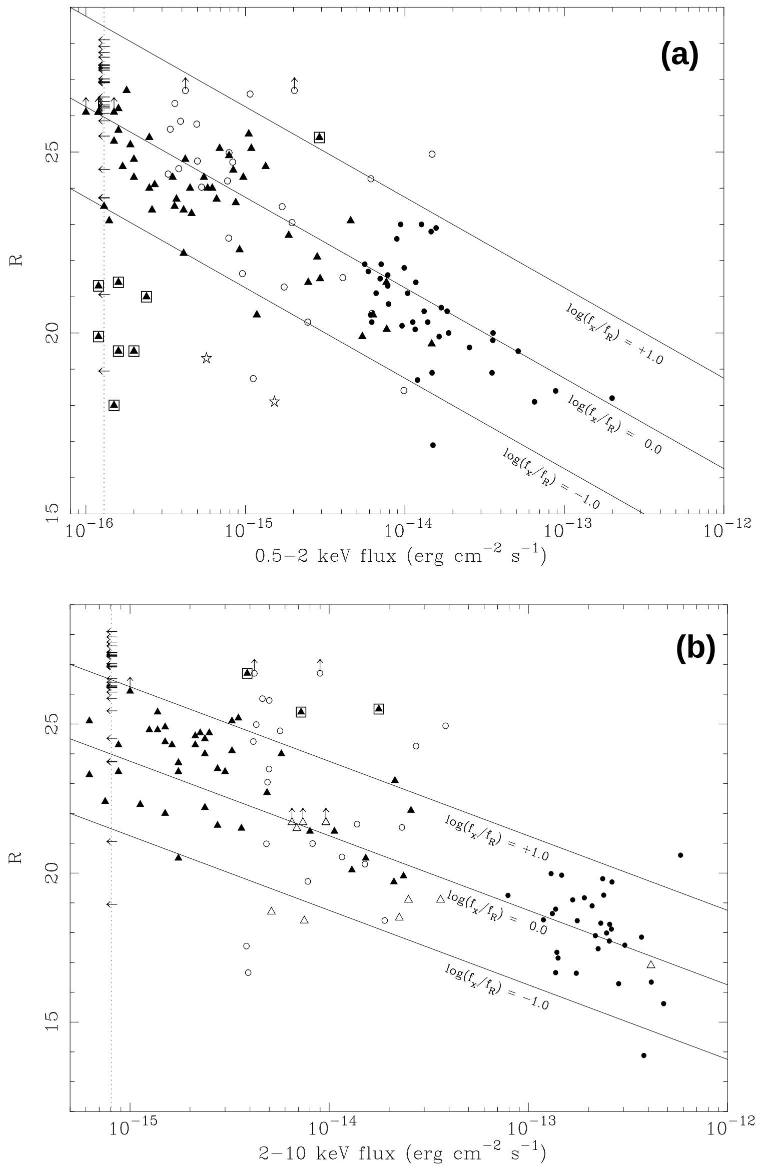

Fig. 8.— Plots of R magnitude versus (a) 0.5–2 keV flux and (b) 2–10 keV flux for X-ray detected sources. Solid triangles are sources from this paper, open triangles are those from Brandt et al. (2000), and open circles are those from Mushotzky et al. (2000). Solid dots in the upper and lower panels are sources from Schmidt et al. (1998) and Akiyama et al. (2000), respectively. We plot only the AGN from Schmidt et al. (1998), excluding galaxies, stars, and groups. The two stars in the upper panel are spectroscopically identified stars (see Table 6 and §A.1), and the left-pointing arrows near the left-hand edges of the plots are AGN candidates discussed in §7.5; F606W magnitudes have been converted to R assuming $F606W - I = 0.22$. The slanted lines are calculated for 0.5–2 keV (2–10 keV) X-ray fluxes ($f_{\rm X}$) in the top (bottom) panel. The vertical dotted lines show our detection limits for an assumed Γ = 1.4 power-law spectrum; sources slightly beyond these lines have spectral shapes differing from a Γ = 1.4 power law. The boxes mark our sources with extreme $\log\left(\frac{f_{\rm X}}{f_{\rm R}}\right)$ ratios as discussed in §5.1 and §5.4.

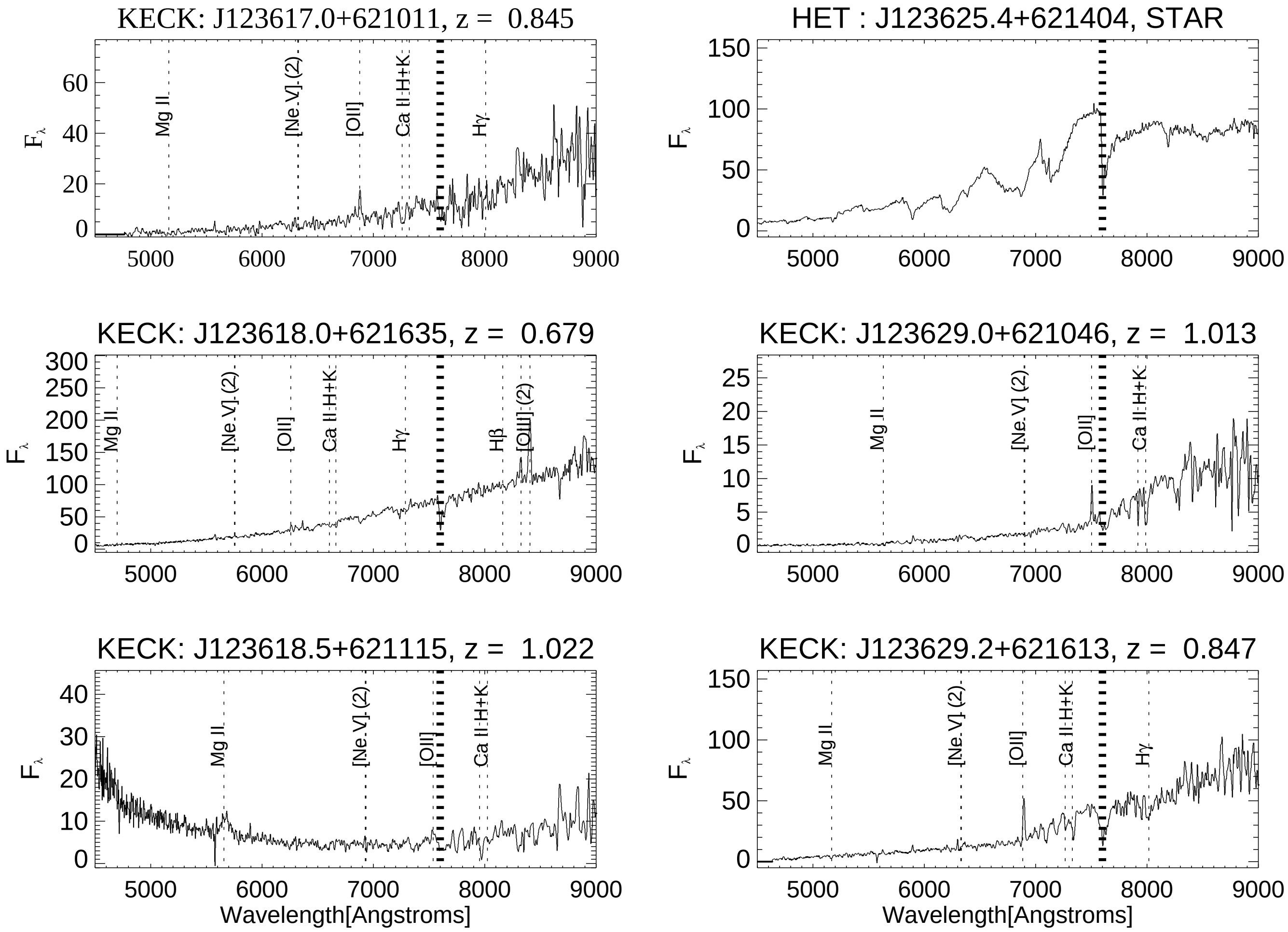

Fig. 9.— Optical spectra of *Chandra* sources. For all spectra, the ordinate is normalized to F_λ (erg cm^{-2} s^{-1} Å^{-1}). No attempt has been made to place the spectra on an absolute spectrophotometric scale. Several key optical transitions have been labeled at their observed-frame wavelengths; a "(2)" indicates that the next line redward is from the same element and ionization state. The hash marked regions indicate atmospheric absorption. The spectral resolution is ≈ 17 Å for both the Keck and HET spectra. Note that second-order contamination is present in the HET spectra at wavelengths greater than 7700 Å. The spectra are described in detail in §A.1.

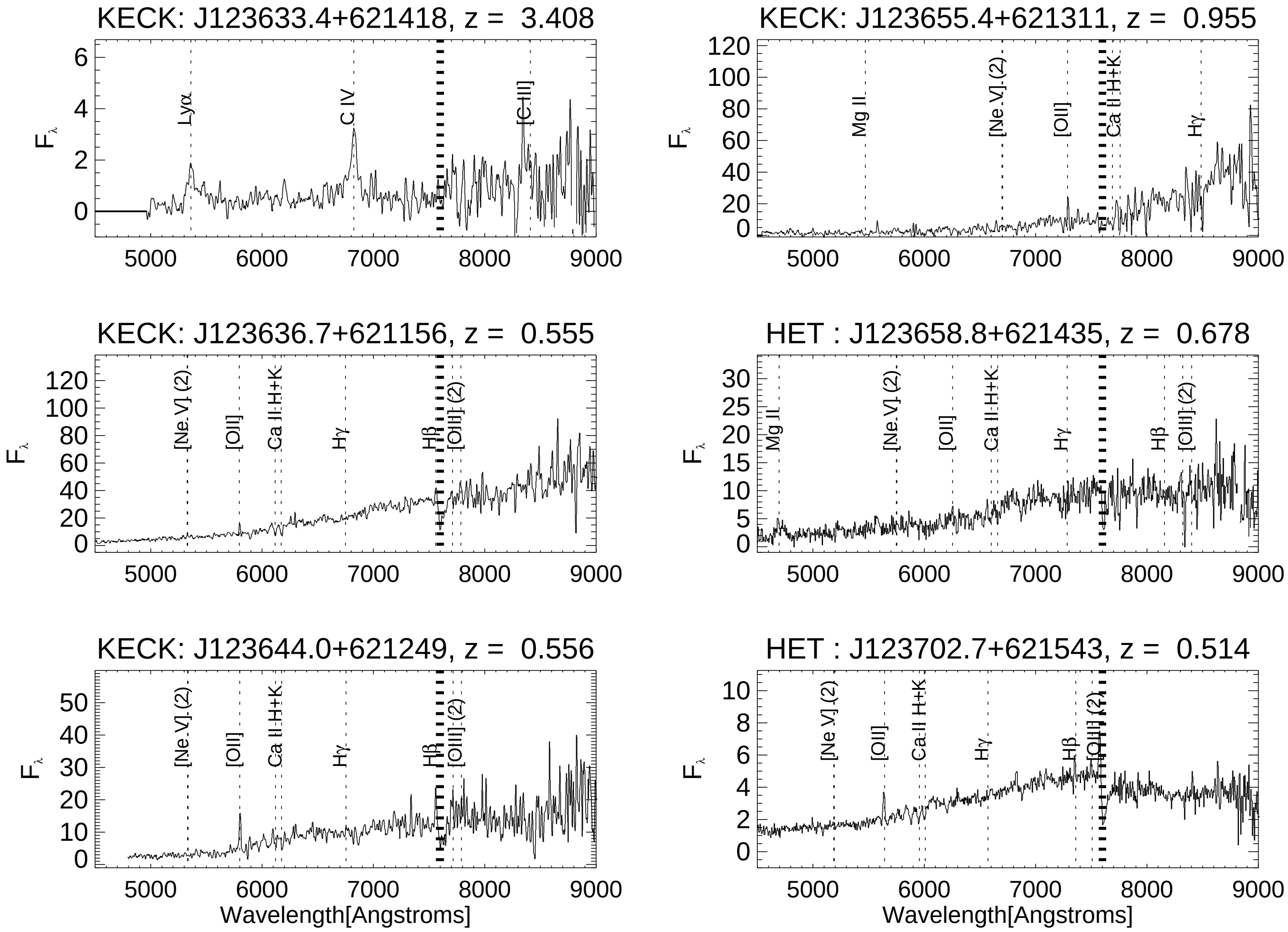
KECK: J123633.4+621418, z = 3.408
Lyα
C IV
[C III]
KECK: J123655.4+621311, z = 0.955
Mg II
[Ne V] (2)
[OII]
Ca II H+K
Hγ
KECK: J123636.7+621156, z = 0.555
[Ne V] (2)
[OII]
Ca II H+K
Hγ
Hβ
[OIII] (2)
HET : J123658.8+621435, z = 0.678
Mg II
[Ne V] (2)
[OII]
Ca II H+K
Hγ
Hβ
[OIII] (2)
KECK: J123644.0+621249, z = 0.556
[Ne V] (2)
[OII]
Ca II H+K
Hγ
Hβ
[OIII] (2)
HET : J123702.7+621543, z = 0.514
[Ne V] (2)
[OII]
Ca II H+K
Hγ
Hβ
[OIII] (2)
F_λ
Wavelength[Angstroms]

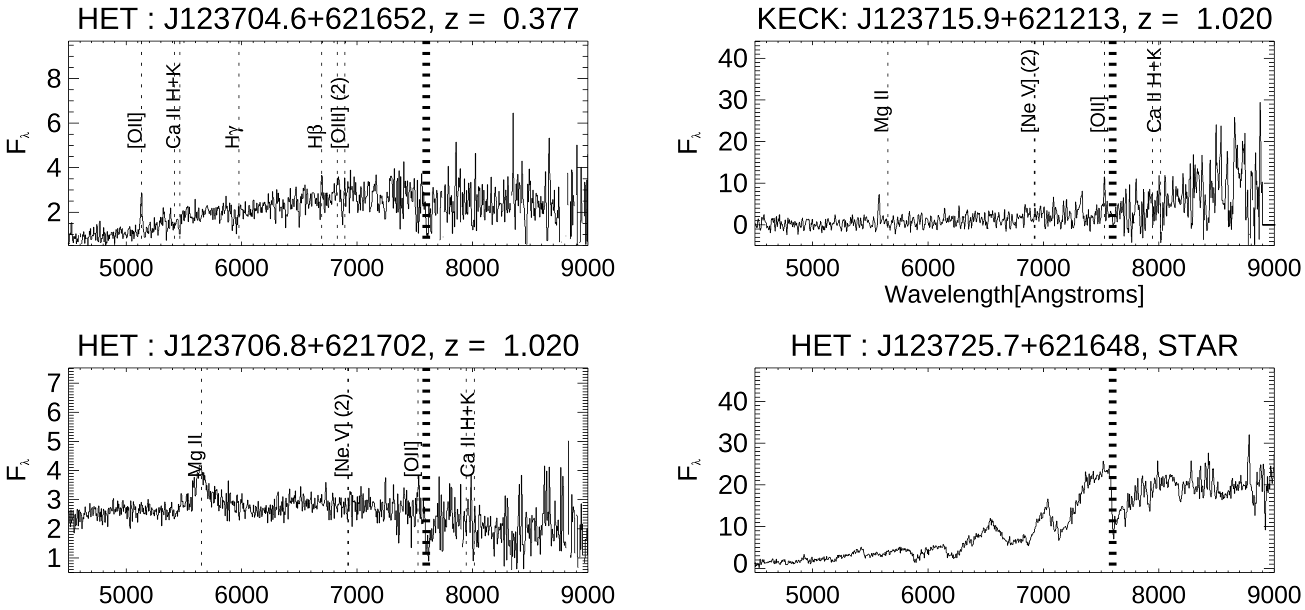
HET : J123704.6+621652, z = 0.377
[OII]
Ca II H+K
Hγ
Hβ
[OIII] (2)
KECK: J123715.9+621213, z = 1.020
Mg II
[Ne V] (2)
[OII]
Ca II H+K
Wavelength[Angstroms]
HET : J123706.8+621702, z = 1.020
Mg II
[Ne V] (2)
[OII]
Ca II H+K
HET : J123725.7+621648, STAR
F_λ

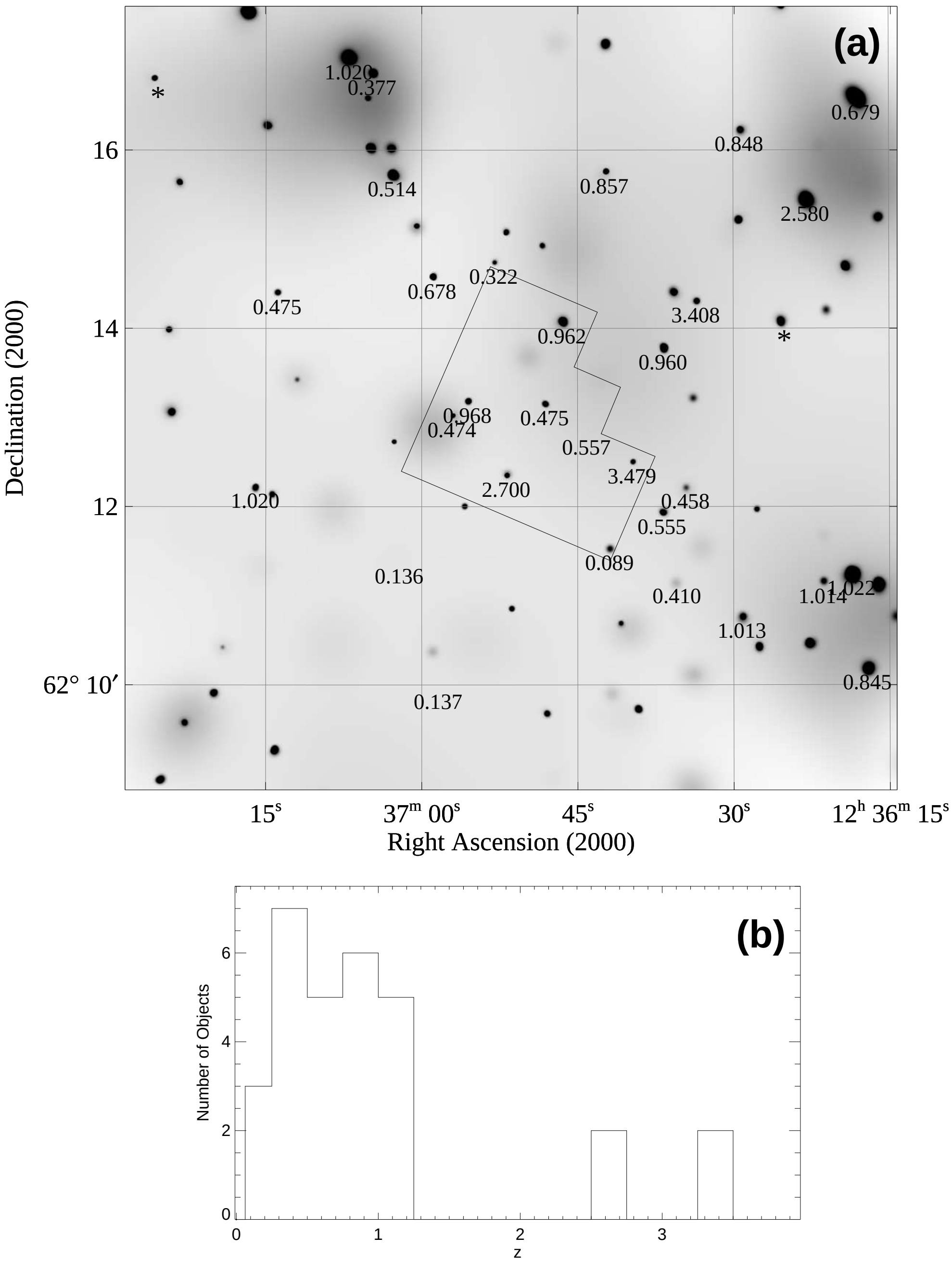

Fig. 10.— Redshifts of *Chandra* X-ray sources. (a) Adaptively smoothed full-band image of the Caltech area with the available redshifts superposed. Redshifts are given immediately below the corresponding X-ray sources, and all redshifts are spectroscopic except for that of CXOHDFN J123651.7+621221 (marked at $z = 2.700$) where the redshift is photometric and uncertain (see H00). The redshift of the object marked at $z = 3.479$ is determined using both photometry and spectroscopy (see §6). The two X-ray sources with asterisks beneath them are stars (of type M4). The adaptive smoothing is at the 3σ level using the code of Ebeling, White, & Rangarajan (2001). (b) Redshift distribution of the 30 extragalactic *Chandra* sources with measured redshifts.

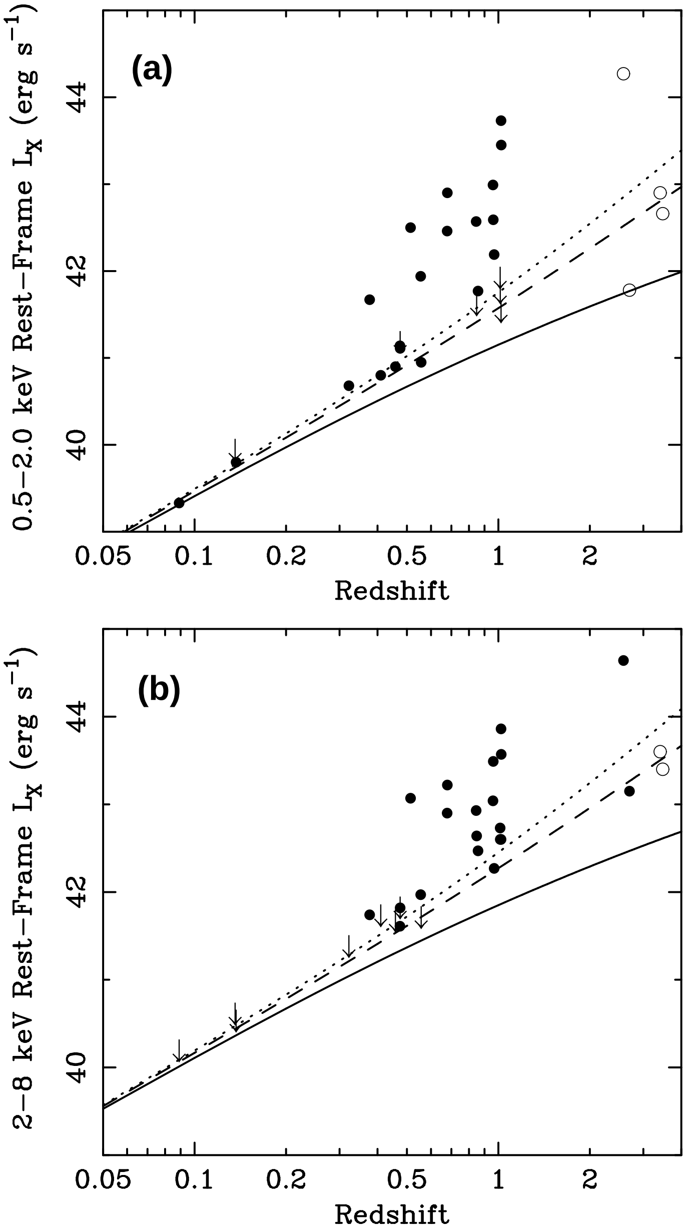

Fig. 11.— Rest-frame luminosity in the (a) soft band and (b) hard band versus redshift for our *Chandra* sources with spectroscopic identifications. The solid, dashed and dotted curves are our detection limits for photon indices of Γ = 0.0, Γ = 1.4 and Γ = 2.0, respectively. Note that we have used a range of photon indices in the calculation of the luminosities. Open symbols are used for four soft-band sources at high redshift due to the fact that we are directly measuring little or no rest-frame soft-band emission from these sources; the derived rest-frame soft-band luminosities are extrapolated from data at higher rest-frame energies. Open symbols are used for two hard-band sources at high redshift where the rest-frame hard-band luminosities were calculated based on observed-frame soft-band data.

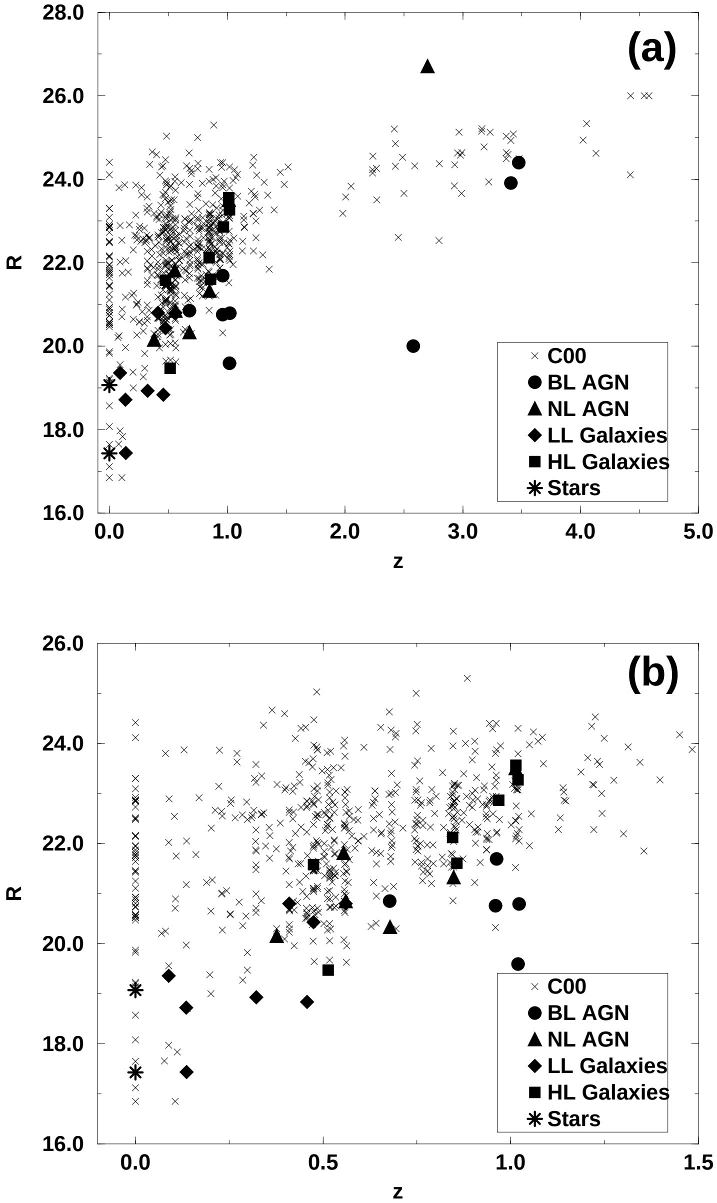

Fig. 12.— $\mathcal{R}$ magnitude versus redshift for all *Chandra* sources having spectroscopic identifications, plotted over the redshift catalog of C00. $\mathcal{R}$ (Hogg00; see §4.2) is plotted here for the X-ray sources in order to make direct comparison with C00 who also use $\mathcal{R}$. Panel (a) shows the total sample of 32 *Chandra* sources with optical identifications, while panel (b) shows the same data for $0 < z < 1.5$, where most of the *Chandra* objects reside. All of the C00 sources at $z = 0$ are spectroscopically identified stars.

Fig. 13.— Two newly discovered X-ray sources in the HDF-N. CXOHDFN J123639.6+621230 is a broad-line AGN at $z = 3.479$. The two objects to the south of CXOHDFN J123639.6+621230 do not have spectroscopic redshifts, but their photometric redshifts of $z = 0.00$ and $z = 1.16$ (Fernández-Soto et al. 1999) are sufficiently different to argue against interaction. CXOHDFN J123644.0+621249 is a $z = 0.557$ emission-line galaxy that also probably contains an AGN (see §6.1). The object to the the south of CXOHDFN J123644.0+621249 is at $z = 0.555$; these two galaxies are likely interacting (see R98 for discussion). The blue circles are centered at the best *Chandra* positions and have diameters of $1''$.

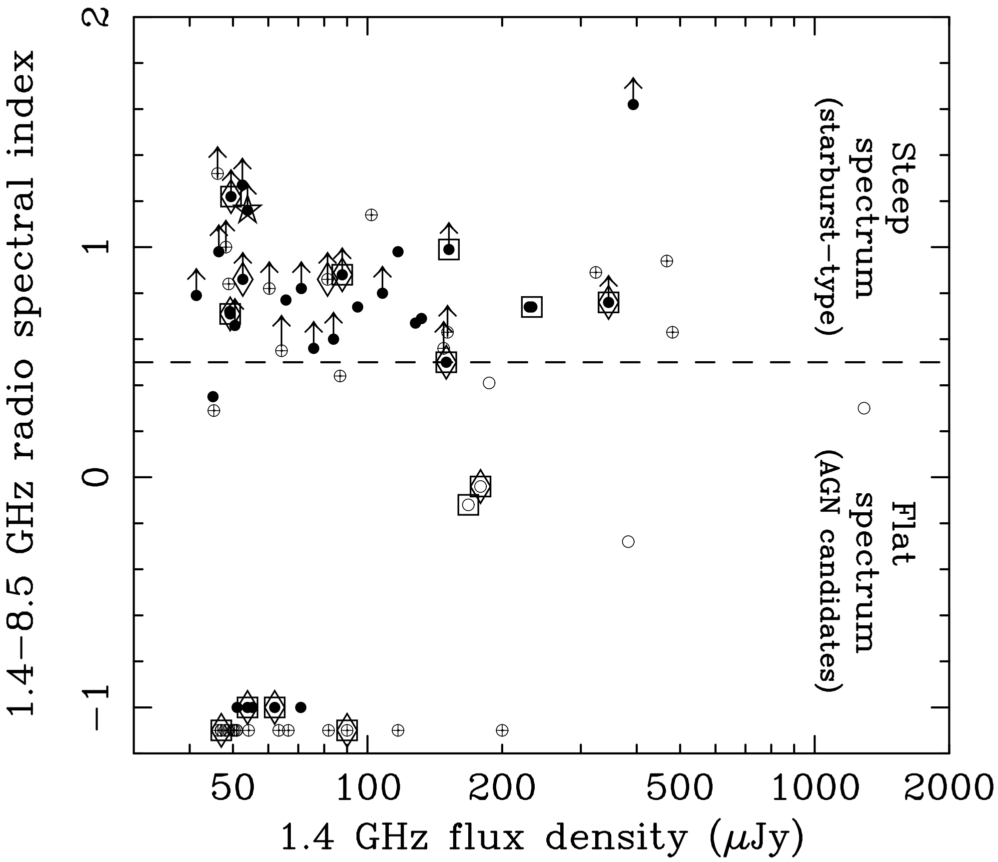

Fig. 14.— 1.4–8.5 GHz spectral index versus flux density at 1.4 GHz for radio-classified starburst-type systems (solid dots), AGN candidates (open circles), and systems of unknown type (circles with crosses inside) detected at 1.4 GHz in the Caltech area (R00). Markers with squares (diamonds) around them indicate that the corresponding source has been detected by *Chandra* in the soft band (hard band). One 1.4 GHz source, J123711.9+621325, was only detected in the full-band data (see Table 8) and is marked with a star around it. The horizontal dashed line drawn at a 1.4–8.5 GHz spectral index of 0.5 denotes the typical value used to separate starburst-type systems and AGN candidates (e.g., §6 of R00). Symbols located at or below −1 along the ordinate do not have measurements of their 1.4–8.5 GHz spectral indices. Note that the X-ray detection fractions, in both the soft and hard bands, are comparable for both the starburst-type systems and AGN candidates.

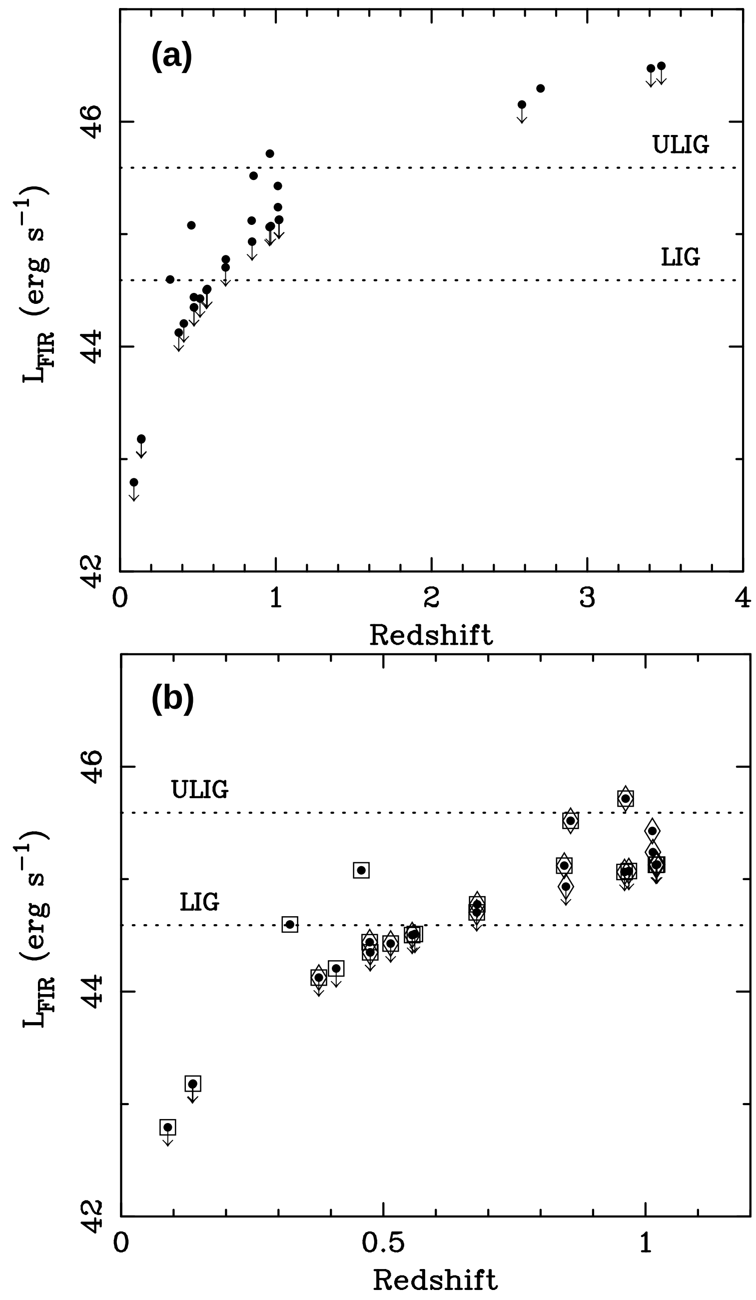

Fig. 15.— Far-infrared (FIR) luminosity, as estimated from the FIR-radio correlation, versus redshift for (a) all our *Chandra* sources with redshifts and (b) only those sources with $z = 0$–1.2. When sources are not detected at 1.4 GHz, we calculate upper limits following §3 of R00. The two horizontal dotted lines show the luminosity thresholds for luminous far-infrared galaxies ($L_{\rm FIR} > 10^{11}\ L_\odot$) and ultraluminous far-infrared galaxies ($L_{\rm FIR} > 10^{12}\ L_\odot$). In panel (b) markers with squares (diamonds) around them indicate that the corresponding source has been detected by *Chandra* in the soft band (hard band); we show a restricted redshift range in panel (b) to minimize symbol crowding. The two sources in panel (a) with $z = 2$–3 are detected in both the soft and hard bands, and the two sources with $z > 3$ are only detected in the soft band.

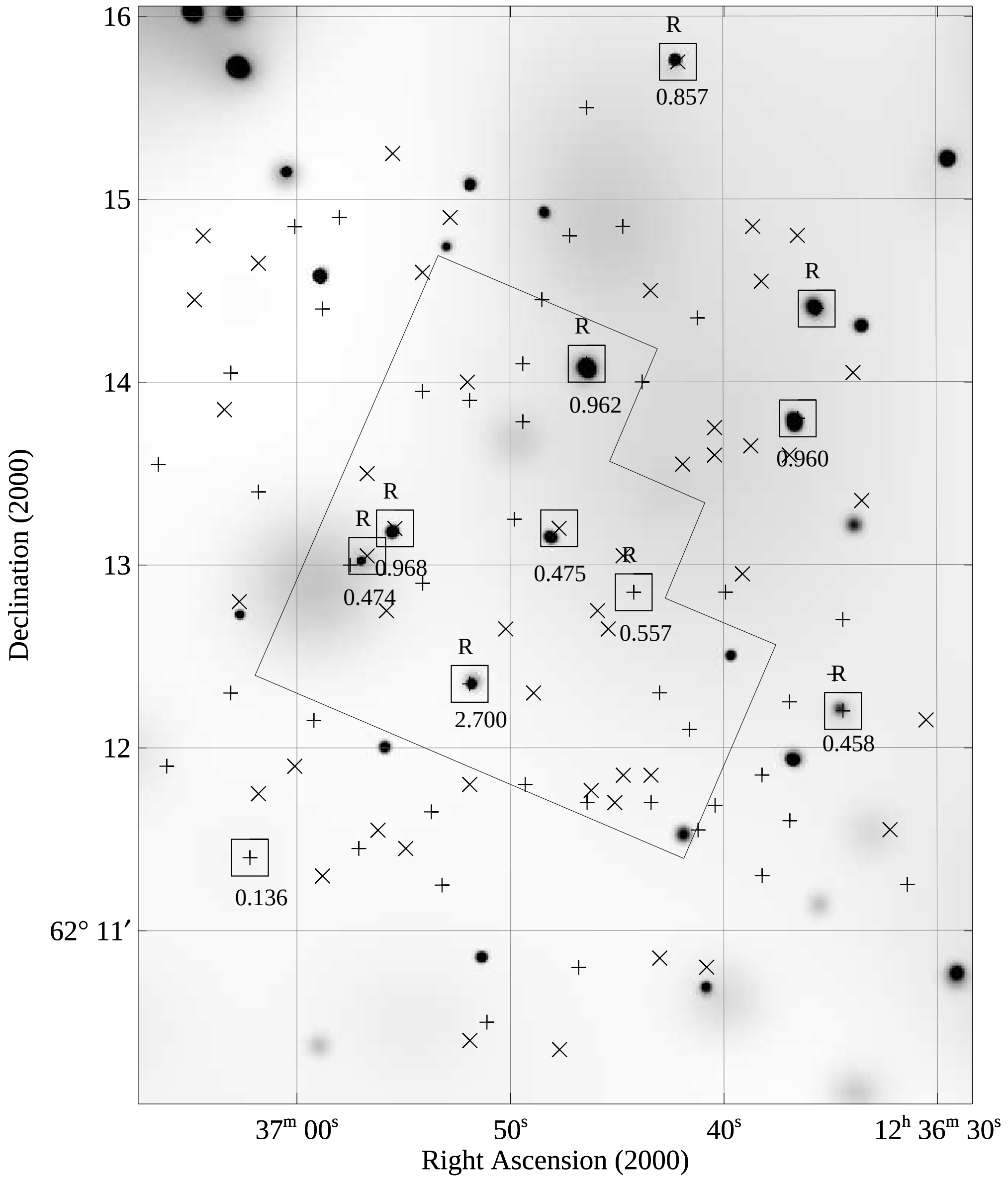

Fig. 16.— Adaptively smoothed full-band *Chandra* image showing the A99 main *ISO*-CAM sources (plus signs) and the A99 supplementary *ISO*-CAM sources (multiplication signs); the entire *ISO*-CAM survey area is shown in this plot. *ISO*-CAM sources with *Chandra* matches are boxed, and when available redshifts are given for these matches below the boxes. Matches with detections at 8.5 GHz are marked with "R" above the boxes. Note that six of the eight *Chandra* sources in the HDF-N have *ISO*-CAM matches and that most of these matches are also detected at 8.5 GHz. The adaptive smoothing is at the 3σ level using the code of Ebeling, White, & Rangarajan (2001).

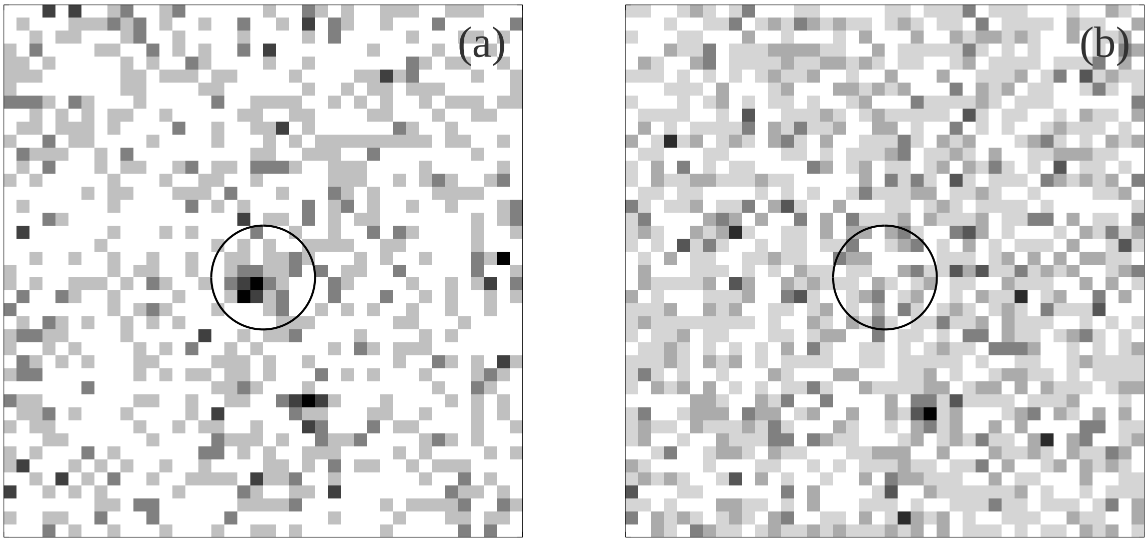

Fig. 17.— Stacked *Chandra* images of the 29 X-ray weak VROs in the (a) soft band and (b) hard band. These images have effective exposure times of 6.02 Ms each, are $20''$ on a side, and have $0.5''$ pixels. The circles in the centers of the images are centered at the nominal stacking position and are $2''$ in radius. Note the X-ray source in the stacked soft-band image that is not visible in the stacked hard-band image; this source is found by WAVDETECT in the soft band when WAVDETECT is run with a probability threshold of 1×10^{-7}. The detection of the stacked X-ray weak VROs only in the soft band contrasts with the hard X-ray emission of the four VROs individually detected by *Chandra*.